Università degli Studi di Firenze
Facoltà di Ingegneria

Scuola di Dottorato in
Ingegneria Industriale

Dottorato in Energetica e Tecnologie Industriali ed Ambientali Innovative - XXVI Ciclo

Harvesting Power from Marginal Energy Content Sources: a Study on the Road Traffic

Autore:

Ing. Alessandro Mattana

Relatore:

Prof. Francesco Martelli

Correlatori:

Prof. Claudio Borri

Dott. Ing. Simone Salvadori

UNIVERSITÀ
DEGLI STUDI
FIRENZE
DIEF
DIPARTIMENTO
DI INGEGNERIA
INDUSTRIALE

Coordinatore del Dottorato:

Prof. Maurizio De Lucia

Anno Accademico 2013/2014

Acknowlegments

Before presenting the topics of the present thesis, I would like to thank several persons, that have make possible such a result.

A special thank goes to Ing. Simone Salvadori who has introduced me in the group where I have spent these last 3 years of intense work; he has been a great point of reference with all his advices all along this time.

Then, I would like to thank Prof. Francesco Martelli for trusting my capabilities and for giving me the opportunity of working within his group.

A cordial thank gives to Ing. Tommaso Morbiato and Prof. Claudio Borri as well, for sharing time, ideas and comments on the subject.

A grateful thank also gives to all the colleagues whose time is still spent side by side and especially Massimiliano, Alessandro, Duccio, Adriano, Leonardo and Mauro.

Another time, with deep gratitude, a thank goes to my family, for the opportunity and patience in supporting my choices with a special and loving thank for my sister, for having such a journey together.

Abstract

The actual energetic research context aims at reducing the fossil contribution to the overall energy world consumption by means of renewable and alternative energy sources.
Among the latter, new technologies for harvesting power from marginal energy contents is emerging, especially aiming at powering portable and small-sized electronic equipment.
Within such a category is the idea of harvesting energy from the air-flows induced by the motion of road vehicles by means of wind turbines. Therefore, a numerical investigation has been done aiming at characterize both the assumed resource and the feasibility of using vertical axis wind turbines for exploiting the air-flow energy content.
After a deep survey into the available technical literature, an energy balance is derived first and the problem attacked by means of a 1D flat-plate approach to see how the total drag divides into pressure and viscous effects. For this purpose, the best energetic scenario was selected and attention paid on tractor-trailers systems.
Computational Fluid Dynamics simulations are then planned, and a wide section is dedicated to the selection of the adequate numerical approach basing on results found in the conventional aerodynamic literature about trucks. Hence, the external aerodynamics of a European truck type designed for the purpose is studied in both 2D and 3D environments and use of steady and unsteady RANS approaches implemented into the ANSYS Fluent® environment.
Study of the external aerodynamics is made from the point of view of an observer fixed to the ground, revealing a peculiar flow pattern that 2D sim-

ulations are not able to catch properly, 3D results for the steady simulations proving the strong three-dimensional effects affecting the induced flow. For this purpose comparison among the obtained results for the two approaches is made in a devoted section.

Moreover, time dependent analysis were considered mandatory for investigating the interaction between an external object and the approaching vehicles. By use of the remeshing technique available in Fluent, it was possible to study such a problem in both 2D and 3D domains for the case of one moving truck. In doing so, and with focus on the region above the truck, the induced flow has been characterized and the mechanism of loading the external object explained.

According to 3D results, tests for a Savonius rotor type were made assuming the simulated velocity pulse induced by the moving truck. The turbine start-up dynamics for both the single truck case and that for a very long truck row were considered and both the no-load and with-load cases were explored solving the second cardinal equation of dynamics. Results are shown to be in a good agreement with the available experimental data and the feasibility of using such a technology deeply investigated.

Contents

1 Introduction 17

2 Phenomenological Aspects and Basic Tools 1

2.1 Effects due to road vehicles 3
    2.1.1 Evaluating horizontal loads on a model highway sign . 4
    2.1.2 Full scale measurements on road-side signs 14
    2.1.3 Validating data with both recent theoretical and experimental tests 17
    2.1.4 Conclusions about phenomenological aspects 20
2.2 Exploring truck's aerodynamics with CFD 21
    2.2.1 Analysis made on simplified truck shapes: the GTS and GCM models 22
    2.2.2 Simulations on the GTS model 26
        2.2.2.1 RANS simulations 26
        2.2.2.2 DES simulations 30
    2.2.3 Simulations on the GCM model 33
        2.2.3.1 RANS simulations 33
        2.2.3.2 URANS simulations 35
    2.2.4 LES simulations of a simplified tractor-trailer system . 37
    2.2.5 Conclusions about CFD techniques for exploring truck's aerodynamics 41

3 Investigating the Energy Contents: PLANNED ACTIVITIES 42

3.1 Energy Balance Analysis 44

3.2 Numerical Analysis 47
    3.2.1 Flat Plate Approach 48
    3.2.2 CFD Analysis 49
        3.2.2.1 RANS modeling with 2D/3D approaches . . 51
        3.2.2.2 URANS modeling with 2D/3D approaches with obstacle probes 54

4 Investigating the Energy Contents: RESULTS 58
4.1 Energy Balance Analysis Results 59
4.2 Numerical Analysis Results 61
    4.2.1 Flat Plate Approach 61
    4.2.2 CFD Analysis 67
        4.2.2.1 RANS modeling with 2D/3D approaches . . 67
        4.2.2.2 URANS modeling with 2D/3D approaches with obstacle probes 80
4.3 Comments on the Obtained Results 89

5 Exploiting the Wind Energy Content: the Start-up Problem 92
5.1 Drag-Type Wind Rotors 93
5.2 Start-up Dynamics of a Savonius Rotor 98
    5.2.1 Code Validation 99
    5.2.2 Turbine Response to the Equivalent Velocity Pulse: 1 Truck Case 101
    5.2.3 Turbine Response to the Equivalent Velocity Pulse: Multi-Truck Case 108
    5.2.4 Estimating the Energy Output 113

6 Conclusions and Perspectives 116

List of Figures

1.1 Figures extracted from [1] 19
1.2 Figures extracted from [2] 20
1.3 Figures extracted from [3] 21
1.4 The Double New Jersey design proposed in [4] 22
1.5 Figures extracted from [5] 23
1.6 A sketch of the harvesting system from [6] 24
1.7 Figures extracted from [7] 25
1.8 A sketch of the harvesting system from [8] 26
1.9 Figures extracted from [9] 26
1.10 the New Jersey concept proposed in [10] 27
1.11 the *Turbine light*, from [11] 27
1.12 the New Jersey design proposed in [12] 27
1.13 the *Green tunnel* unit from [13] 28
1.14 the *City Speed Turbine* concept, from [14] 28
1.15 Figures extracted from [15] 29
1.16 The in-field installation, from [16] 29

2.1 The model tested (dimensions in *mm*), from [17] 4
2.2 Non-dimensional time histories for measured velocities , from [17] 5
2.3 Non-dimensional velocity profiles, from [17] 7
2.4 Non-dimensional acceleration history, from [17] 8
2.5 The wake decay exponent trends, from [17] 8
2.6 Rig geometry 9
2.7 Typical force coefficient time history 10
2.8 The effect of varying sign height 12

2.9 Source vehicle experimental data VS simplified potential model 12
2.10 The effect of varying vehicle shape 13
2.11 Sketch of the main results from [18] 14
2.12 Example of an ensemble average measurements for a square sign placed at 1,5 m distance from the closest passing vehicle. Red box: wind speed measurement 15
2.13 Typical load coefficients found by Quinn et al. in one of the road sections considered 16
2.14 Maximum suction peak dependance with separation distance from vehicle 17
2.15 Load coefficient for pedestrian barriers placed perpendicular (empty squares) and parallel (filled squares) to the roadway direction 17
2.16 Potential model approximations (solid line) and comparison with experimental data (dots) 18
2.17 Comparison between normalized load coefficients on a flat plate with varying the sign angle with respect to track direction. 19
2.18 US vehicles classes 22
2.19 Cab designs. Top: COE - Bottom: conventional 23
2.20 Standardized models used for investigating drag-reduction devices. (Figures depicted in different scales) 23
2.21 Computational domain, from [20] 27
2.22 C_p variations on MGTS surfaces, from Veluri et al. [20] 28
2.23 PIV measurements vs RANS predictions in the GTS base region, from Roy et al. [21] 29
2.24 Center-plane wake vorticity distributions for the GTS model . 30
2.25 Center-plane pressure coefficients. Comparison with experimental values from Storms et al. [22] 31
2.26 Pressure coefficients for RANS and DES predictions 32
2.27 Predicted pressure coefficients for different regions of the GCM model compared with experimental values 34
2.28 Velocity magnitude predictions 34
2.29 Velocity magnitude predictions 35

2.30 Comparison between predicted pressure trends and experimental values in the base region 36
2.31 RANS vs URANS drag predictions for the coarse mesh 36
2.32 The vehicle used by Krajnović and Davidson in their LES simulations 37
2.33 The vehicle studied in [24] 38
2.34 Comparison between predicted and experimental C_d values . 39
2.35 Surface projected streamlines on the lateral face of the cab box: with sharp edges (left) and rounded edges (right) 39
2.36 Time averaged streamlines - g/b=0.17 40

3.1 Examples of truck aerodynamic styling 44
3.2 Surfaces where drag contributions arise 45
3.3 Drag data for a streamlined 2D cylinder at Re=10^6, adapted from [25] 46
3.4 The ET design 50
3.5 3 truck mesh case and domain alignment for the 2D analysis and postprocessing phase 53
3.6 Test validation for the dynamic mesh approach 55
3.7 General sketch of the 2D unsteady simulations 56
3.8 The 3D obstacle model 57

4.1 Energy consumption percentages from [26] 59
4.2 Measured total drag 62
4.3 Skin-friction and boundary layer thickness distributions for the GTS model at $2 \cdot 10^6$ and $4.8 \cdot 10^6$ Reynolds numbers . . . 63
4.4 Non-dimensional velocity profiles for the W-section 100km/h case on the trailer roof 68
4.5 Curves representing the Vx=0 loci for the 1 truck, 2 trucks and 3 trucks rows. (rectangular shapes correspond to trucks placement) 69
4.6 Cp trends for the 1 truck, 2 trucks and 3 trucks rows. Thin lines are for the $\Delta Y/H = 0.64$ section, the thick ones for the $\Delta Y/H = 0.26$ section 70

4.7 2D vs 3D non-dimensional velocity and pressure profiles . . . 75
4.8 2D vs 3D non-dimensional velocity and pressure profiles . . . 76
4.9 $3D$ non-dimensional velocity and pressure dependence from Z/W coordinate 77
4.10 $\Delta Y/H = 0.26$ section with projected streamlines. Streamtubes narrow at both the front and base regions of the truck, hence the highest values of V_x/U_0 locate here 78
4.11 Flow pattern and V_x/U_0 magnitude at $Z/W = 0.36$ 79
4.12 The flow structure wrapping the moving truck 79
4.13 Drag coefficients variations due to rectangular and circular shape objects 81
4.14 3D total and pressure drag coefficients versus non-dimensional time 82
4.15 Drag and lift time histories for drag and lift coefficients . . . 84
4.16 Angle variation with time for total forces acting on the cylinder 85
4.17 Absolute values of total forces acting on the cylinder 86
4.18 Non-dimensional equivalent flow velocity 86
4.19 3D streamlines comparison at $Z = 0$ sections 87
4.20 The pressure field on the simulated obstacle at U_0t/L=0.15; pressure units in Pa 88

5.1 Drag and lift type rotors 93
5.2 Working principles of drag and lift type wind rotors 94
5.3 Wind turbines power coefficients, from [27] 95
5.4 Cp curves for Savonius and Darrieus wind rotors 96
5.5 Curves for the 2-bladed Savonius rotors, from [28] 100
5.6 Numerical results compared to tests from [28] 100
5.7 The turbine dynamics when subjected to v_{eq} 102
5.8 Turbine start-up comparisons with varying the moment of inertia 104
5.9 The turbine dynamics 106
5.10 Start-up analysis with varying the rotor inertia 107
5.11 Loads and equivalent velocity pulse as derived for the 3 truck case study 109

5.12 The turbine dynamics for the case of a truck row with vehicles spaced 10 m apart 111
5.13 Turbine start-up behaviour when subjected to a long truck row112
5.14 Turbine start-up behaviour when subjected to a long truck row114

List of Tables

2.1 test matrix from [18] 9

2.2 Models data. L=Length - H=Height - W=Width. (wheels not included) 24

2.3 Drag coefficient comparison with varying turbulence model, from Veluri et al. [20] 29

2.4 Predicted drag and errors, from [29] 31

2.5 Predicted drag and errors 33

2.6 Predicted drag and errors 38

3.1 Test matrix for 2D RANS analysis 51

3.2 Boundary conditions 52

3.3 Test case for the 3D RANS simulations 54

3.4 Test matrix for the 2D URANS analysis 56

3.5 Test case for the 3D URANS simulations 57

4.1 Experimental values for the GTS scaled model 60

4.2 Speed correspondences between the GTS model and the GTS at full-scale 61

4.3 Comparison between GTS drag values for the $2 \cdot 10^6$ and $4.8 \cdot 10^6$ Reynolds numbers 63

4.4 Height of the viscous region upon the trailer's roof computed from flat-plate theory (GTS at full-scale) 65

4.5 Total and roof-friction wasted powers computed basing on flat-plate theory (GTS at full-scale and ambient conditions) . 66

4.6 Truck drag coefficients and wasted powers based on the NW-section 2D analysis results 71

4.7 Truck drag coefficients and wasted powers based on both the W and NW sections 2D analysis results 72
4.8 Deviations of power values relative to flat-plate approaches - truck model based on NW-section 72
4.9 Deviations of power values relative to flat-plate approaches - truck model based on both W and NW sections 72
4.10 Results for the 3D analysis and comparison with the flat-plate results 80
4.11 Required energy boost to keep the speed constant 82
4.12 Results obtained for the 100 km/h speed case 89

Nomenclature

A	Vehicle Projected areat	$[m^2]$
A_R	Wind Rotor Swept Area	$[m^2]$
C_d	Total drag coefficient	
C_f	Load coefficient	
C_{PR}	Rotor Power Coefficient	
C_{QR}	Rotor Torque Coefficient	
C_{df}	Skin-friction drag coefficient	
C_{dp}	Pressure drag coefficient	
F	Force	$[N]$
H	Truck Height	$[m]$
I_R	Wind Rotor Moment of Inertia	$[Kgm^2]$
L	Truck Length	$[m]$
M_mR	Wind Speed	$[m/s]$
M_{mR}	Rotor Aerodynamic Torque	$[Nm]$
M_{rR}	Rotor Parasitic Torque	$[Nm]$
P_R	Wind Rotor Delivered Power	$[W]$
P_{tot}	Total aerodynamic power consumption	$[W]$

R	Wind Rotor Radius	$[m]$
Re	Reynolds number	
S	Sign panel area	$[m^2]$
TSR, λ	Tip Speed Ratio	
U,U_0	Vehicle speed	$[\frac{m}{s}]$
V_0	Wind Speed	$[m/s]$
V_x	Absolute flow velocity, X-component	$[m/s]$
X	Axial coordinate, origin at the vehicle nose	$[m]$
Y	Height from street plane	$[m]$
Z	Transversal coordinate, origin at the vehicle midplane	$[m]$
ΔY	Distance from truck surface in the Y direction	$[m]$
c_f	Skin friction coefficient	
p	Pressure	$[Pa]$
t	Time	$[s]$
w,W	Truck Width	$[m]$

Greeks

δ	Boundary Layer Thickness	$[m]$
ν	kinematic viscosity	$\left[\frac{m^2}{s}\right]$
ρ	Air density	$\left[\frac{kg}{m^3}\right]$

Subscripts

i	i-*th* component
m	Model
r	Reference value

Superscripts

c	Corrected value
r	Value at the roof of the vehicle

Chapter 1

Introduction

The Energy Harvesting process relates to those methods and technologies planned to harness that energy fraction of a process that otherwise would be lost by means of vibrations, light, sound etc. With this perspective and in the context of the present efforts in searching new energy sources, a lot of ideas and solutions are introduced. Sources of great availability are the most attractive, even if often are those that supply marginal energy contents. Therefore, for these sources the energy potential lyes in the repetition of the energy-generation event, rather than in the single $energy-packet$ available.

The idea of extracting energy from the road traffic by means of a tailored wind-energy device falls in such a category. Because of transportation, with both private and freight destinations, road vehicles are considered a huge energy source when considering their aerodynamic energy loss. The aerodynamic drag arises because a vehicle needs to displace the air out of the way, hence a fraction of the engine power output is transferred to the air itself. This event occurs once with the vehicle transit, hence this energy transfer is discontinuous and the energy potential of such a source consists in the passage of multiple vehicles, i.e. on the vehicular traffic.

Consider for example the Italian A1 highway in the section connecting Brescia with Padova; at the end of the first three months of 2013, the daily heavy vehicles traffic was estimated in 22,179 VMGT, amounting to about 28 % of the total traffic there, AISCAT [30]. Assuming common values for vehicle frontal dimensions and typical cruise speeds (A_r=10 m/s. U_r=90 km/h, see

Sec. 2.2.1 later), with a track length of 146.1 Km and a drag coefficient of about 0.6, the power wasted by each vehicle would amount to 56.25 kW, see Eq. 2.8, corresponding to about 91.3 kWh wasted energy. Considering now the number of vehicles reported above, we obtain that heavy vehicles in the highway section considered put into the air something like 2 GWh daily. Note now that this corresponds to about 750 times the yearly energy consumption of an Italian middle-class family (2700 kWh).

As proved above, very often it is not a problem to recognize where some energy fraction of a process is gone nor to estimate it, rather of great difficulty is to asses whether that energy content could be harvested. Furthermore, this issue rarely relies in finding a device that make the job, rather consists in studying the assumed resource and evaluate if the harvesting process could interfere with the primary process that provides the energy content we are looking for. Not having such an interaction is a must in an harvesting process of the kind considered here, hence a deep knowledge of the structure of the resource is needed before every attempt in harnessing some energy content is made.

Despite such keynotes, our research shows that many of the efforts in the direction of harvesting energy from the road traffic (in the form of a presumed induced-wind) focus mainly on devices and equipments, as it was certainly that the harvesting process is feasible.

The first record we found about exploiting induced-wind relates to a US patent application published in 1993 and cited by Bellarmine and Urquhart [31], who speaks about the so called *Highway energy barrier*, [1]. The apparatus consists in a modified road-barrier typically used to separate lanes (*New Jersey* barriers) where vehicles travel in opposite directions, see fig. 1.1(a) for the general configuration of the proposed system.

The equipment embodies one Savonius vertical-axis rotor at least, whose rotation would be induced by both the airflows generated by the oppositely moving vehicles. The preferred embodiment suggests use of a plurality of rotors all connected to a main shaft where a flywheel rotates to maintain uniformity in the energy output with passing vehicles, see fig. 1.1(b). Use of deflectors to convey the airflow towards the rotor blades is suggested as a means for increasing the energy output. A claim in [31] relates to the use

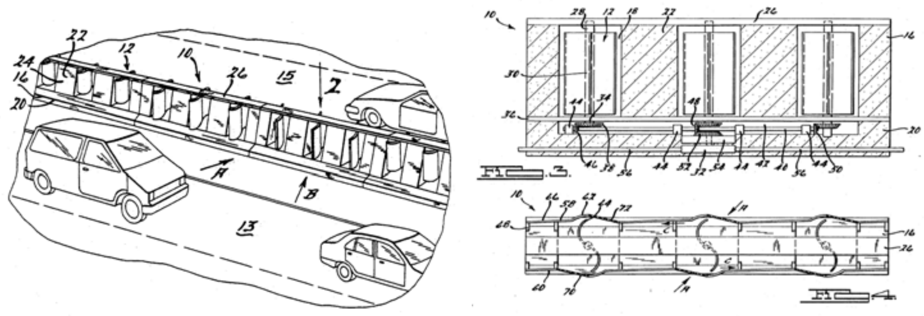

(a) A sketch of the subway layout

(b) A detail of the wind-collecting duct

Figure 1.1: Figures extracted from [1]

of the energy barrier for a highway scheduled for construction in 1996-1997, but up to date we are not aware about any of such a use.

In 2001 we found the patent application of Wilson [32] where again mention of a vertical axis wind turbine is done for exploiting the energy contents of vehicles generated airflows. The system is proposed to be operated in several configurations, with the possibility to be used also adjacent to airports runways.

About 1 years later, Gutterman [2] proposed a device to harvest energy from subway trains rather than road vehicles. It is possible to find other patents relating the exploiting of trains induced-flows, but here we present this one only because not strictly related to road-vehicle case. Anyway, in this granted patent a subway system layout is proposed where collecting ducts allow the induced-flow generated from the moving trains to be channeled towards horizontal wind rotors, see figs. 1.2.

In 2004 Bilgen [3] suggested use of a special drag-driven device, see Figs. 1.3. In this case, as that of Gutterman [2], the system is proposed to be placed upon the moving vehicles rather than on their sides, but no explanation is given about the reasons behind of such a choice.

One year later, in 2005, resurgence of the road-barrier concept is proposed by Di [4]. The system is shown in fig. 1.4 where because of safety reasons the rotor system is suggested to be placed between two barriers rather than

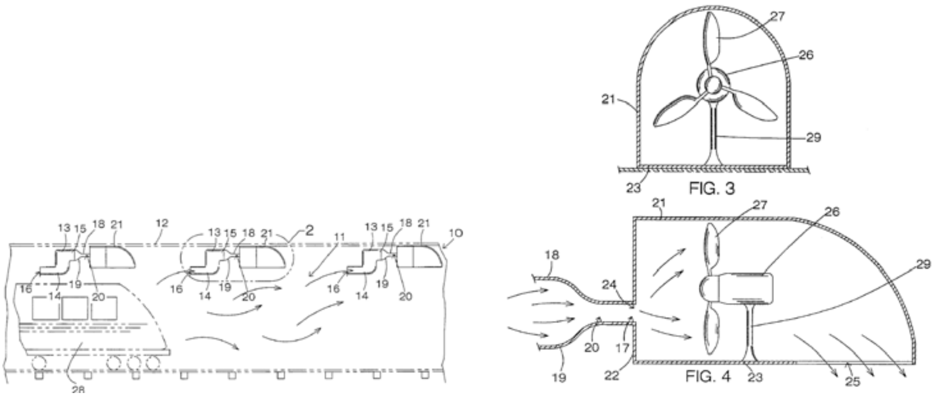

(a) A sketch of the lane layout (b) The Highway Energy Barrier

Figure 1.2: Figures extracted from [2]

incorporated within a single structure. The induced flows are collected by air conveyance elements on both the lanes sides. Furthermore, the authors introduce several rotor shapes aiming at increasing conversion efficiency and air discharge, once the air has slowed down through the rotor.

In 2007, Wiegel and Stevens [5] propose their *traffic driven wind generator* consisting in the use of high aspect-ratio Savonius type rotors for both road vehicles and trains, see figs. 1.5.

In the same year we found the patent applications of Spinelli [33] and Dempster [34] both dealing with the use of Savonius-like rotors to harvest energy from vehicles generated flows. The device in [33] resemble that of [1] because is proposed again the idea of gathering the flows coming from both the lane directions (using a road barrier as a housing structure).

In the 2008, Schmidler [35] mentioned the idea of harvesting the pressure form of the vehicle induced-flow rather than its dynamic part. The inventor deals with spring-linked devices able to drive electrical generators operating in both rotational and linear manner and no turbine is then considered.

In 2009 we find the proposals of Gushakowski [36] and King and Ratcliffe [37], while in 2011 Van Meveren and Van Meveren [6] suggested a wind-rotor set-up very close to that of Wiegel and Stevens [5]: the rotor is placed upon the vehicle but use of straight blades instead of the curved ones is proposed,

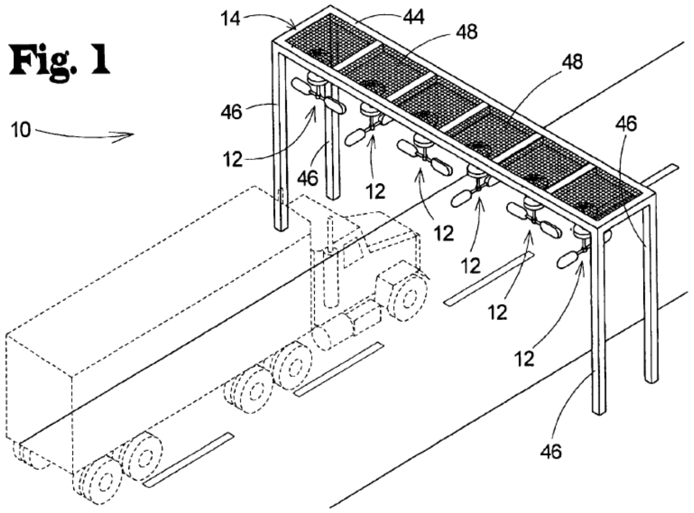

(a) A sketch of the lane layout

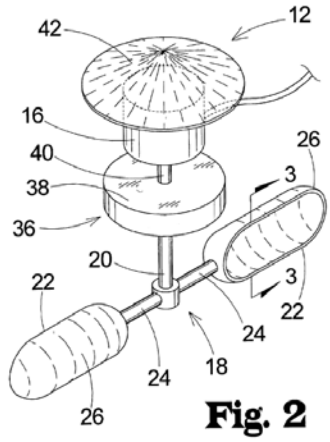

(b) The rotor design

Figure 1.3: Figures extracted from [3]

see figs. 1.6.

One year later, Mauro and Alkaragholy [7] proposed to collect the vehicles induced-wind through a trench made along the road (i.e. underneath the

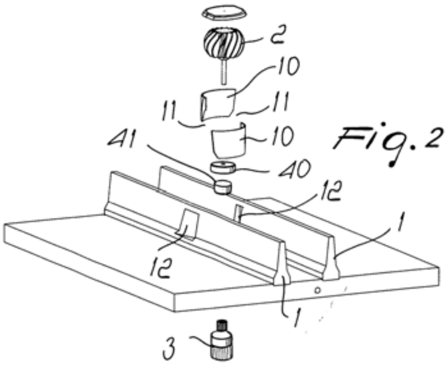

Figure 1.4: The Double New Jersey design proposed in [4]

vehicles) covered with grids, see fig. 1.7(a). In the patent we found different cavity sections all with drainage piping systems to allow the trench being filled up by water, as sketched for example in fig. 1.7(b).

In 2013, Ignatiev and Song [8] propose again use of a by-side configuration for a wind-rotor unit, see fig. 1.8. Unlike the aforementioned patents, in this one we found some consideration about the structure of the resource (we found a CFD contour-map of velocity of a moving truck) allowing the author to gather information about the wind-unit placement with respect to the moving truck.

As briefly showed, all but one of the patents analyzed are based on the idea that what really is at disposal with the vehicle transit is an induced-wind useful to make wind-rotors rotate and generate power. When this idea is assumed to be true, in almost all the devices analyzed use of a vertical-axis wind rotor is suggested. This fact could be related to two main factors: the first one is based upon the favorable set-up of such kind of wind-rotors and their compactness; The second one consists in the intuition that a moving vehicle generates a flow that vary its direction during the transit, hence vertical axis rotors are suitable for this condition because do not require alignment with the wind direction. Furthermore, lift devices are for the most part not considered, while often are proposed drag-driven rotors. Once again, we may gather that behind such a choice lays a specific reason, i.e. the higher starting capabilities of the drag-driven devices compared to the lift-driven

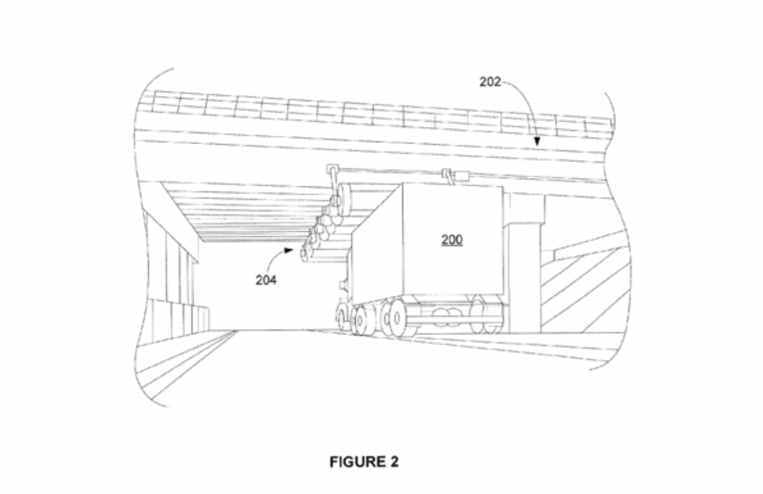

(a) Lane layout

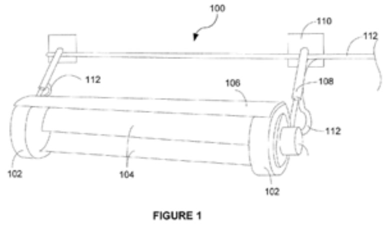

(b) The rotor design coupled with safety shroud

Figure 1.5: Figures extracted from [5]

types. In considering the rotor self-starting issue, one may think about the use of machines with very low rotational inertia in order to assure good start-up capabilities, while often is recommended the use of flywheels connected to turbines shafts to make rotors keep their motion. This is why sometimes servomotors are suggested to be used, making the supposed energy-device more complex to be operated.

The idea of harvesting energy from such special flows seems to be widespread,

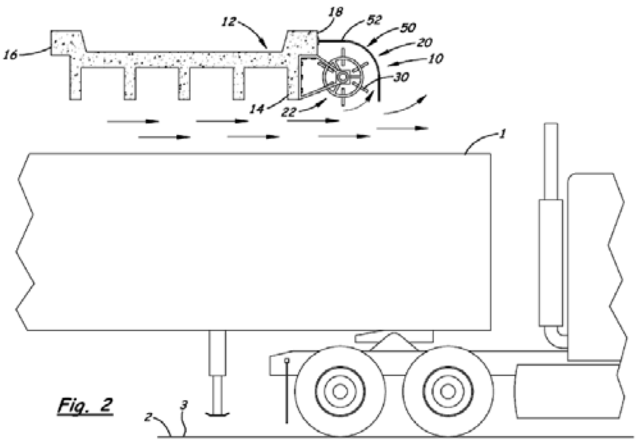

Figure 1.6: A sketch of the harvesting system from [6]

as a brief search on the web shows. From that search, it seems that the first one who proposed use of the vehicles induced-flows for energy harvesting purposes is a student from the Arizona State University, [9] see figs. 1.9, as quoted also by Chen et al. [38]; With an assumed induced-wind speed of about 10 mph in average, the author claims an annual energy production of 9600 kWh from a single turbine. In the same year, a New Jersey Barrier concept was suggested to be useful for harvesting induced wind-traffic [10], fig. 1.10. About 14 years later, the proposal is the same of [1], with the substitution of the original Savonius rotor with helicoidal Darrieus lift-type machines.

We have found many other concepts: see the *turbine light* of Schwartz [11] (fig. 1.11) , the *voltaire turbine* of San [12] (fig. 1.12) and the *Green tunnel* concept of Callegari [13] where the energy harvesting unit consists in a board filled-up with micro-turbines to be placed inside a tunnel, (fig. 1.13).

In the 2009, Sanna [14] won the Mini Design Award and a reward of 10,000 Euros, [39], with its *City Speed Turbine* design, see figs. 1.14. In 2011 we found the work of Saqr and Musa [40], where discussion on the energy consumption trends in the Malaysian road transport sector is made. Here a picture of the total aerodynamic loss of the Malaysian road system is presented and the idea of use wind turbines to harvest the energy is sug-

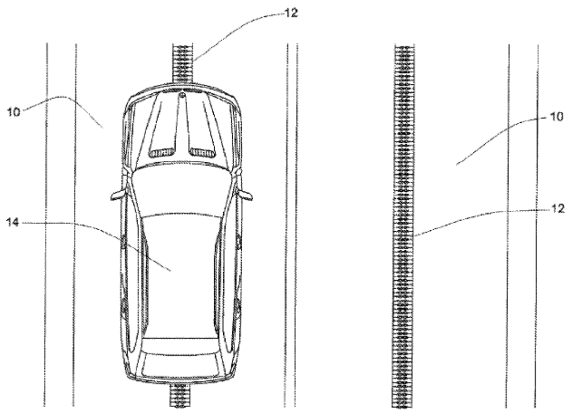

(a) Street plane view

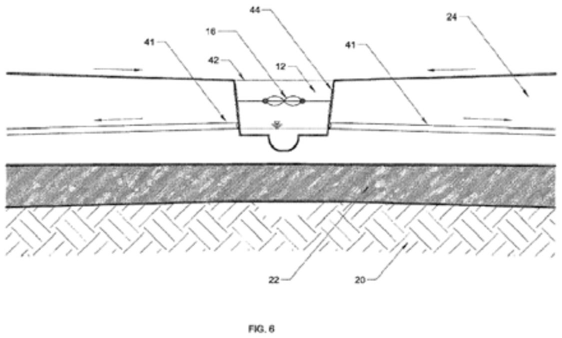

(b) The cavity section with rotor assembled inside

Figure 1.7: Figures extracted from [7]

gested.

Even if all the aforementioned references are a proof of the increasing interest in trying to harvesting energy from such kind of induced-flows, we have not found any real application of the cited concepts, at least in the author knowledge. An exception in this sense seems to be a small French company, [41], who placed a multi-stage drag-type rotor on the side of the A6 highway between Paris and Lyon,[15], see figs. 1.15. A direct claim about their interest and skills in designing such a device could be heard

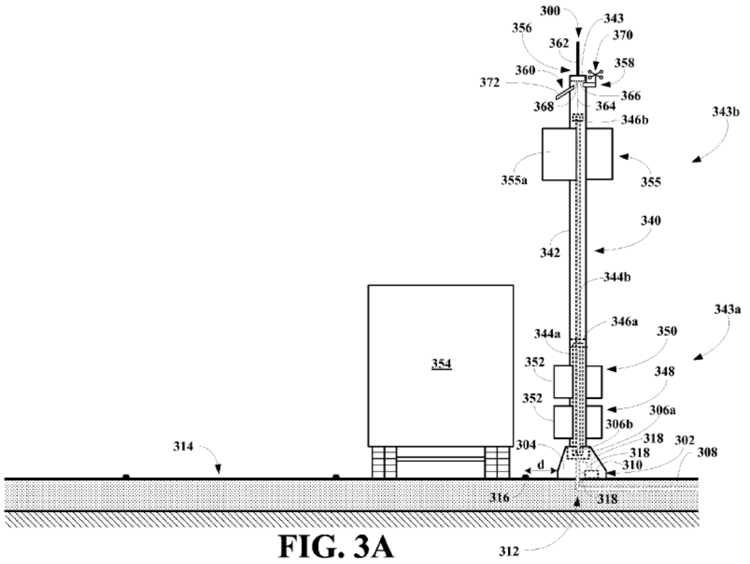

Figure 1.8: A sketch of the harvesting system from [8]

(a) A rendering of the proposed scenario

(b) A sketch of the street plane

Figure 1.9: Figures extracted from [9]

in [42], where it is said that the turbine works primary with the natural wind and is capable of harvesting a fraction of the flows generated by the vehicular traffic. Another company who claims to design devices useful to harvest induced-flows locates in Italy, [43], promoting a three bladed drag-type turbine specifically designed for the purpose. Anyway, in both these

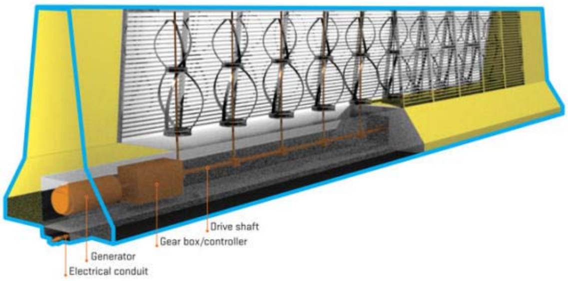

Figure 1.10: the New Jersey concept proposed in [10]

Figure 1.11: the *Turbine light*, from [11]

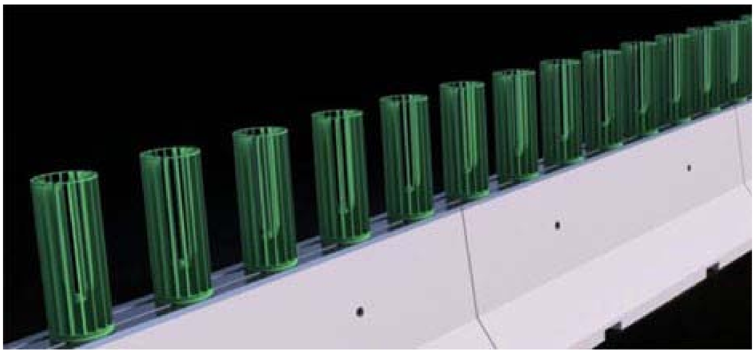

Figure 1.12: the New Jersey design proposed in [12]

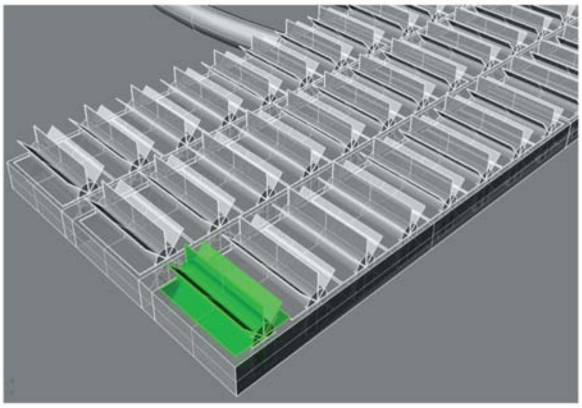

Figure 1.13: the *Green tunnel* unit from [13]

Figure 1.14: the *City Speed Turbine* concept, from [14]

cases, there is a lack in proofs and details about both the used technology and the results of tests in the field.

The last case we cite is the most relevant one, especially because the size of the investment implied. In 2012, the Italian startup Atea won the *EnelLab* 2012 competition patronized by ENEL, [16] the first Italian power supplier (the second in Europe), with a project for harnessing energy from the vehicle induced-flows using a vertical axis wind rotor. ENEL invested 250,000 Euros in the project and a preliminary equipment consisting of a 2,2 Kw Savonius helicoidal rotor was placed in the A4 Brescia-Padova highway, figs. 1.16. Claim about the first in-field tests is a daily production of about 9 Kwh, sufficient to satisfy the yearly energy consumption of a middle-class

(a) the Savonius-type turbine (b) details of the turbine

Figure 1.15: Figures extracted from [15]

Italian family. Furthermore, from the article of Luna [44], published in May 2013, we read that other 400,000 Euros are to be invested in the project according to the final experimental results of the master plan.

Figure 1.16: The in-field installation, from [16]

In the context of the harvesting process applied to the airflows induced by moving road vehicles, all the aforementioned references depict a twofold scenario. On one side, we found strong proofs for the interest of both public and private subjects on this very special issue. On the other side it is clear the lack of a scientific approach in both defining the proposed resource and the effects of some harvesting-process on the vehicles (i.e those who really provide the energy one is trying to harvest). Therefore, some of the basic questions need to be answered are: is the effect commonly felt in proximity of a passing vehicle due to air gusts? Are there other physical effects useful for harvesting energy purposes? If so, how much energy is possible to scavenge? The present work aims at creating the fundamentals of such a matter, taking always in mind the harvesting paradigm, i.e. the need to convert wasted energy without interfering with the primary process from where this energy comes. This is the cornerstone upon which is based the whole work presented here.

Objective of the present work

The present work is organized as follows:
Chapter 1: consists in this introductory part of the work with presentation of the known references dealing with the problem of harvesting energy from the road vehicles induced flows. Here some considerations arise dealing with different aspects and issues related to the use of a wind generator to exploit the energy content of the proposed resource.

Chapter 2: in this chapter general results about the vehicle transit effects on the surroundings are presented, none of this coming from dedicated literature because no specific studies have been found dealing with the energy harvesting process applied to vehicles induced flows. Attention and results come mainly from works on road sign resistance, some insights being captured anyway with accuracy and wealth of details.
Moreover, a detailed survey on CFD tools basing on actual literature is here presented and the main approaches in modeling truck aerodynamics explored. A feasible CFD analysis requires the correct approach to be tailored with respect on the pursued objective and a clear choice is done after considering both performances and code simplicity.

Chapter 3: this chapter focus on the objectives and methodologies pursued in the present work. Description of the choices and explanations about the planned steps of the study are here completely analyzed and shown in their details. Here we present the validation for the method used in the unsteady CFD simulations as well.

Chapter 4: this chapter present major results coming from all the activities described in the previous chapter. Results of the bibliographic research about the energy balance and of all the numerical activities performed are presented and comparison among them showed in terms of velocity profiles, pressure fields, drag coefficients and wasted powers as well. Furthermore, results about the problem of the vehicle-device interaction is presented along with details about the structure of the assumed resource.

Chapter 5: this chapter relates to a simplified approach planned to asses the start-up capabilities of a wind rotor when subjected to the induced wind generated by the moving vehicle. Before starting any evaluation of the energy potential thet a wind turbine could harvest from the considered resource, a study of the starting capabilities of the machine from the rest condition are mandatory and both the no-load and load condition explored by integration of the Newton second low for rotation. Results for the feasibility of the analyzed technology are presented here.

Chapter 6: this chapter relates to conclusions about the present work and some suggestions about future perspectives in the field.

Chapter 2

Phenomenological Aspects and Basic Tools

In every day life, in modern industrial countries at least, everyone is forced to experience human-vehicle interactions of different kind. In particular, everyone could give descriptions about the sensations felt as a consequence of a road vehicle moving at high speed, but the basic phenomena involved with such an event need to be analyzed with a scientific approach.

The energy content that a vehicle put into the air when it is moving is directly related to its drag coefficient, hence mainly on how it is streamlined. In order to explore the most favourable energetic scenario from the point of view of the harvesting process, we concentrate on heavy-vehicles, i.e. on trucks. Among all the types of road vehicles, trucks are those that suite best our target because they are basically bluff-bodies, showing the higher values of drag coefficient and hence energy input into the air.

The first section of this chapter aims at disclosing the physics underneath the fluid flow generated around a moving truck, with special emphasis on its surroundings rather than on the vehicle itself. For this purposes a deep investigation is performed basing on the available technical literature results.

After the bibliographic study, our research could start in defining and quantifying the assumed resource. The higher-level tool selected to perform these investigations is *Computational fluid Dynamics* or briefly, CFD. Therefore, in order to make a correct selection among all the available numerical methods for simulating truck aerodynamics, in the second section of the present chapter we present a survey on modern CFD approaches. Here, comparison among numerical predictions of different codes are presented with special emphasis on the aerodynamics of the two major truck shapes investigated in literature. At the end, a specific choice on the selected CFD approach is then motivated.

2.1 Effects due to road vehicles

Actual technical literature lacks completely of studies of the flow fields induced by moving vehicles for energy harvesting purposes, therefore available information need to be searched elsewhere. In practice, research on the premature failure of the USA type cantilevered traffic signal structures and deficiencies in the UK design standards on road signs give us the opportunity to obtain a lot of details about what happens to an object placed in the proximity of an high speed vehicle. In the last 30 years not many works have dealt with such problems and today authors still seem to refer specifically to a few of these, especially those of Cali and Covert [18] and Quinn et al. [19] for the reliability and size of their experimental databases. These works are quite recent and other studies where carried out in the past, the first known being that of Creamer et al. [45] who modeled the pressure distribution on the road sign surfaces using the field-measured stresses between structure members. In the presented works, to find a reliable design criteria, tests and simulations were to be performed for the worst case scenario i.e. the transit of a bluff body vehicle, that is, a truck. A review of the work done in the field of induced gust loads on cantilevered structures can be found in the work of Albert et al. [46]. Nevertheless, this section deals with other interesting articles, especially that of Baker et al. [17] where the flow field around a model of a lorry is tested. Note also that many of such works relate to scaled models hence they have to be considered with caution: with scaling, results often do not match our range of speed cases but are considered to provide reliable basic features anyway.

2.1.1 Evaluating horizontal loads on a model highway sign

In the work of Baker et al. [17] the slipstream and wake of a 1 : 25 scaled model lorry are investigated, see Fig. 2.1 for a sketch of the vehicle shape. The experimental apparatus consisted in a 8-unit rake of hot TSI anemometers to be placed on both the vehicle side and roof. The rake allowed authors to measure velocity profiles in the motion direction with a sampling rate oh 4000 Hz. Flow velocity and time are made non-dimensional basing on vehicle speed U and truck length L, hence the lapse in the reduced time Ut/L between 0 and 1 represents the time interval needed to overcome the measuring station, the origin being the time the vehicle nose pass underneath. Results prove a strong correlation among the increase in velocity and the passing vehicle, as Fig. 2.2 shows; here, are depicted the non-dimensional velocity histories measured for anemometers 1, 4 and 7 at non-dimensional distances of $Z/W = 0.54, 0.67, 1.02$ from the lorry side (corresponding to full-scale distances of 0.125, 0.375 and 1.5 m respectively) for the 30 m/s speed case (with the rake placed at $Z/W = 90$ mm, just beneath the middle of the vehicle). From such a measures, the authors found that the flow trailed from the vehicle could be divided into five time-regions, each characterized by specific flow features:

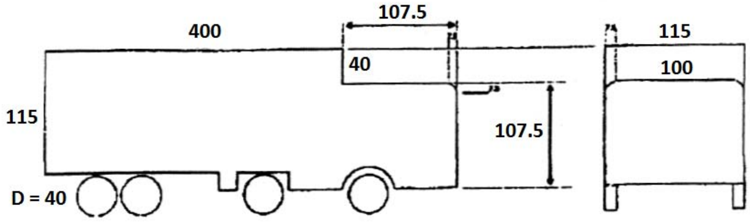

Figure 2.1: The model tested (dimensions in mm), from [17]

- **Upstream Region [UR]** $Ut/L < 0$
  This is the region in front of the vehicle where velocities increase smoothly and the flow behaves as it was inviscid. Side measurements show that the air feels the vehicle arriving at a time of about -1, or in terms of distance, at a fairly 1 vehicle length from the nose of the advancing model.

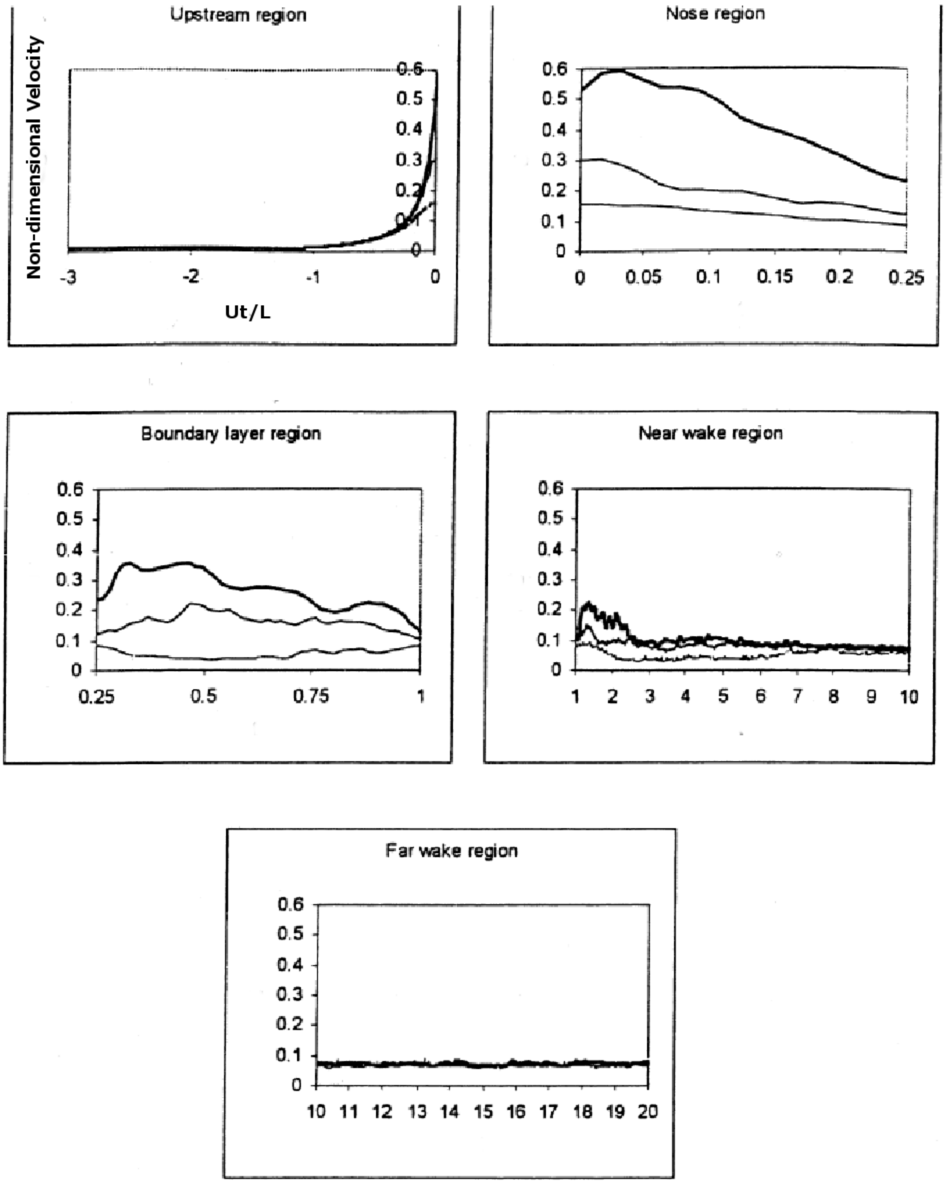

Figure 2.2: Non-dimensional time histories for measured velocities , from [17]

- **Nose Region [NR]** $Ut/L \in [0, 0.25]$
  In this region are located the highest values of velocity that the vehicle could reach. In a lapse, velocity values decrease hence nose and upstream regions are the zones where the highest velocity gradients, or fluid accelerations, locate. Peaks strengths depend from distance, lowering with leaving the vehicle surface.

- **Boundary Layer Region [BLR]** $Ut/L \in [0.25, 1]$
  The potential behaviour ceases here and viscous effects start to dominate, with the formation and develop of boundary layers on the vehicle body. Here velocity variations are slow hence the flow shows low acceleration terms.
- **Near Wake Region [NWR]** $Ut/L \in [1, 10]$
  This zone starts from the vehicle base region and downwards of it velocity profiles show high non-uniformities that decrease in amplitudes with time.
- **Far Wake Region [FWR]** $Ut/L > 10$
  The wake has uniform values of velocity at any section and gradually decay with time (not shown in figure).

Velocity profiles for the side case test of the 30 m/s speed case are depicted in Fig. 2.3. Here we can see how the velocity profiles change with the vehicle transit and note that the higher values locate always at anemometer 1; this is because this anemometer is the nearest to the model surface where the no-slip condition forces the air to move at the same speed of the vehicle. From these figures we note also that the air never exceeds 0.6 time the vehicle speed.

Acceleration terms, related to the induced flows of Fig. 2.2, are computed integrating the velocity time histories evidencing the effects on objects placed nearby the vehicle way, see Fig. 2.5. As can be seen, acceleration curves show a variation with a change in sign around the zero time, i.e. on the vehicle nose, while oscillations of minor strength appear especially during the transit event. In reality it is expected that the presence of an object, depending on its shape and size, affects the interaction with the vehicle providing a resulting flow-field where both the object and the vehicle mutually interact exchanging forces and moments. Finally, the authors claim that the wake varies with a law decay of non-dimensional velocity proportional to t^{α}, where the exponent α for each anemometer is depicted in Fig. 2.5 for the 30 m/s speed-case. Here we can appreciate how the roof exponents (R30) are higher in absolute with respect to those of the side case (S30), meaning that in the upper part of the vehicle the air goes to rest more rapidly than on the sides, anyway curves resemble in the general trend.

Cali and Covert [18] made experimental measurements of the loads on a 1 : 30 scale model of a overhead highway sign with varying sign height, truck

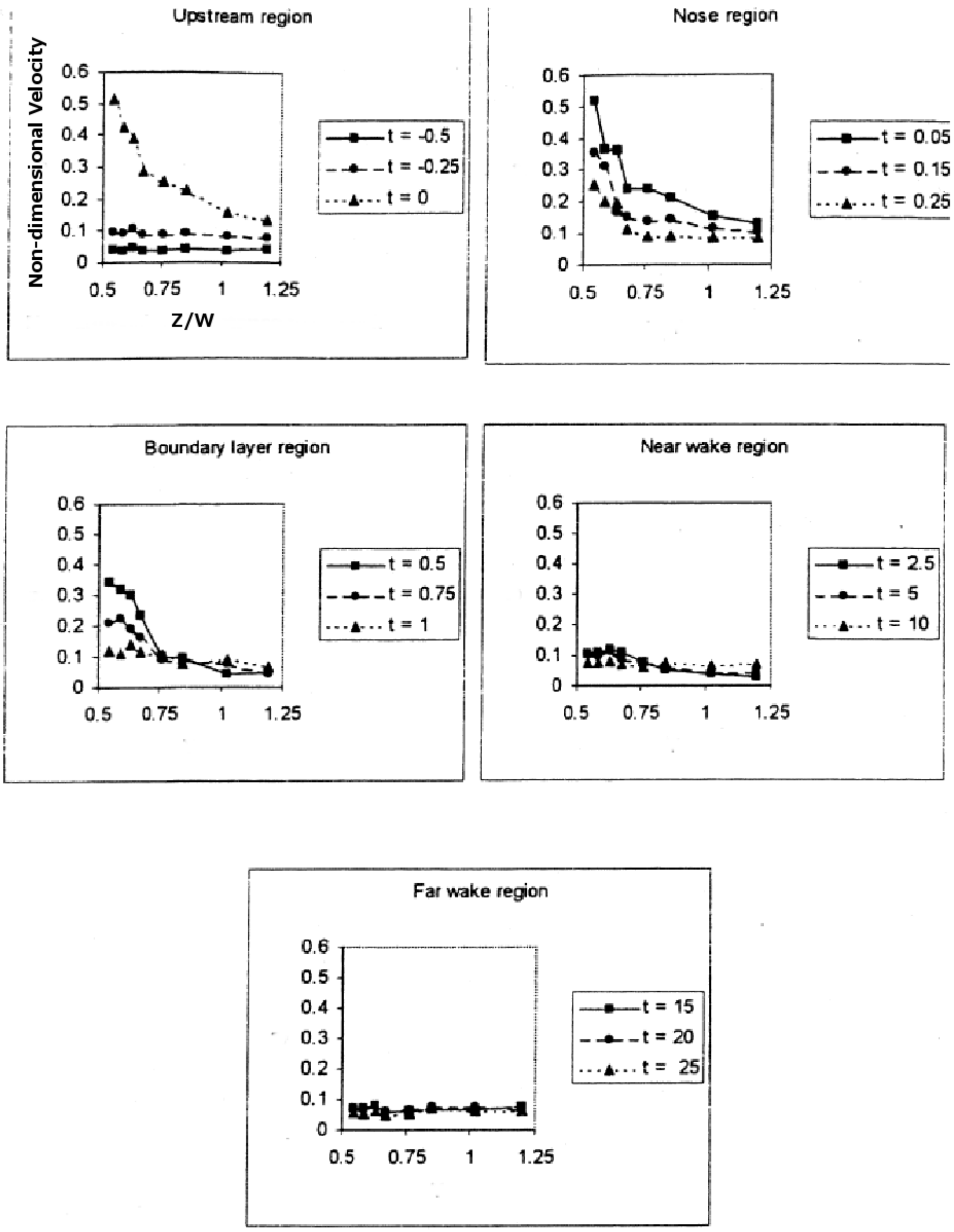

Figure 2.3: Non-dimensional velocity profiles, from [17]

length, truck speed and truck shape. The sign was set perpendicularly to the direction in which the vehicles move (this is why measured loads are said to be longitudinal or horizontal) and mounted on a rigid frame using three pre-compressed load cells allowing to measure both positive and negative

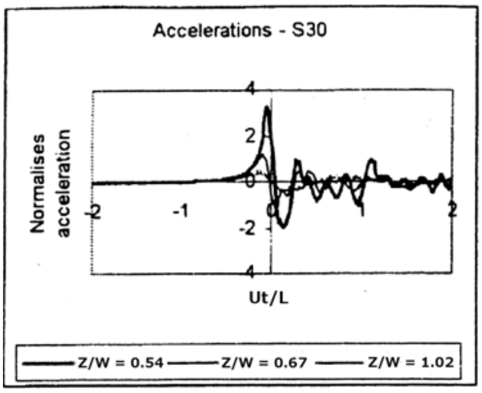

Figure 2.4: Non-dimensional acceleration history, from [17]

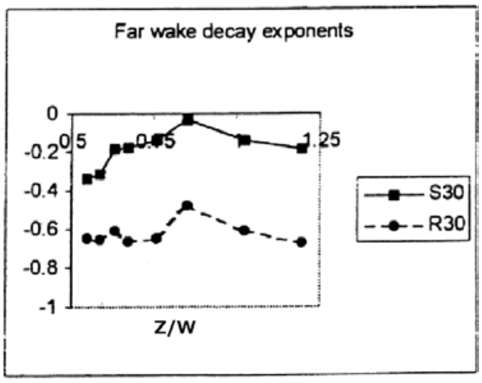

Figure 2.5: The wake decay exponent trends, from [17]

loads as the vehicle passed underneath (each test consisted of 14-18 runs of the same case at still air conditions). The geometry of the rig, together with the cell set-up, are depicted in fig. 2.6 while Tab. 2.1 refers to the test matrix adopted.

From Tab. 2.1 one can infer that only two vehicle shapes were tested: they were the "box" and the "source" types referring to a rectangular parallelepiped and the half-Rankine body respectively. The latter comes from the stagnation streamlines formed superposing a source plus a uniform stream in a potential flow. With this choice authors focused on the range where real vehicles loads were supposed to fall, the streamlined shape expected to provide the lower induced effects. Anyway, both shape types had the same

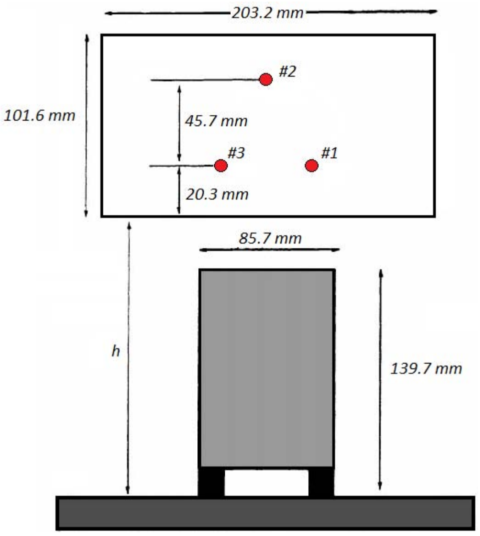

Figure 2.6: Rig geometry

Table 2.1: test matrix from [18]

Test case	Vehicle shape	Vehicle length [cm]	Sign height [cm]	Speeds [Km/h]		
A	Box	61	18.4	39.5	30.5	21.5
B	Box	idem	idem	34.8	28.3	23
C	Source	91	idem	34.4	29.6	25.1
D	Box	idem	idem	32.8	28.2	25.8
E	Box	idem	16	33	28	26
F	Box	idem	21	33	28.3	25.6

hydraulic diameter. Provided that velocities were held constant underneath the sign and through the aid of a photocell placed at sign position to collimate each time-history event, the authors were able to calculate the total force coefficient C_f defined as the sum of the single cell coefficient C_{fi} as follows

$$C_f = \sum_{i=1}^{3} C_{fi} \tag{2.1}$$

$$C_{fi} = \frac{F_i}{1/2\rho U^2 S} \tag{2.2}$$

where ρ, U and S are the air density, vehicle speed and panel area respectively, with F_i the force measured from the $i-th$ cell.

Experimental results allowed Cali and Covert to find characteristic features of the measured loads irrespective of the vehicle type considered, fig. 2.7 depicting the typical force coefficient time history found. As can be seen, the abscissa is the non-dimensional time Ut/L deduced using the vehicle speed and length as scaling parameters; therefore, at the origin the vehicle's leading edge is exactly beneath the sign, while at the value of 1 of the reduced time the trailing edge of the vehicle is just passed by. The curve has five peaks (points from P_1 to P_5) and four zero-crossings (points from Z_1 to Z_4) whose position and magnitude depend in different ways on the parameters investigated.

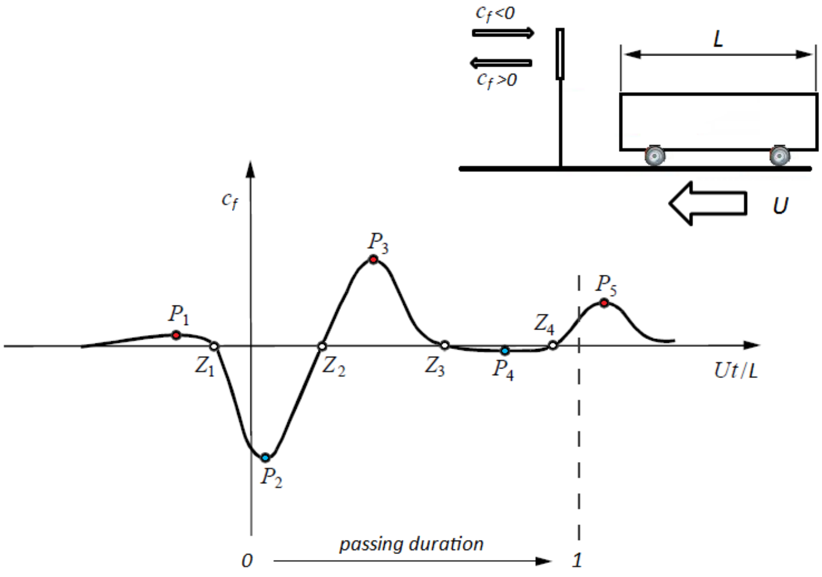

Figure 2.7: Typical force coefficient time history

The relevant features are the following:

- the sign-vehicle interaction starts before the vehicle arrives at the sign position and ends after it has passed by, maxima P_1 and P_5 being external to the transit event duration

- the greater load occurs just after the vehicle's leading edge has passed the sign, being directed in the opposite direction of the truck movement ($C_f < 0$, negative peak P_2)

- after P_2 the load reverses, reaching peak P_3

- between Z_3 and Z_4 zeros the load in practice ceases

The effects of the parameters investigated led to the following results:

Vehicle length (L)

with varying vehicle length, the time region of fig. 2.7 can be split in two, the zone on the right of Z_3 being the only one dependent from L, whilst that on the left depends from the hydraulic diameter.

Sign height (h)

- by lowering the sign height, load amplitudes become greater while the variations with time become steeper, as the narrowing amplitudes of the bell-shaped curves show in fig. 2.8 when shifting from case F to E.
- at the same time the Z_1 cross moves toward the origin proving the *potential* nature of the interaction at P_1. In fact such a behavior agrees with the simple model of a cylinder moving in a fluid at rest, see fig. 2.9(a), as shown in fig. 2.9(b) where test C and the theoretical values from this potential model are compared.

Vehicle shape (Box or Rankine half-body)

- varying the vehicle's shape allows to explain the strong variation in load from peaks P_2 to P_3; in fig. 2.10 the "source" (test C) gives

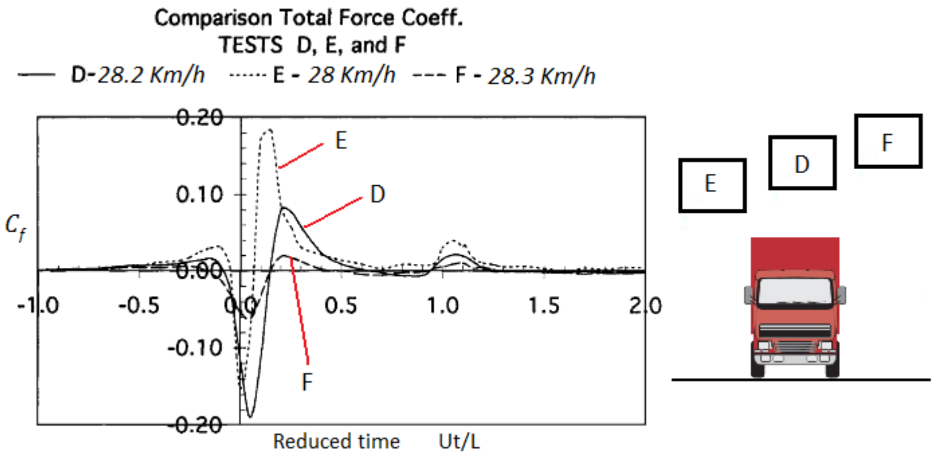

Figure 2.8: The effect of varying sign height

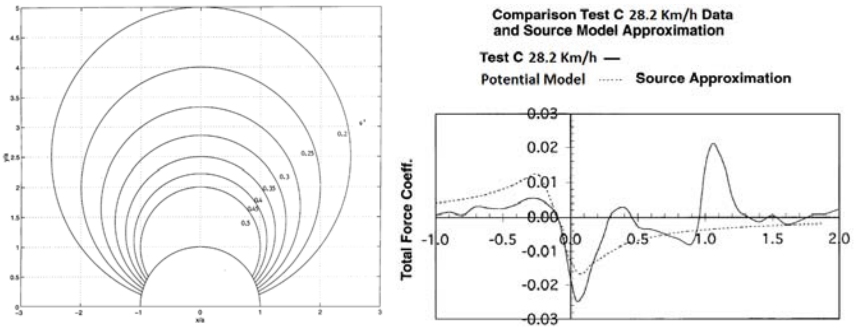

(a) Streamlines for a moving cylinder

(b) Loads comparison

Figure 2.9: Source vehicle experimental data VS simplified potential model

a negative load value close to zero just on the right of the origin, point P_3 being zero in practice, while the boxed vehicle (test D) shows much higher loads in the same region. Through the aid of a theoretical model the authors demonstrate that such a difference comes from the direct interaction of a separation bubble in the upper part of the vehicle with the lower part of the sign, with the lowest effect due to the streamlined shape of the source vehicle, irrespective of the same hydraulic diameter of the two. Therefore, what really matters is how a vehicle is streamlined, or in other words, how is detached the flux upon the vehicle roof. Such an effect was proved varying the sign height because, as depicted in fig. 2.8, heightening the panel the momentum exchange between the bubble (that moves at vehicle speed) and the sign surface decreases. This is why the authors suggest a linear decrease in load within the bubble interaction zone while a potential flow rate of decay with the minus 4 power in the outer region. Nevertheless they noted that further investigation was needed to support such hypothesis.

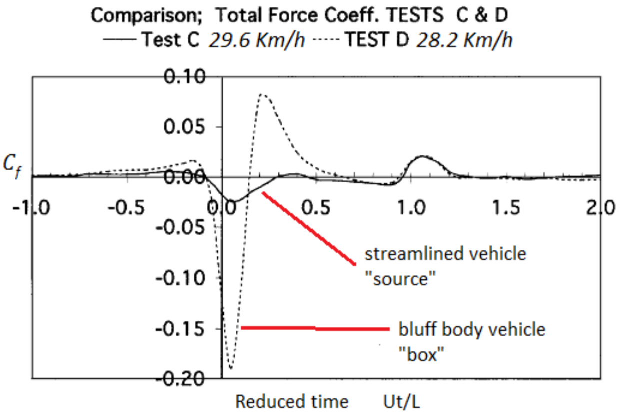

Figure 2.10: The effect of varying vehicle shape

- Fig. 2.10 highlights the influence of the rear part of the vehicles as well: as can be seen, since vehicles had the same length and rear shape, the force coefficient histories overlap in the region on the right of point Z_3.

Note that Cali and Covert refer to a wind-loading mechanism but no experimental data is presented relative to induced flow speeds or pressure fields on the sign. A schematic of the results is depicted in fig. 2.11.

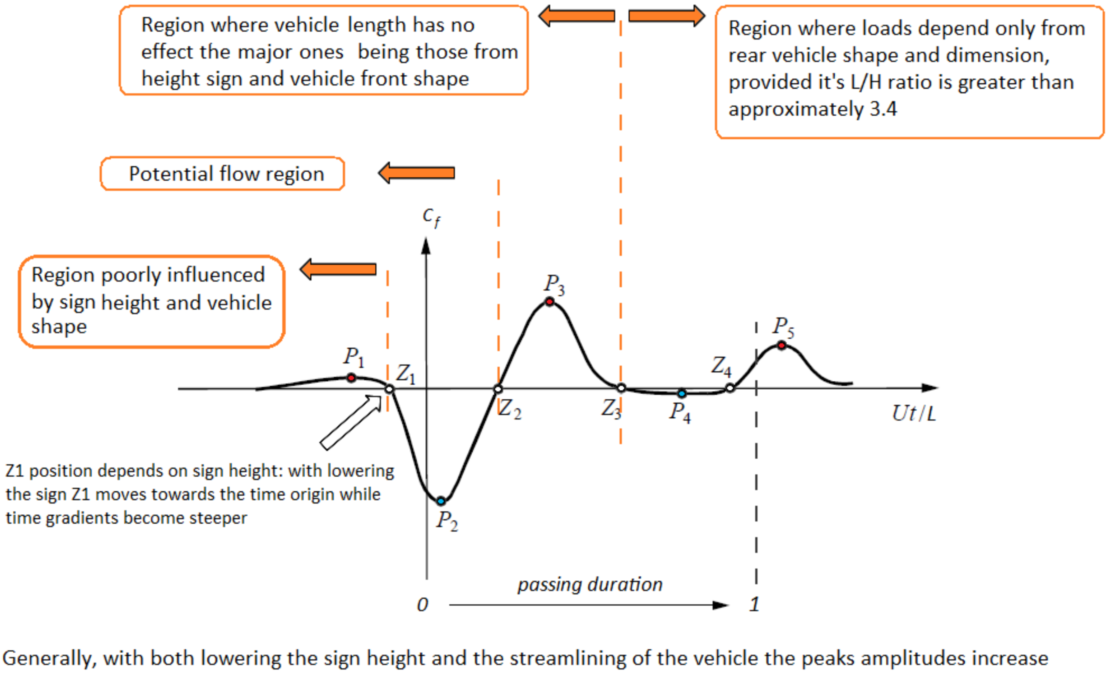

Figure 2.11: Sketch of the main results from [18]

2.1.2 Full scale measurements on road-side signs

Unlike the work of Cali and Covert, that of Quinn et al. allows to shed light onto the phenomena responsible for the vehicle induced loads; their experimental apparatus was used to evaluate longitudinal loads on real signs of different size and shape placed at the side of the carriageways of two different roads. Panels were mounted on a rigid frame through three load cells (as done in the scaled test of Cali and Covert) and both static pressure and wind speed measurements were made using an omni-directional probe and an ultrasonic anemometer mounted upwind at the same nominal height of the sign.

From preliminary tests, they found that wind and vehicle effects could be treated separately (to first order) and especially that *the vehicle-load induced component is due to the pressure field related to the potential flow region of the vehicle slipstream, rather than a significant vehicle induced gust effect.* Such a result was supported by the subsequent roadside tests, as fig. 2.12

clearly shows: as can be seen the measured average wind speed is unaffected by the vehicle transit and a neat pressure event appears as the real cause of the panel load. An example of the measured total load coefficient trends (defined as in Eq. 2.1) is depicted in fig. 2.13. As can be seen, the load coefficient trends support what found by the scale model measurement of Cali and Covert even if the region of loads after the Z_2 cross (see again fig. 2.7 for point nomenclature) seems to have disappeared, the authors explaining this according to the number of vehicle events accounted for in the averaging process. Note that the load history is shown as function of time and not of a reduced variable.

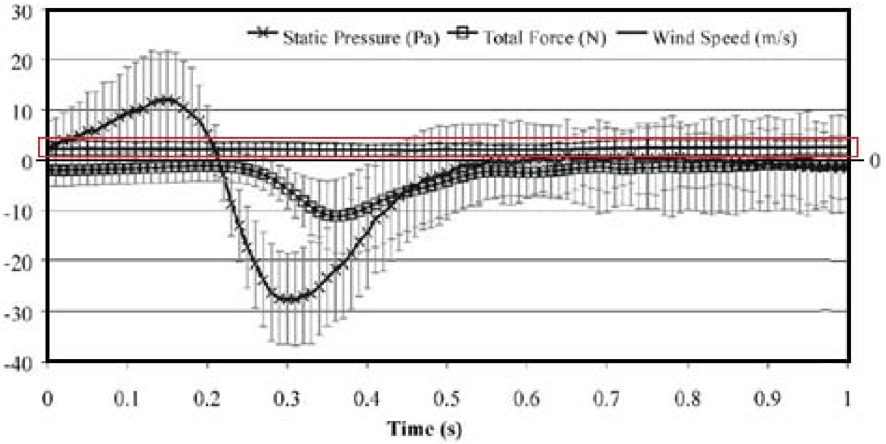

Figure 2.12: Example of an ensemble average measurements for a square sign placed at 1,5 m distance from the closest passing vehicle. Red box: wind speed measurement

From the same data, the authors were able to suggest a load decay with the minus 2 power of distance from the vehicle, as fig. 2.14 shows. The major point of discussion in this work consists indeed in the ensembling procedure: field test measurements were done according to real traffic events and so the selecting criteria need to be chosen among vehicle events to give reliable load-history. To exclude the lowering contribution of smaller vehicles, the authors only considered pressure events with maximum suction pressure above 18 Pa, so results are affected not only by the number of events considered but by the cut-off pressure chosen as well.

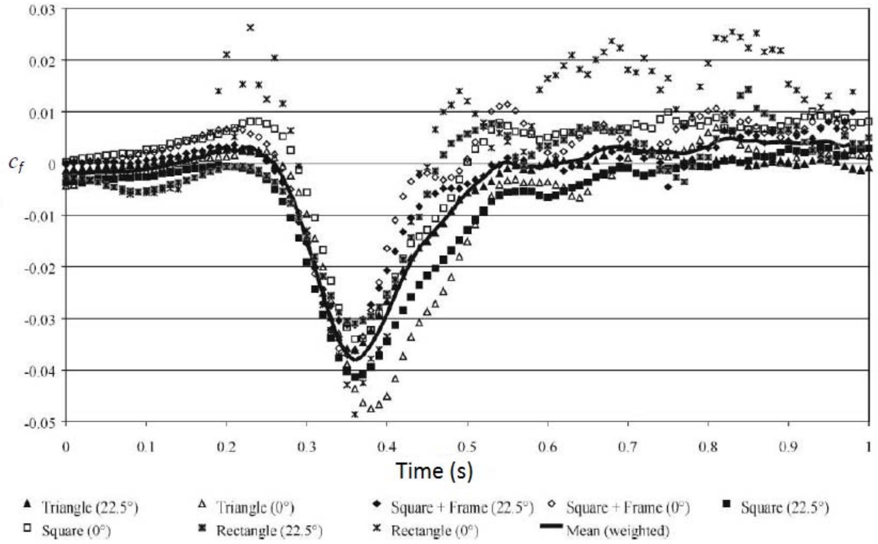

Figure 2.13: Typical load coefficients found by Quinn et al. in one of the road sections considered

Another interesting result comes from the measurements of the loads on pedestrian barriers, as depicted in fig. 2.15, with both perpendicular and parallel placement relative to roadway direction. As can be seen, a persistent negative load appears for the latter case in which the barrier is first pushed-out from the street and than pulled-in with a positive peak that resemble in magnitude the negative one of the perpendicular case.

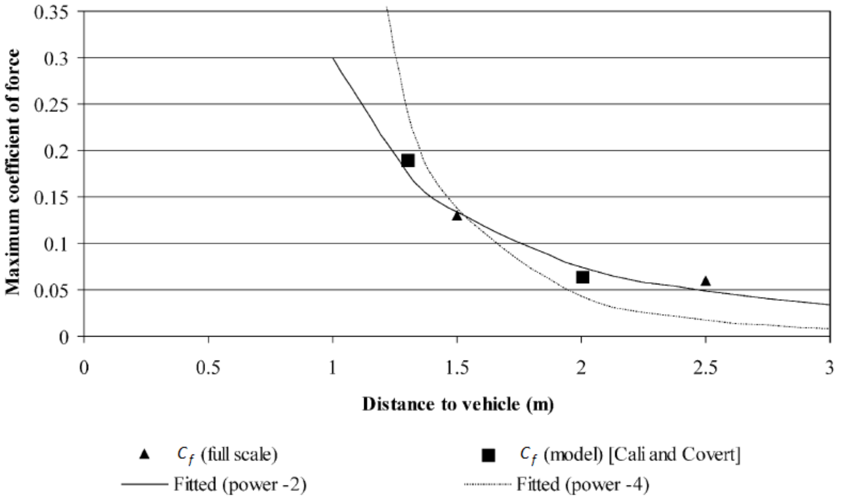

Figure 2.14: Maximum suction peak dependance with separation distance from vehicle

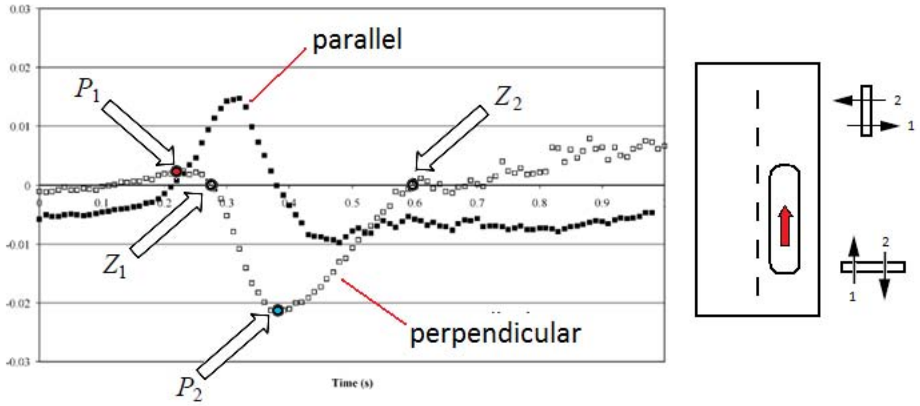

Figure 2.15: Load coefficient for pedestrian barriers placed perpendicular (empty squares) and parallel (filled squares) to the roadway direction

2.1.3 Validating data with both recent theoretical and experimental tests

As shown, experimental evidence supports dividing load time-histories in two regions: the first generated by the transient pressure field due to a potential unsteady flow and the second one governed by viscous-wake pressure effects, as depicted in fig. 2.11. On these basis, succeeding efforts were made to develop potential models capable of describing the nose-interaction zone of the vehicle, especially because the higher loads concentrates here, for bluff bodies at least. The work of Sanz-Andrès et al. [47] deals with such an approach: simulating a three-dimensional potential flow and making several hypothesis on the flow itself they were able to reproduce the load trends found by both Cali and Covert and Quinn et al., see figs. 2.16(a) and 2.16(b). With respect to the "source" vehicle of Cali and Covert, the potential output agree in both qualitative and quantitative terms, unlike the results of Quinn et al. where calculated trends agree only in shape (the authors pointed out that for pedestrian barriers - see fig. 2.15 - the model gave the worst load prediction). This fact is not a surprise at all because the theoretical code models the vehicle as a moving source reproducing the vehicle front shape used by Cali and Covert. Moreover, fig. 2.16(a) give evidence of the wake effects, because at reduced time $T = 4$ (here reduced time is defined in a different way as by Cali and Covert and for comparison data were converted first) the wake peak appears, clearly not reproduced by the potential model. Finally, unlike what pointed out in the experimental works considered, the potential model presents a load-decay law varying with the minus 3 power of separation distance. With respect on such a law, the experimental work of Sanz-Andrès

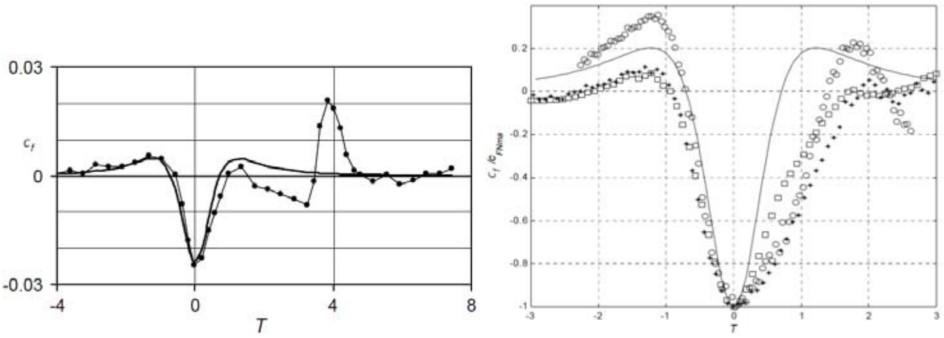

(a) comparison with results from [18]

(b) comparison with results from [19]

Figure 2.16: Potential model approximations (solid line) and comparison with experimental data (dots)

et al. [48] confirm the -3-rd power dependance. In their recent report they describe the centrifuge-rig developed with the aim of investigating vehicle induced effects, with attention devoted only on nose interaction. Preliminary tests used the "source" shape of Cali and Covert allow the authors to find load trends in good agreement with those of the aforementioned potential model results as, for example fig. 2.17 show.

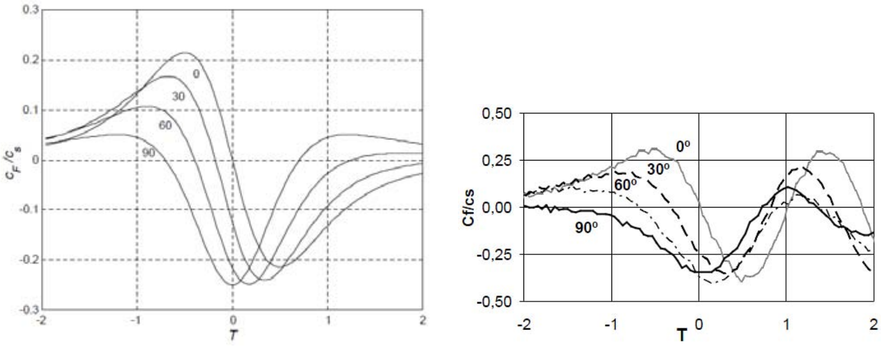

(a) potential model data from [47] (b) experimental data from [48]

Figure 2.17: Comparison between normalized load coefficients on a flat plate with varying the sign angle with respect to track direction.

When

2.1.4 Conclusions about phenomenological aspects

Previous section presented a resume of the available data on road vehicle induced-flows and effects on obstacles of different sizes and shapes. Both experimental and theoretical data support that an high-speed vehicle induces loads on local bodies due to a moving pressure field rather than a consistent wind-gust effect, despite the common sensation felt when placed near the vehicle way. Moreover, this pressure field is based on different mechanisms depending on the part of the vehicle considered: the front part generate a flow whose features are mainly potential in nature (irrespective of vehicle's frontal shape) while directly behind this region, viscous effects take over in the form of separation bubbles, if any, and wakes. The existence of a potential region near the vehicle is of interest for the one who is trying to harvest energy from such a process. As a matter of fact, the viscous region is expected to be unaccessible to any harvesting device because shear-stresses and other viscous effects are considered to grow in this case, possibly slowing down the vehicle. Therefore a deeper investigation is required with the aim of identifying the boundaries of these two main regions and to see how the presence of intrusive surfaces could alter the truck motion. This is why the next section is entirely devoted to the CFD codes comparisons and selection.

2.2 Exploring truck's aerodynamics with CFD

As pointed out in the previous section, actual literature lacks for specific surveys on induced flows by truckage, whilst a lot of studies exist relating to the aerodynamics of vehicle in general, and on trucks in particular when focusing on fuel savings strategies. In this field CFD codes starts to give their contribute recently and use of external devices to reduce total drag are investigated with the aid of such new approaches. This section catches the main characteristics of such codes and their performances when applied on trucks, allowing to identify the best approach to be pursued at a deeper level of this study and to present the standard shapes investigated in the scientific community. It is worth to note here, that we are interested in the *absolute flow* as seen from the one who is at rest in the street frame of reference, rather than in the *realtive flow* seen by the driver of the truck. The latter point of view is that pursued in all the works below and in aerodynamics studies in general, but this is not a problem; the absolute flow is derived from the relative one by subtraction of the truck speed, hence CFD results and worth are the same and generalities on codes could be extended to our specific case as well.

2.2.1 Analysis made on simplified truck shapes: the GTS and GCM models

In the USA exists two major classifications for trucks, both based on the *Gross Vehicle Weight Rating* ($GVWR$), representing the sum of the vehicle's net weight plus those of fuel, cargo and passengers. The first one is defined by the US government and consists in weight classes ranging from the lighter Class-1 to the heavier Class-8; at the same time, a broader classification is defined by US DOT Federal Highway Administration ($FHWA$) Vehicle Inventory and Use Survey ($VIUS$) basing on three categories: Light Duty Trucks, Medium Duty Trucks and Heavy Duty Trucks. Correspondence between classes and weight limits are shown in fig. 2.18(a).

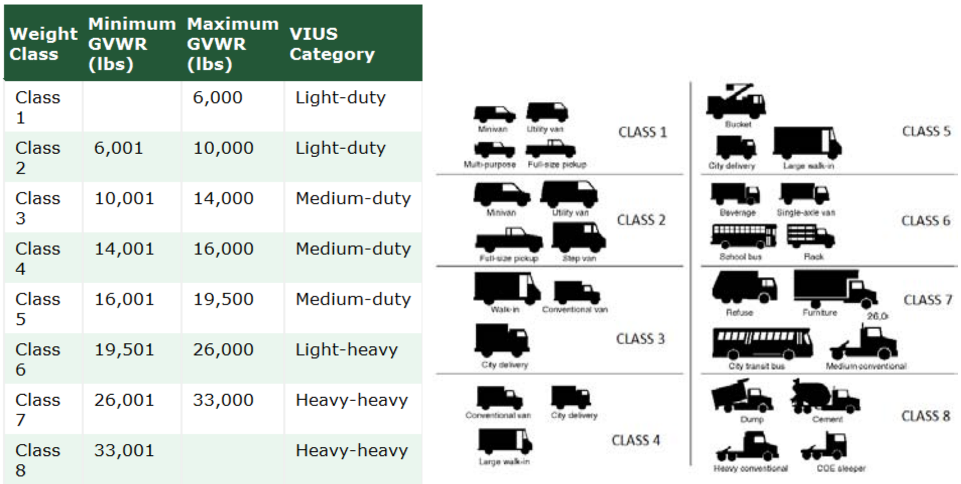

Weight Class	Minimum GVWR (lbs)	Maximum GVWR (lbs)	VIUS Category
Class 1		6,000	Light-duty
Class 2	6,001	10,000	Light-duty
Class 3	10,001	14,000	Medium-duty
Class 4	14,001	16,000	Medium-duty
Class 5	16,001	19,500	Medium-duty
Class 6	19,501	26,000	Light-heavy
Class 7	26,001	33,000	Heavy-heavy
Class 8	33,001		Heavy-heavy

(a) US truck classifications

(b) typical shapes

Figure 2.18: US vehicles classes

As depicted in fig. 2.18(b), each class includes vehicles with very different shapes, as does Class-8 where attention is paid on tractor semi-trailer systems since aerodynamics investigations are mainly directed to improve the fuel efficiency of such vehicles. Among these kind of vehicles, two main tractor design are investigated, both experimentally and numerically: the cab over design (COE) and the conventional design, where the driver is seated behind the engine rather than upon it, see fig. 2.19.

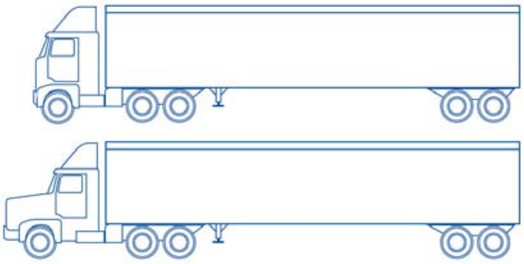

Figure 2.19: Cab designs. Top: COE - Bottom: conventional

Consequently technical literature deals with two standardized Class-8 representing shapes, the so called *Ground Transportation System* or GTS, [49], and the *Generic Conventional Model* or GCM, [50], designed to reproduce in scale (1/8) the generic *COE* and conventional tractors types respectively, see fig. 2.20.

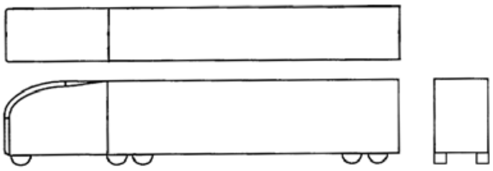

(a) GTS (COE design)

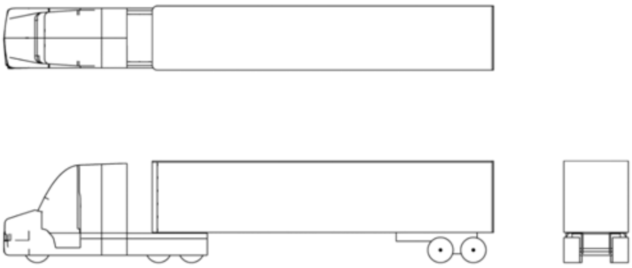

(b) GCM (CONVENTIONAL design)

Figure 2.20: Standardized models used for investigating drag-reduction devices. (Figures depicted in different scales)

Tab. 2.6 presents the main dimensions of these models made non-dimensional with respect to vehicle's widths; comparison between the two is made on the last row where differences are shown basing on the GTS data; as can be seen, differences are due mainly to the lower height of the GCM.

Table 2.2: Models data. L=Length - H=Height - W=Width. (wheels not included)

Model	**Gap**	**Cab only**			**Trailer only**			**Total Length**
	G/W	H/W	L/W	L/H	H/W	L/W	L/H	L_{tot}/W
GTS	0	1.392	2	1.436	1.392	5.647	4.056	7.647
GCM	0.385	1.117	1.917	1.3	1.117	5.293	4.736	7.595
$\Delta_{GTS}(\%)$	-	19.75	4.15	9.47	19.75	6.27	-16.76	0.68

With the aim of creating experimental databases for validating later numerical studies, model shapes were simplified and for both the GTS and GCM vehicles no attempt was made to duplicate real undercarriages, wheel wells, mirrors, small scale surface details or flow-through components. The GCM model reproduce with more accuracy the actual truck shape, see fig. 2.20(b), mainly because it includes the tractor-trailer gap, a region which strongly affects vehicle drag.

The drag is defined as the force opposing to the vehicle's motion, acting in the direction of the motion itself. Generally, depending on both the speed and vehicle's shape several drag contributions arise.

For road vehicles moving at typical speeds the drag force is mainly due to both *pressure drag* and *skin-friction drag.* A deeper discussion about these forces is devoted later, here suffices to say that pressure drag arises because the fluid stagnates in the front of the vehicle and separates in the rear, regions where the flow has pressure values higher and lower than the atmospheric one respectively, giving rise to a net force that suck back the vehicle. Skin-friction drag is viscous in nature and comes from the shear stresses that the vehicle has to overcome within the boundary layers.

The mathematical definitions are the following:

$$C_{dp} = \frac{Pressure - drag}{\frac{1}{2}\rho_r U_r^2 A_r} \tag{2.3}$$

$$C_{df} = \frac{Friction - drag}{\frac{1}{2}\rho_r U_r^2 A_r} \tag{2.4}$$

$$C_d = C_{dp} + C_{df} \tag{2.5}$$

where quantities with subscript r refer to reference values, ρ, U and A being the air density, air speed and the vehicle projected area respectively; often these quantities relates to freestream values and for blunt shapes as in the case of trucks, to the frontal area corresponding to the body as seen from the stream. Actually, skin-friction coefficients are referred to the wetted area, but in order to sum drag contributions, i.e. to write Eq. 2.5, in the present work the reference area for C_{df}s is the same used to define C_{dp}s coefficients. Because of its definition, C_{dp} can be defined also in terms of the *pressure coefficient* C_p, expressing the non-dimensional pressure field, that is:

$$C_p = \frac{p - p_r}{\frac{1}{2}\rho_r U_r^2} \tag{2.6}$$

$$C_{dp} = \frac{1}{A_r} \int_{A_{rear}}^{A_{front}} C_p dA \tag{2.7}$$

where p denotes static pressure values. With such coefficients at hand it' s possible to calculate the related wasted powers with the next :

$$P_i = \frac{1}{2}\rho_r A_r U_r^3 C_{di} \tag{2.8}$$

where index i is used to indicate anyone of the aforementioned coefficients.

2.2.2 Simulations on the GTS model

This section deals with CFD investigations only on the GTS model. As shown in the previous paragraph, this shape is quite simplified with respect to a real vehicle, nevertheless a further reduction is done by researchers for mitigating further the complexity of computations, i.e., the wheels are removed and the vehicle set upon cylindrical pins. Furthermore, in the present work attention is paid on the 0° yaw configuration only, that is, with no cross-winds impinging on the vehicle.

2.2.2.1 RANS simulations

Turbulence modeling with RANS is widespread for engineering applications, providing results of useful accuracy when attached flows are of concern. When the flow separates massively, or large adverse pressure gradients dominate, RANS modeling may provide non-realistic results.

Nevertheless, many efforts were done to assess the effectiveness of such an approach for investigating baseline configurations of tractor-trailer vehicles and drag-reduction devices.

As a matter of fact, many works such as those of Salari et al. [51], R.C. McCallen et al. [52], Roy et al. [21] and Veluri et al. [20] demonstrate that the RANS approach is able to predict pressure fields on vehicle's surfaces except in the base region. Interestingly it is found that although in this zone pressure field and flow structure predictions do not match with experimental data, pressure levels are similar and so vehicle drag is predicted with accuracy depending on the turbulence model adopted.

To show such a conclusion, some results taken from the recent work of Veluri et al. [20] are presented, where both experimental measurements and steady-state RANS simulations are performed, the latter run with the following turbulence models: the standard Wilcox 1998 k-ω model, the SST k-ω model, the standard k-ϵ model, and the Spalart-Allmaras model.

The vehicle investigated by Veluri et al. is shorter than the GTS described in Sec. 2.2.1 due to the length limitation imposed by the wind tunnel used, having a length to width ratio of 3,4 instead of more than 5 of the GTS, and because forward corners are more rounded; this vehicle is based upon the so called *Modified Ground Transportation System* or MGTS designed by Hammache and Browand [53].

Veluri et al. use the $FLUENT$ CFD code to set-up RANS simulations with three grid levels for both the empty tunnel and truck simulations. The computational domain is depicted in fig. 2.21 while fig. 2.22 show comparison between CFD and experimental pressure coefficients for top and bottom surfaces, sides, front and back regions respectively (for interpreting axes coordinates look at the reference system in fig. 2.21).

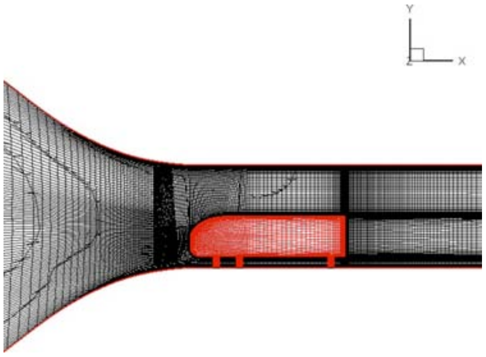

Figure 2.21: Computational domain, from [20]

The predicted C_p coefficients are in good agreement with the experimental measurements except in the rear region, see fig. 2.22(d), where pressure trends strongly disagree. Such a result is consistent with previous RANS simulations; consider for example fig. 2.23(a), taken from Roy et al. [21] for the GTS model, where 2D streamlines and contours of streamwise velocity in the centered vertical plane are presented for both PIV measurements, by Storms et al. [22] (top), and RANS simulations with the Menter k-ω turbulence model (bottom). As can be seen, experimental data reveal a large vortex, while RANS computations predict two counter-rotating vortices suggesting a more symmetrical pattern, as shown in fig. 2.22(d) by the calculated C_p trend as well. Interestingly, Roy et al. found that such a disagreement is due to vertical velocity components mainly, while other components are predicted with more accuracy by simulations, as fig. 2.23(b) shows; here an horizontal streamwise cut of the base region is depicted show-

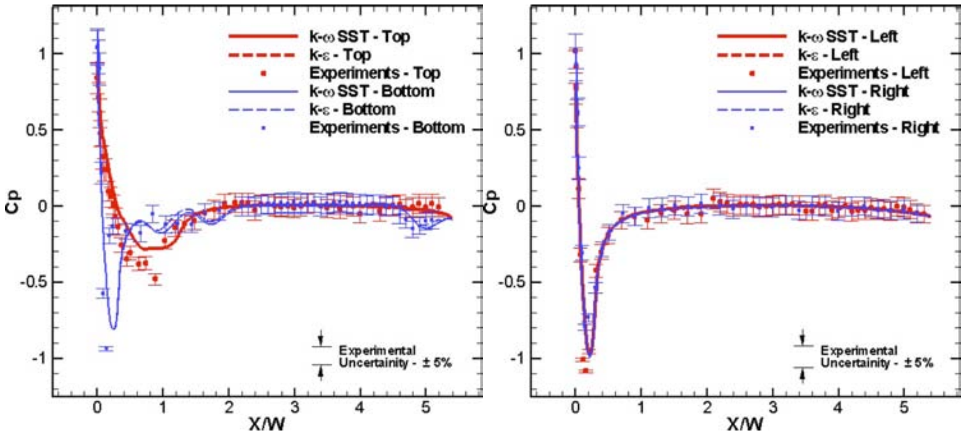

(a) top and bottom (b) sides

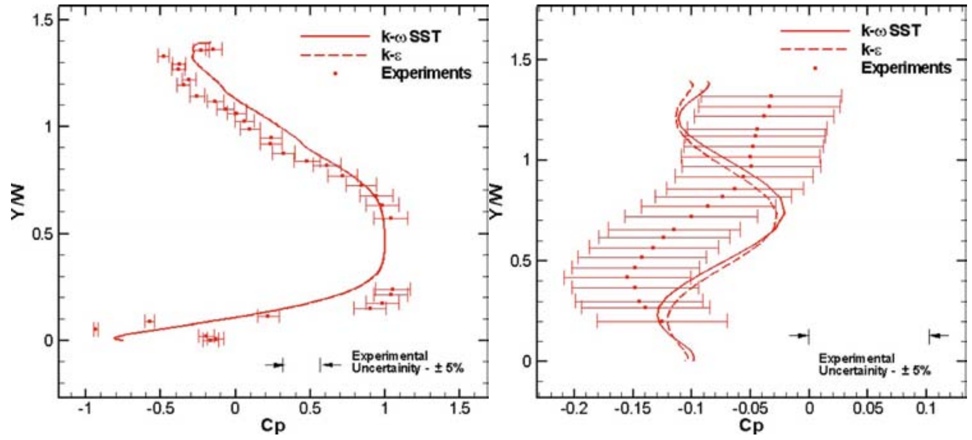

(c) front (d) back

Figure 2.22: C_p variations on MGTS surfaces, from Veluri et al. [20]

ing 2D streamlines and contours of vertical velocity, in this case simulations allowing to identify correctly the vortical structures and their location, even though speed amplitudes are quite different.

Although such discrepancies, the overall drag coefficients are found to be close to the measured ones, as Tab. 2.3 shows for the RANS predictions of Veluri et al., especially for the k-ω model. A list of general observations and guidelines for steady-state RANS simulations can be found in R.C. McCallen et al. [52].

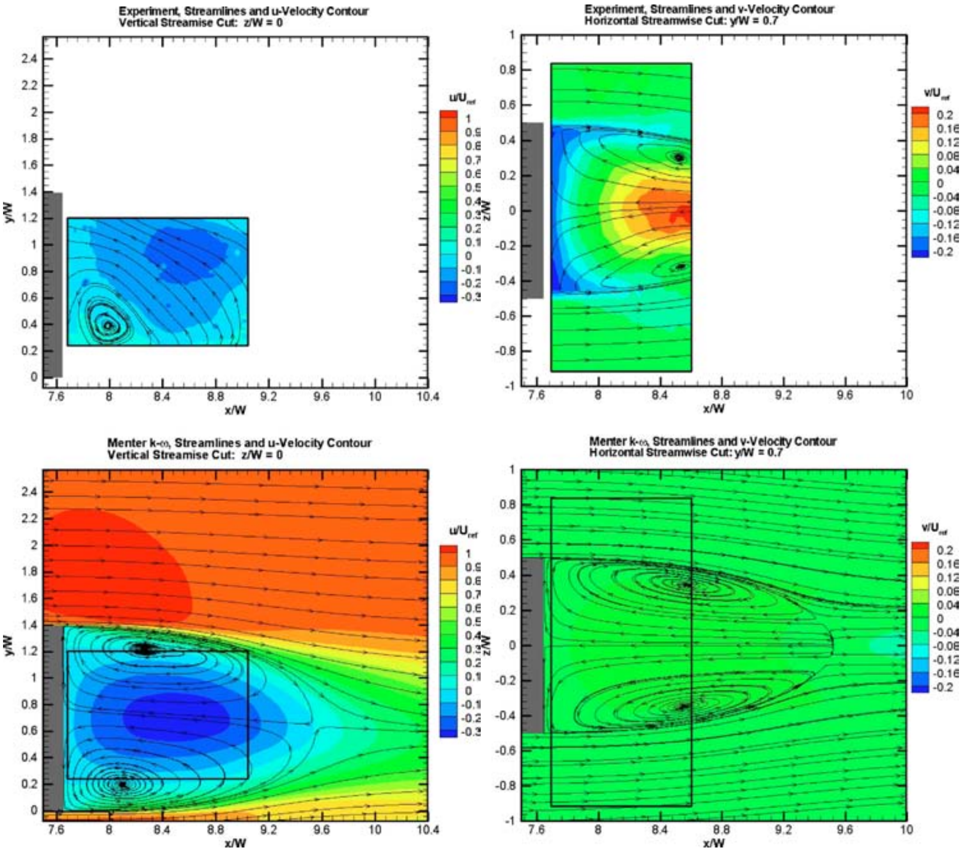

(a) Vertical plane in wake centerline

(b) Horizontal plane at y/W=0.7

Figure 2.23: *PIV* measurements vs RANS predictions in the GTS base region, from Roy et al. [21]

Table 2.3: Drag coefficient comparison with varying turbulence model, from Veluri et al. [20]

	C_d	Error (%)
Spalart-Allmaras	0.3975 ± 0.0249	-22.3
k-ϵ	0.3072 ± 0.0035	5.48
k-ω	0.3089 ± 0.0405	4.95
SST k-ω	0.3003 ± 0.0017	7.6
Experiment	0.325 ± 0.016	-

2.2.2.2 DES simulations

As already pointed, RANS modeling is unable to predict the unsteady flow behavior in the base region and since many studies concentrates in altering the flow in this zone of the vehicle using add-on devices, new approaches are needed capable to catch the flow-features in the wake. From this viewpoint, an interesting approach is the *Detached-Eddy Simulation*, or DES, developed as an hybrid approach between the RANS and LES (*Large-Eddy Simulation*) methods. The aim is to reduce equations to the RANS form in the wall regions where the flow is attached, while in the detached regions closure of the problem is given by a LES approach, whose equations provide higher resolution for simulating 3D eddies.
The work of Maddox et al. [29] deals with the comparison between purely RANS prediction and DES, both working with the Spalart-Allmaras turbulence model. Both approaches are based upon the same grid and no attempt is made to reproduce boundary layer transition, therefore a small level of eddy viscosity is prescribed providing the full-turbulent solution to the problem.
As expected, detached flow regions are described more realistically by DES than RANS, as fig. 2.24 shows, relating to the wake in the rear region of the GTS, while results for drag coefficients are in Tab. 2.4.

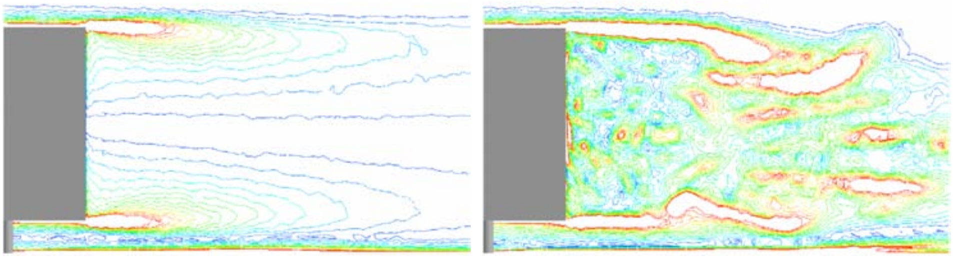

(a) RANS prediction - steady state (b) DES prediction - instantaneous

Figure 2.24: Center-plane wake vorticity distributions for the GTS model

Pressure predictions for both the front and the base region for the two approach are depicted in fig. 2.25; as can be seen, differences arise only for the base region (quasi-vertical curves) where for the DES solution sensitivity to

Table 2.4: Predicted drag and errors, from [29]

	C_d	Error (%)
RANS	0.370	-48.59
DES	0.279	-12.05
Experiment	0.249	-

vertical coordinate is less than that of RANS, a proof of the existence there of a highly separated flow region, not well captured by the RANS approach.

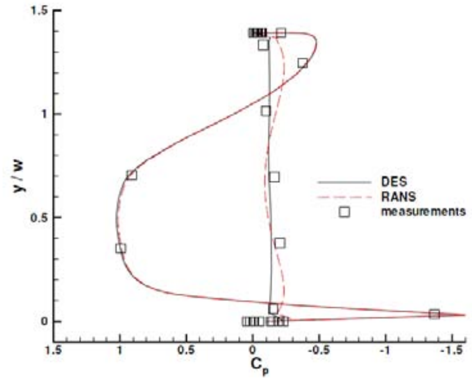

Figure 2.25: Center-plane pressure coefficients. Comparison with experimental values from Storms et al. [22]

DES and RANS approaches are expected to give non-similar results only in separated regions, but not into attached region, therefore for the front of the vehicle it's not a surprise that predictions coincide. This is true for both side and roof surfaces as well, as fig. 2.26 shows, where differences between trends arise only near the wake region at the right limit of the curves.

Despite such promising results many unresolved issues still affects DES simulations, the criterion determining the matching line between LES and RANS domains being one of these.

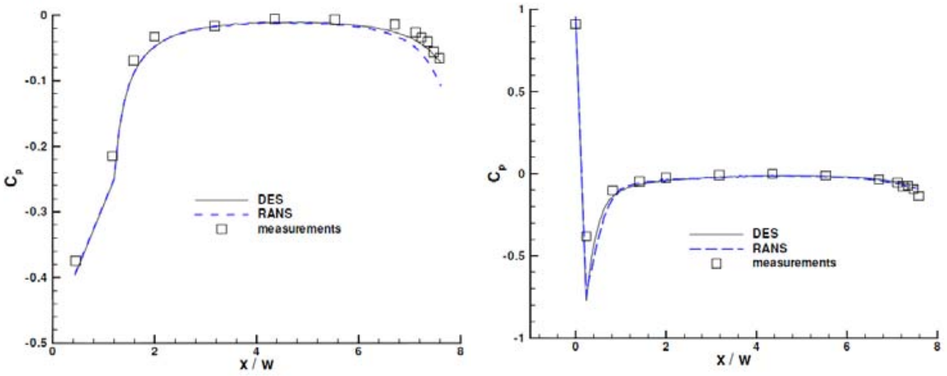

(a) C_p trends on the roof

(b) C_p trends on the side

Figure 2.26: Pressure coefficients for RANS and DES predictions

2.2.3 Simulations on the GCM model

As already noted, the GCM model is more realistic than the GTS mainly because incorporates the tractor-trailer gap, but more attention is required during the modeling process in order to ensure accuracy in vehicle's surface reproduction, since the GCM shape has more details than the GTS; consequently, the GCM model challenges more actual CFD codes, and interesting results from several numerical approaches arise from recent works.

2.2.3.1 RANS simulations

Within the US *DOE* project on the Aerodynamics of heavy vehicles, strong efforts are made to evaluate CFD tools for simulating real truck geometries. In this context the work of Pointer [54] aims at giving general guidelines to make accurate RANS simulations using commercial CFD codes. With this purposes, results on the GCM model without wheels from [54] came from the commercial code *Star-CD*. Focusing on the 0° yaw configuration, the drag coefficients found with varying turbulence model are shown in Tab. 2.6.

Table 2.5: Predicted drag and errors

Turbulence Model	C_d	Error (%)
High-reynolds Number k-ϵ	0.402	1
Menter k-ω SST	0.401	0.8
RNG	0.389	2.3
Chen	0.3919	1.61
Quadratic model	0.3815	4.32
Experiment	0.398	-

As can be seen, C_d values are very close to the experimental one, with accuracy comparable with some RANS simulations made on the GTS by Veluri et al., see Tab. 2.3 in sec.2.2.2.1; more interestingly, in the work of Pointer results are in good agreement also for the base region, where simulations for the GTS with RANS approach generally seems to lack in accuracy, see fig. 2.27. This graph shows that the C_p trends are quite similar to the experimental ones, and as a consequence, good agreement exists for the C_{dp} values as well because of eq. 2.5.

RANS sensitivity to geometry variations in the trailer base region is shown also in fig. 2.27, where the velocity fields of the base-line GCM model (top) is compared with that provided with boat tail device in the rear (bottom); despite what pointed out by virtue of the RANS simulation on the GTS, here steady-state RANS predictions seems to sense the effect of reducing drag devices even in highly separated regions.

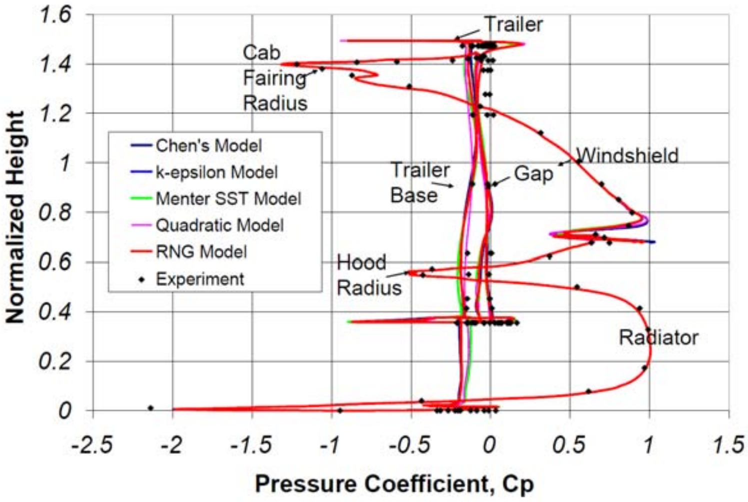

Figure 2.27: Predicted pressure coefficients for different regions of the GCM model compared with experimental values

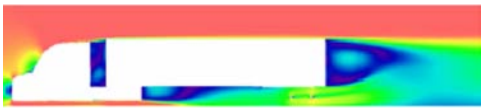

(a) Base-line configuration

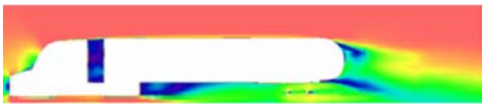

(b) Mod configuration

Figure 2.28: Velocity magnitude predictions

2.2.3.2 URANS simulations

In the work of Hyams et al. [55] is presented a very detailed study on the aerodynamics of the GCM using the URANS approach. The authors work out flow predictions for the 0° yaw configuration using a private code named *Tenasi*, coupled with the one equation Menter-SAS turbulence model operating in DES mode.

Results on pressure distributions along surfaces are in very good agreement with experimental data, see for example fig. 2.29 where both time-averaged and steady state solutions for pressure are depicted; fig. 2.29(a) is the same of fig. 2.28 while fig. 2.29(b) corresponds for example to fig.2.26(b).

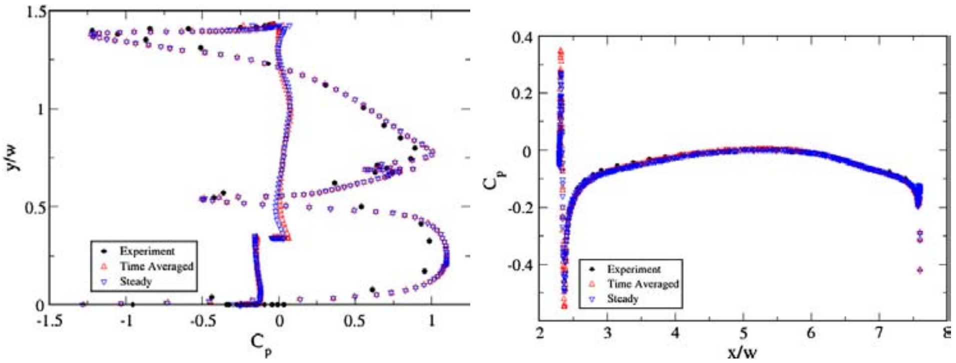

(a) C_p trends:front and rear

(b) C_p trends: sides

Figure 2.29: Velocity magnitude predictions

Results for C_p trends in the base region are depicted in fig. 2.30; as can be seen, experimental values are tracked quite well, especially if compared with the RANS prediction of fig. 2.22(d): in this case no symmetrical pattern is found and predicted values are closer to the experimental ones especially in the lower part of the trailer.

The URANS approach seems to work better, anyway the RANS modeling competes quite well as shown in the previous section, and in this perspective, the work of Salari et al. [56] consist in a comparison of the two using the *Star-CD* commercial software: fig. 2.31 compares the drag coefficients for both the GCM base-line and with baseflaps configurations for the coarser mesh; as can be seen drag coefficient values practically match.

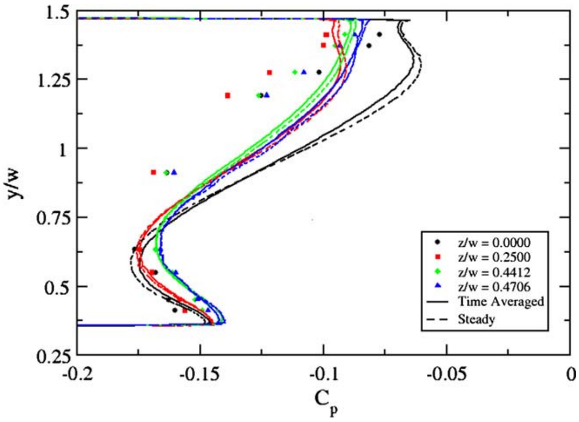

Figure 2.30: Comparison between predicted pressure trends and experimental values in the base region

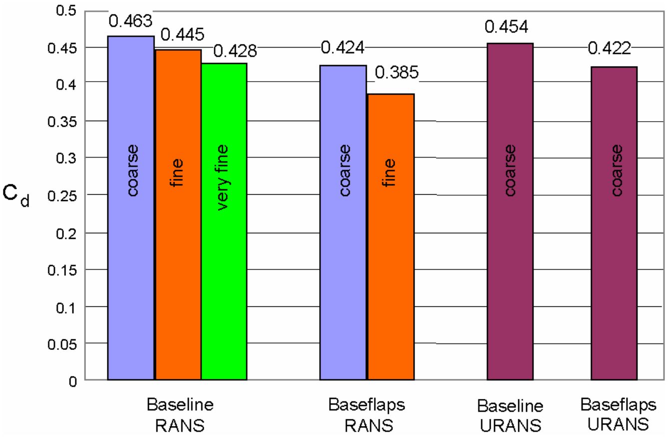

Figure 2.31: RANS vs URANS drag predictions for the coarse mesh

2.2.4 LES simulations of a simplified tractor-trailer system

Purely LES approaches are found to be useful for predicting the flow around bluff-body shapes, nevertheless many limitations exist especially when quantitative information are needed. Such an issue is faced with emphasis in several works by Krajnović and Davidson [23], [57], [58] and [59] dealing with heavy vehicle aerodynamics. Especially in [59], Krajnović and Davidson point out that LES usefulness consists in explaining the physics of such very complex flow, rather than providing accurate predictions on loads and forces on the vehicle. Therefore, the authors speak about the qualitative value of the LES approach as a means to deepen the understanding of the flow features indeed; see for example Krajnović and Davidson [58], where a complete description of the topology of the flow around a simplified vehicle is explained basing on LES predictions, see fig. 2.32 below.

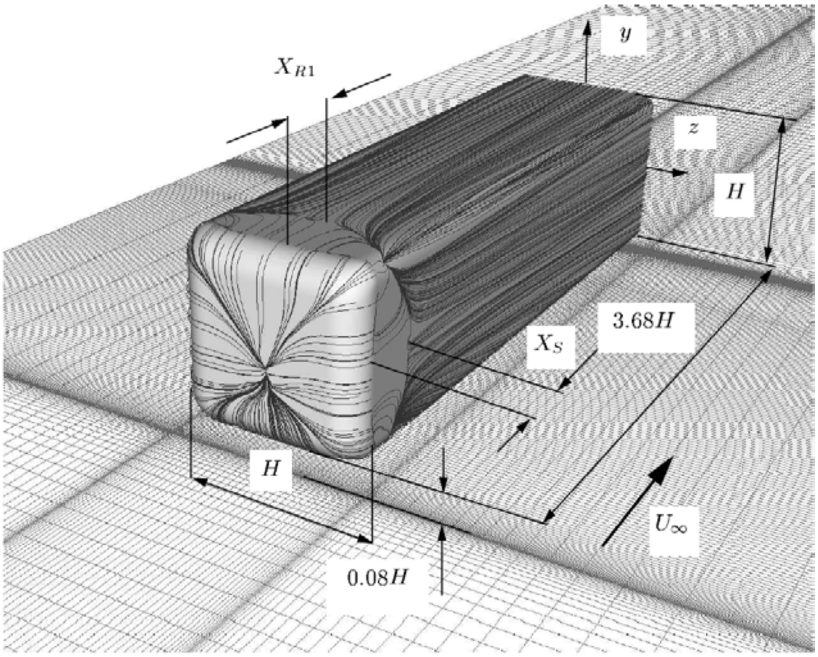

Figure 2.32: The vehicle used by Krajnović and Davidson in their LES simulations

A more realistic vehicle is investigated with LES by Östh [24], basing on the aforementioned articles of Krajnović and Davidson, as fig. 2.33 shows. As can be seen, this vehicle includes the tractor-trailer gap, and accounts for the different heights that the cab and trailer bodies have relative to the ground.

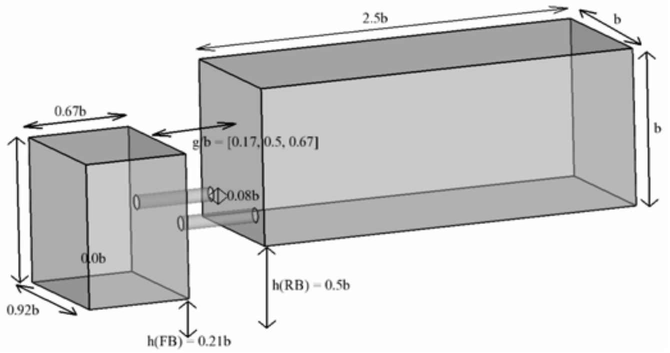

Figure 2.33: The vehicle studied in [24]

This work compares the flows around the vehicle with the front box having both sharp and rounded edges with radius r, with varying the gap g between the tractor and trailer boxes. Comparison with experimental data shows that LES analysis predicts with relative accuracy the drag coefficient only for the model with sharp edges, while for the rounded one, general trends are tracked by LES predictions but with much less accuracy, see Tab. 2.6.

Table 2.6: Predicted drag and errors

g/b	r/b	C_d	Experiment	Error(%)
0.17	0	1.022	1.02	-0.19
0.17	0.08	0.823	0.768	7.16
0.5	0	1.084	1.05	-3.23
0.5	0.08	1.089	1.21	10
0.67	0	1.157	1.09	-6.14
0.67	0.08	1.146	1.28	10.47

Looking at the single drag contributions, fig. 2.33 shows the C_d trends with varying the non-dimensional gap g/b, for the base face of the cab (fig. 2.34(a)) and the front face of the trailer (fig. 2.34(b)).

Anyway, errors in drag predictions for the sharp model from Tab. 2.6 are of the same order of those presented in Tab. 2.6 for the RANS simulations, and for the URANS calculations too by virtue of what proved by fig. 2.31. However, LES is powerful for catching the flow features, and Österh succeeds in explaining the differences in drag coefficients between the two models analyzing streamlines, flow patterns and critical points around the shapes, see for example figs. 2.35 and 2.36. All these results seem to prove further what pointed out on the LES approach by Krajnović and Davidson.

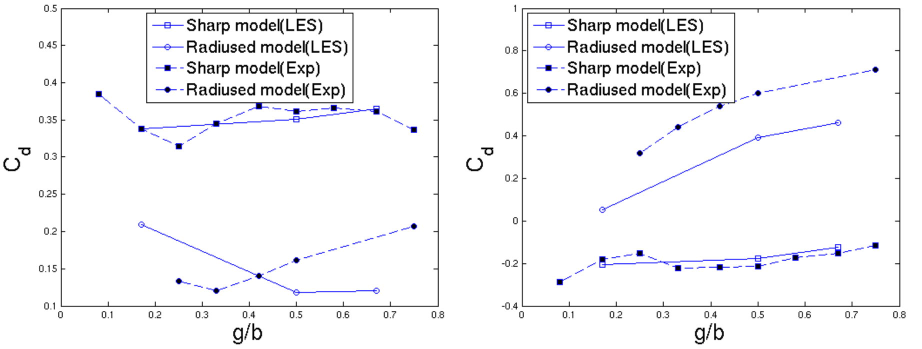

(a) C_d contributions from the base face of the front box

(b) C_d contributions from the front face of the rear box

Figure 2.34: Comparison between predicted and experimental C_d values

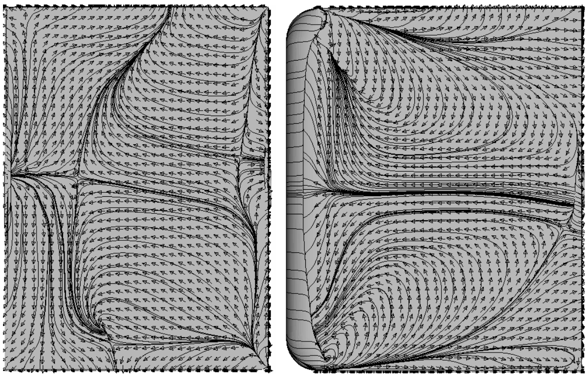

Figure 2.35: Surface projected streamlines on the lateral face of the cab box: with sharp edges (left) and rounded edges (right)

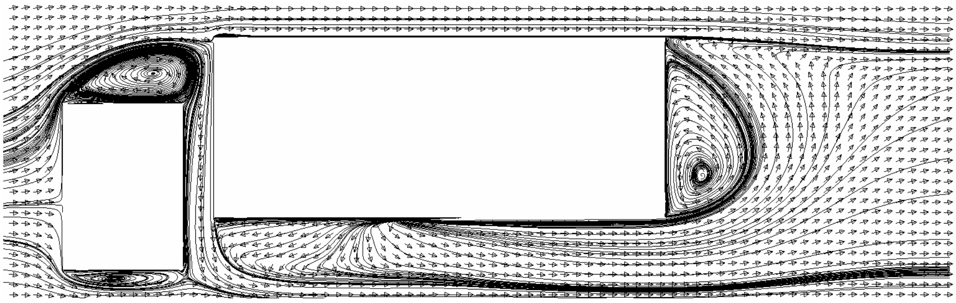

(a) sharp edged model

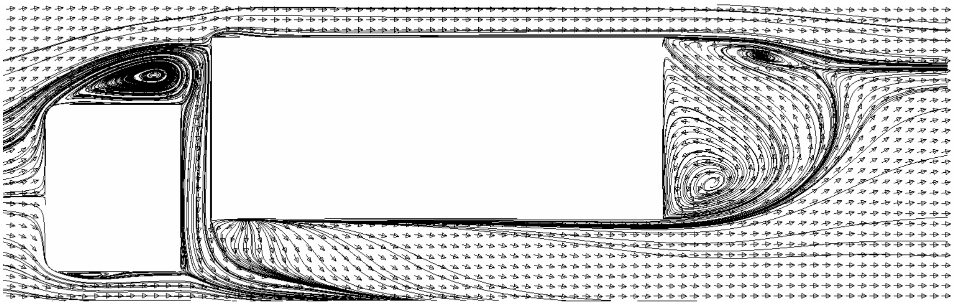

(b) round edged model - r/b=0.08

Figure 2.36: Time averaged streamlines - g/b=0.17

2.2.5 Conclusions about CFD techniques for exploring truck's aerodynamics

Truck's aerodynamics is strongly affected by three-dimensional and time-dependent flow features, due mainly to the vortices formed along both the tractor and trailer edges and surfaces. The flow is so complex, even in the case of very simplified vehicle shapes, that for capturing flow patterns transient processes need to be considered. In general this happens because time-averaged quantities are quite different from the instantaneous ones. Therefore, especially from a quantitative viewpoint, URANS and DES approaches seem to work better than RANS and LES techniques, the latter being very useful in the process of understanding the physics of the flow rather than for predicting quantities with accuracy. Nevertheless, despite the impossibility of predicting such unsteady flows, RANS simulations seem to work well anyway, even if flow features in detached flow regions are physically meaningless. According to such results and as a compromise with the required and overall computational effort, we have choose to solve the fully Navier-Stokes equations with RANS and URANS numerical approaches. RANS will be used to simulate vehicle induced-flows in absence of any obstacle, while the study of the truck-obstacle interaction will be performed with the unsteady version of the RANS approach, or URANS.

Chapter 3

Investigating the Energy Contents: PLANNED ACTIVITIES

In external aerodynamics, the energy contents one could detect into an air flow are obviously in the form of both static and dynamic pressures. But while these forms are strictly related one each other, when an object is moving into a fluid such a relation is not so clear when effects on other bodies placed nearby are of interest. Therefore, use of a *probe* immersed in the fluid domain near the vehicle will help in discovering what is the link, but the course we have planned proceeds with increasing complexity, and activities developed are organized into the following major steps:

- Energy balance analysis
- Numerical analysis
    - flat plate approach
    - RANS modeling with 2D/3D approaches
    - URANS modeling with 2D/3D approaches with obstacle probes

Note that the aim of the present work is to put the basis on the matter and the case of a truck moving with constant speed into a level and windless road is always assumed. Furthermore, bodies to be put into the fluid domain near the moving truck are not permeable to the air, hence in our CFD study steps no actual energy-device is simulated; use of such *obstacles* serves to characterize mainly the resource and to asses the obstacle-truck interaction nature. An investigation of the actual exploiting of the available energy will be presented later.

Furthermore, we have chose to investigate mainly what happens upon the moving vehicle rather than its sides. There are several reasons about such a choice, upon all that of safety for drivers and workers; especially in the case of a turbine-type device, because of the low power-density of wind, rotors of high frontal area would be suggested to be operated, with obvious risks for safety. Furthermore, according to the presence of outside lanes and/or other vehicles moving near the truck it was thought to be more realistic to put some device upon the road, even if maintenance operation are recognized to be more problematic in this case.

Each of the aforementioned step is explained in what follows with emphasis on proposed objectives and pursued methodologies.

3.1 Energy Balance Analysis

A preliminary study is done in order to acquire as much information as possible about the aerodynamic losses that a truck generates during standard operating conditions, starting from the available data on actual literature. Therefore this survey is conducted to make a rough estimate of the global energy balance of an heavy vehicle, aiming at defining the aerodynamic loss structure as well.

As briefly pointed in Sec. 2.2, special efforts in such a field were conducted focusing on fuel savings especially in the USA. The energy consumption due to Class-8 tractor-trailers commercial fleet accounts for the majority of trucking fuel consumption in the USA, and special attention is devoted to such kind of vehicles since 1950's, [60]. Advanced aerodynamics research is ongoing and drag-reduction devices for Class-8 trucks, see Fig. 3.1, are developed with the purpose of increasing energy efficiency, so results are often presented in both terms of drag coefficients and fuel economy parameters.

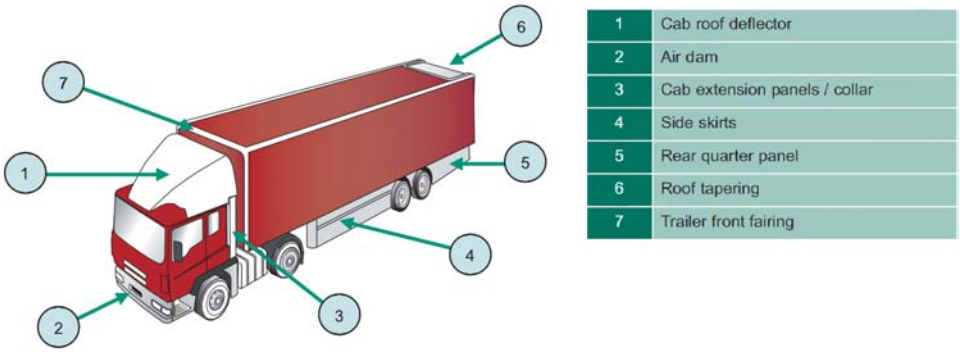

1	Cab roof deflector
2	Air dam
3	Cab extension panels / collar
4	Side skirts
5	Rear quarter panel
6	Roof tapering
7	Trailer front fairing

Figure 3.1: Examples of truck aerodynamic styling

Generally, the drag force experienced by a vehicle moving through a fluid comes from both pressure and friction contributions.

Skin-friction drag arises from the *tangential* shear stresses acting on adjacent fluid layers in the proximity of the body surface, where boundary layers form due to viscosity. The relative movement between the fluid and the body concentrates in this layer and so, for a fixed flow regime, skin-friction drag depends on the surface area over which the fluid flows.

Pressure drag results from the distribution of forces *normal* to the body surface, and several mechanisms may be responsible for the onset of the corresponding pressure differentials. For subsonic flows like those considered here, such pressure fields are due to boundary layer separation.
Whenever a flow has to overcome an obstacle, it impinges on it in such a way that ideally, pressure fields in the front and rear part balance and the drag is due only to skin-friction. Actually, the flow separates from the body surface, and a recirculation flow region forms where pressure lowers. Such a separation may be due to both an adverse pressure gradient or a sharp variation in body shape, as in the rear part of a blunt-shaped body. Therefore, while the pressure in the front of the body behaves almost ideally, somewhere downstream a region exists on the body surface from which the fluid ceases to recover its pressure, and a net force results: the component of this force in the direction of motion is the pressure drag.

Fig. 3.2 highlights the nature of such contributes for the simple shape of a box. The relative contribution of friction and pressure drag depends strongly

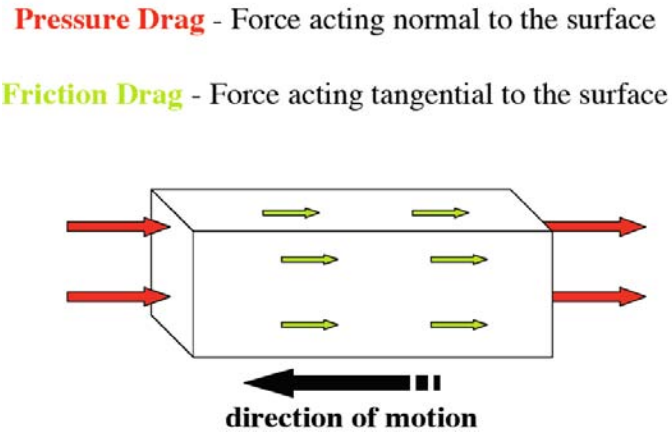

Figure 3.2: Surfaces where drag contributions arise

from vehicle's speed and shape. As an example, consider a 2D streamlined cylinder immersed in an airstream at fixed (and high enough) Reynolds number: the percentage variation of the drag components with varying the thickness ratio is depicted in fig. 3.3: the less is streamlined the cylinder the more is the pressure drag contribution to total drag.

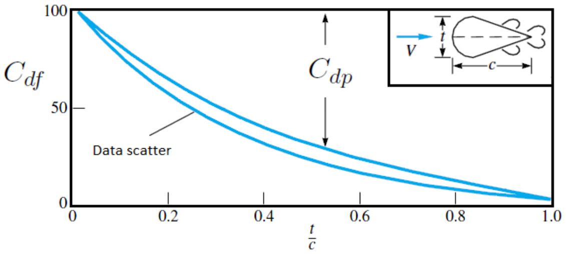

Figure 3.3: Drag data for a streamlined 2D cylinder at Re=10^6, adapted from [25]

As may be expected, a truck behaves like a bluff-body and the total drag is mainly pressure drag, i.e. the skin-friction contribution is very low. As pointed in [61], for a box-shaped vehicle with dimensions of length to width to height of 3:1.33:1 and a skin-friction coefficient of 0.002, the C_{df}/C_d ratio holds only to 2%, corresponding to a value of 5% for a real vehicle. This is why for reducing drag, devices are designed to delay separation as much as possible, or to narrow recirculation regions even at the expense of a higher wetted area. We stress again that results obtained relate mainly to Class-8 tractor-trailer vehicles that resembles quite well the typical COE trucks, hence results are to be considered meaningful for the purpose of this work as well.

3.2 Numerical Analysis

Nowadays Computational Fluid Dynamics tools and packages allow to determine with increasing precision details and very complicated aspects of fluid flows. As shown in Sec. 2.2 a lot of limits still remain relating turbulence modeling, where the power of the computers contributes a lot in determining limits, especially with bluff body modeling; anyway a pure CFD analysis is mandatory, nevertheless a flat plate model is developed first to get basic information about viscous contributions to total drag.

3.2.1 Flat Plate Approach

This activity is a deeper level investigation upon the friction drag contribution to total drag. Expected results will allow to identify the energy content of both the fluxes that the vehicle drags and the ones generated by the displacement of the air as a consequence of the truck transit; the latter ones are those hypothesized to be useful for energy harvesting purposes.

Available experimental data are for the roof of the GTS truck shape presented in Sec. 2.2, hence the flat plate model is set finding the friction drag contribution for both the scaled model and the full-scale vehicle for which results are to be scaled for the speed ranges of interest. Comparison with values of total drag are possible because of the total-drag invariance with Reynolds number, hence specific values for friction-wasted power are presented and clues about the height of the trailed flows presented.

3.2.2 CFD Analysis

With the purpose of investigating the flow field generated by a moving truck with CFD, selection of the best suited numerical approach was crucial. According to results from Sec. 2.2, detailed flow description in the base region of the vehicle was out of interest, hence RANS and URANS methods were chosen as useful tools for performing 2D and 3D simulations. The RANS approach was used for evaluating the flow field upon the truck when no obstacle is placed near the vehicle. Unsteady RANS, or URANS, were used to explore the interaction between the vehicle and the moving obstacle instead. All type of simulations were performed with the vehicle held stationary with the absolute flow field derived subtracting to the velocity field the assumed vehicle speeds, i.e. the imposed flow velocity at the inlet section of the fluid domain. Unsteady simulations were performed in the same way, with the obstacles moving with the vehicle speed.

Numerical 2D and 3D simulations on hybrid grids have been performed using both steady and unsteady approaches with the commercial code ANSYS *Fluent*® v.14.0. The $k - \epsilon$ and $SST\ k - \omega$ models have been selected for the turbulence closure in RANS and URANS simulations respectively. A second-order accurate upwind discretization has been applied in space, while gradients are reconstructed with the Green-Gauss node based approach. The SIMPLE scheme has been used for the pressure-velocity coupling, while time discretization of the first-order implicit type was chosen for the unsteady simulations.

In the present work, and with special emphasis on the European truck type, a new COE truck shape was designed: according to the planned study, neither the complexity of the GCM shape nor the simplicity of the GTS model were considered adequate and a shape in the middle of the two, from an aerodynamic point of view, was developed. See Fig. 3.4 for main dimensions and a general sketch of the European Truck (ET) vehicle. Such as the GTS and GCM models, no interest was put on replicate real undercarriages, mirrors, small scale surface details or flow-through components. Anyway, as the GCM vehicle does, the ET wanted to be more realistic reproducing with more accuracy an actual truck shape, mainly because it accounts for the tractor-trailer gap and exposed wheels, i.e. regions known to affects strongly vehicle drag. All simulations represent the vehicle cruising along a level and windless way, with rotating wheels and reference values of density, pressure and area corresponding to $\rho_r = 1.225\ kg/m^3$, p_r =101325 Pa and $A_r = WH = 9.75\ m^2$.

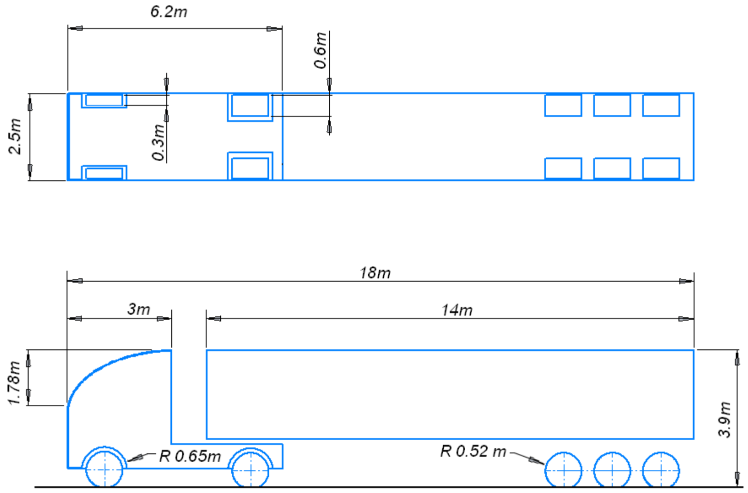

(a) ET main dimensions

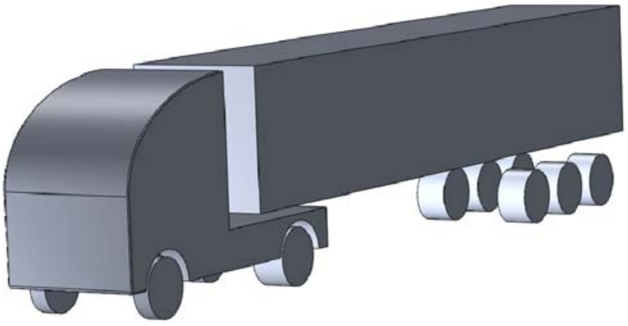

(b) 3D View

Figure 3.4: The ET design

3.2.2.1 RANS modeling with 2D/3D approaches

2D approach

The explored vehicle shapes are two: the first correspond to the central cross section of the ET while the other is chosen to include the wheels, hence coinciding with that showed in Fig. 3.4(a). In the next the former is referred as the No-Wheeled section (NW) while the latter as the Wheeled section (W). Models are analyzed basing on the test-matrix of Tab. 3.1

Table 3.1: Test matrix for 2D RANS analysis

Section	**Vehicles** (#)	**Distance** (m)	**Domain** (H x L) m^2	**Turb. model**	**Speed** (km/h)
W	1 truck	-	100 x 120	$k-\epsilon$	90 ,100 ,110
	2 truck	10	100 x 148		90 ,100 ,110
	3 truck	10, 10	100 x 176		90 ,100 ,110
NW	1 truck	-	100 x 120	$k-\epsilon$	90 ,100 ,110
	2 truck	10	100 x 148		90 ,100 ,110
	3 truck	10, 10	100 x 176		90 ,100 ,110

Column "Vehicles" of Tab. 3.1 give evidence that simulations are performed for the single truck, for two trucks in tandem and for three trucks as well. Trucks are set 10 m apart from each other and speed varied from 90 to 100 and 110 km/h consistent with typical cruising speed ranges. Furthermore, according with values of column "Domain", mesh domains are rectangular and each 100 m height, giving a blockage due to the truck height of 3.9%. The leading truck is positioned 18.5 m apart from the inlet region while the last truck is placed 83.5 m away from the outlet section, whatever the number of trucks and speeds considered.

Note that the selected meshes are chosen according to preliminary tests made upon meshes of lower heights; the 100 m height was chosen because allows the flow to reach the undisturbed value well inside the upper part of the fluid domain. Furthermore, even the incompressible assumption was tested and a compressible simulation was done proving the feasibility of the constant-density approach. Meshes for both the *W* and *NW* shapes are of about 250000, 300000 and 750000 total elements.

Table 3.2: Boundary conditions

		moving	**no slip**	**slip**	**V**	**Pressure**	**TI**	**TLsc**
TRUCK	Wheels	√			√			
	Other		√					
	Inlet				√		√	√
DOMAIN	Outlet					√	√	√
	Sky			√				
	Street	√	√		√			

Tab. 3.2 depicts boundary conditions imposed. At the outlet boundary pressure is set to p_{ref} while turbulent length scale and intensity ($TLsc$ and TI) set to 1 mm and 5% respectively. At the inlet boundary the same turbulent quantities are set to 1 mm and 1% while speeds for both street and wheels are chosen according to velocities of Tab. 3.1. Computational domains are discretized with both structured and unstructured meshes improving solution quality on regions of major concern, such as all the domain parts faced by the trucks and wake regions, see Fig. 3.5(a) where the 3 trucks mesh case is depicted. The upper part of the mesh is structured prescribing an increase in element size to reduce the total number of elements. Comparison between velocity profiles and pressure trends are done focusing on the last truck among the three cases considered; this matching highlighting fluid quantities for each of the three truck position considered for the same outlet conditions, see Fig. 3.5(b).

3D approach

The 3D analysis is performed for a single truck only and for 90, 100 and 110 km/h speed cases. The computational domain has the same dimensions of the corresponding 2D case, with mesh forming a box of 25 m width, with prescribed structured and unstructured regions, see Tab. 3.3 for details. The total number of elements in the mesh is about

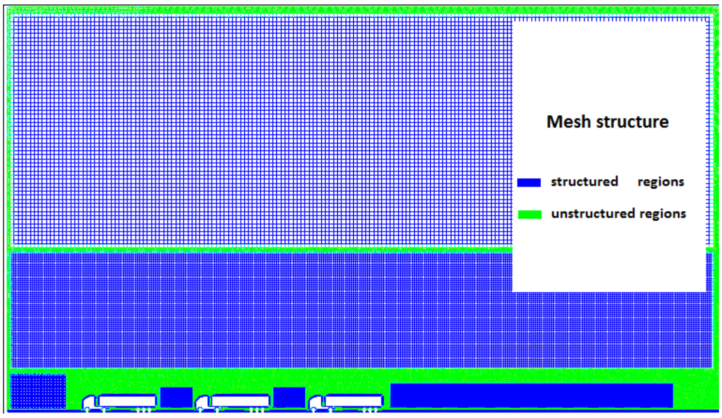

(a) Structured (blue) and unstructured (green) mesh regions

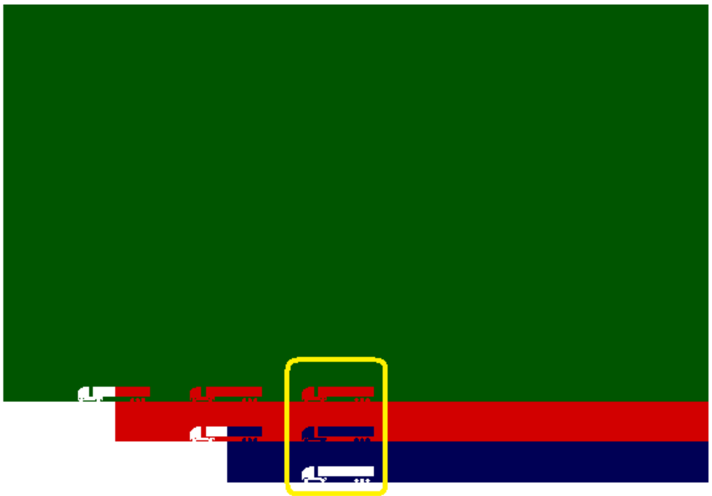

(b) Flow properties are compared for trucks in the yellow box

Figure 3.5: 3 truck mesh case and domain alignment for the 2D analysis and postprocessing phase

6800000. The blockage is defined as the ratio between the frontal area of the ET and the inlet section of the fluid domain, giving a value of 0.39 %, because of the transversal blockage of 10%.

Boundary conditions are imposed as in the 2D case, extending the *Sky* conditions of Tab. 3.2 to both the mesh sides.

Table 3.3: Test case for the 3D RANS simulations

Method	**Domain (H x L x W)** m^3	**Turb. model**	**Speed (km/h)**
RANS	100 x 120 x 25	$k-\epsilon$	90,100,110

3.2.2.2 URANS modeling with 2D/3D approaches with obstacle probes

As briefly pointed out, external unsteady aerodynamics with URANS approaches is proven to work well in the limits discussed above. Conversely, here we faces not only with a time dependent aerodynamic problem, but now the relative motion between a vehicle and an external object has to be simulated with the purpose of exploring the mutual interaction between them. Therefore, a method allowing for reproducing that relative motion has to be selected and validation for the method is then required.

In CFD, *dynamic meshing* is a modeling technique allowing for the arbitrary motion of fluid boundaries into the computational domain. When a time-dependent simulation has to be performed, dynamic meshing allows to simulate the response of the fluid to the prescribed boundary motion at each time-step. In the present work, the obstacle relative motion and its interaction with the vehicle were first explored by means of an obstacle moving relative to the vehicle. 2D and 3D unsteady simulations were planned to simulate such a rigid body motion by use of the remeshing technique available in ANSYS *Fluent*® v.14.0, Inc. [62]. With this method, mesh elements at the obstacle surface and around it were marked for remeshing as user-specified skewness and size limits were exceeded after a prescribed number of time-steps have passed. In doing so, local nodes and cells were added or deleted with varying nodes connectivity.

Validation for the method adopted was done with reference to the test case B of Cali and Covert [18], and the experimental test simulated with considering available data. The vehicle was placed at about 4.5 times the vehicle length from the inlet section. The fluid domain was a box with vehicle/domain dimensions ratios for height, width and length of $h/H = 26$, $w/W = l/L = 10$, while the sampling rate was chosen 10 times higher than the experimental one (i.e. 1000 Hz). The mesh was unstructured with a total number of elements of about 400000.

Results for the validation test are depicted in Fig. 3.6 where CFD and experimental trends for the total force coefficient show good agreement (here positive values means force acting in the direction of motion) while small differences can be ascribed to limited knowledge of the actual test case characteristics. Indication for an adequate selection of the time-steps for the unsteady simulations was derived assuming the Strouhal number ($St = fL_{truck}/U_{truck}$) of the simulations be equal or higher than the experimental one of Cali and Covert [18]. Equating Strouhal numbers gives

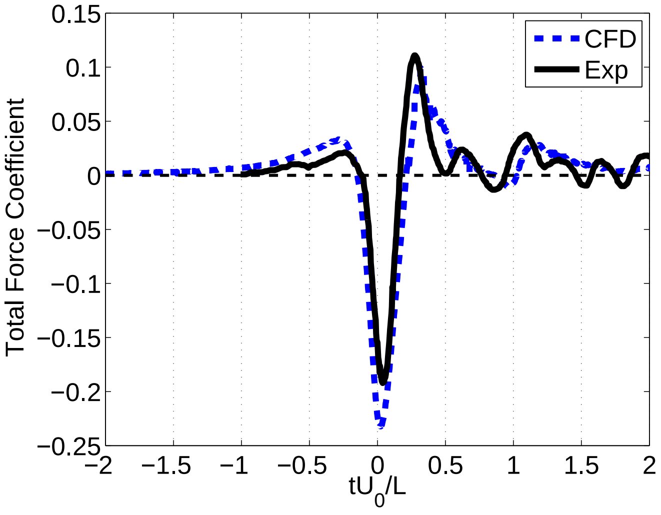

Figure 3.6: Test validation for the dynamic mesh approach

$$f_{cfd} \geq f_{\exp}\frac{T_{\exp}}{T_{cfd}} = 1000\frac{0.063}{0.65} \approx 97\text{Hz} \tag{3.1}$$

where T_{cfd} and T_{exp} are the lapse required by the ET and the vehicle of case B of Cali and Covert [18] to pass underneath the obstacle. In other words, simulations were planned with considering the imposed upper bound for the time-step calculated from Eqn. 3.1 as $1/f_{cfd} \approx 0.01$ s.

2D approach

URANS simulations are performed aiming at characterize the interaction between the vehicle and an obstacle whose lower edge is placed $1m$

above the vehicle roof, this condition being representative of the admitted minimum distance. Variations are monitored for the drag of the truck with varying obstacle shape and dimensions at constant speed, see Tab. 3.4 for details and Fig. 3.7. Therefore, drag variations relate to the additional energy the truck have to waste to maintain its cruise speed, if any. Simulations are performed for the 100 km/h speed case and NW section only, with the domain enlarged to allow the drag reaching the steady value before the obstacle approaches, the mesh having 180 m length. Boundary conditions are the same of the steady case, while a remeshing technique is used to perform the panels movement. The time step is 0.0005 s corresponding to a sampling frequency of 2000 Hz and a spatial-step of about 14 cm. All meshes are of about 200000 total elements.

Table 3.4: Test matrix for the 2D URANS analysis

Type	**Name**	L_p^* **(m)**	H_p **(m)**	**Domain (H x L)** m^2	**Turb. model**	**Speed (km/h)**
Rectangular	P_{n1}	0.4	2.5	100 x 180	SST $k-\omega$	100
	P_{n2}	0.8	2.5	100 x 180		100
	P_{n3}	1.6	2.5	100 x 180		100
Circular	P_{n4}	1.6		100 x 180	SST $k-\omega$	100
	P_{n5}	2		100 x 180		100
	P_{n6}	2.5		100 x 180		100

* or diameter for circular panels

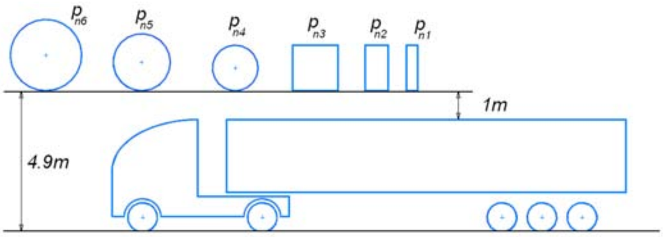

Figure 3.7: General sketch of the 2D unsteady simulations

3D approach

The 3D unsteady simulation is performed for one truck moving at 100 km/h with a cylindrical obstacle of circular shape 1.6 m diameter and 3 m long, see Fig. 3.8. The cylinder axis is placed horizontally across the truck, with the center laying in the $Z = 0$ plane and its lower edge placed $1m$ upon the truck roof (hence resembling in the $Z = const$ planes the arrangement of the 2D circular panels of Fig. 3.7. For this simulation the time step is 0.00179 s corresponding to a sampling rate of about $560Hz$ and a spatial-step of about 5 cm. The total number of elements in the mesh is about 3500000.

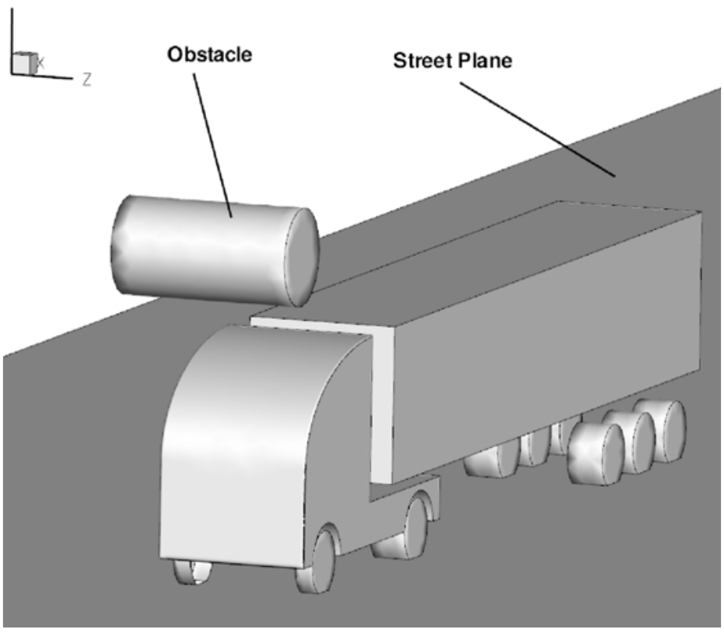

Figure 3.8: The 3D obstacle model

Table 3.5: Test case for the 3D URANS simulations

Method	**Domain** **(H x L x W)** m^3	**Turb.** **model**	**Speed** **(km/h)**
URANS	180 x 120 x 25	SST $k-\omega$	100

Chapter 4

Investigating the Energy Contents: RESULTS

This chapter collects the major results obtained from all the planned activities and starts from the bibliographic research on truck global power wasting and follows with presentation of the main numerical results.

4.1 Energy Balance Analysis Results

For a typical Class-8 tractor-trailer of 300 kW nominal power, Ougburn et al. [26] pointed out that to travel at a speed of 60 mph (approximately 100 km/h) along a level and windless highway, the truck engine has to produce continuously 137 kW at the wheels; according to the percentages quoted, the power being spent to overcome air resistance would be approximately half of that value, see Fig. 4.1.

Basing on such results and according to Hilliard and Springer [61], of the total aerodynamic loss roughly the 5% is spent into frictional losses, i.e. 3.25 kW out of the 65.3 kW of above, the rest of the global loss being used to force the air out of the way. Therefore, air fluxes of a certain strength could be expected somewhere around the truck as a consequence of such wasted power.

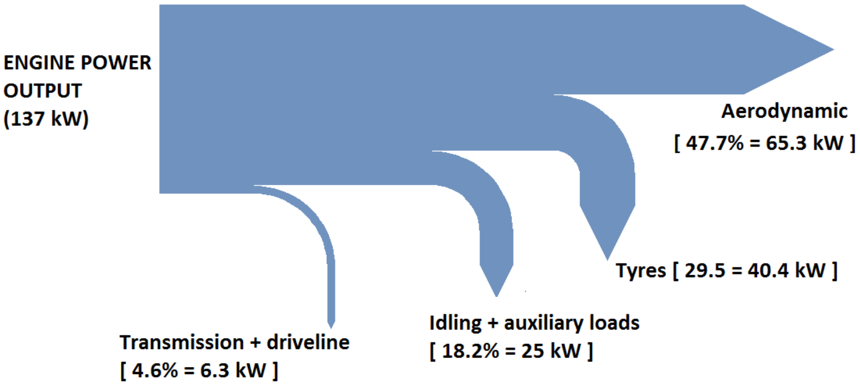

Figure 4.1: Energy consumption percentages from [26]

Another evaluation of the friction contribution to the total drag of a truck could be deduced from the work of Storms et al. [22]. Here is presented the skin-friction curve upon the trailer roof of the 1/8 GTS scaled model, hence by integration we found a viscous drag of about 0.0101, see Tab. 4.1 for more details; here, superscripts r and c stand for $roof$ and *corrected*, the latter being used to indicate the GTS total drag coefficient accounting also for the wheels (+0.1, see Wood and Bauer [63]), the tractor-trailer gap (+0.1, see Wood and Bauer [63]) and the underbody (+0.07, deduced from Diebler and

Smith [64]) contributions; as a matter of fact, the GTS model lacks of such details hence a corrected value is needed to evaluate how much the friction contribute weights on the total. Note that the Reynolds number is based on the scaled GTS width w_m, where subscript m stands for *model*.

Table 4.1: Experimental values for the GTS scaled model

Ref	**Type**	$\mathbf{Re}_m$	C_d	C_d^c	C_{df}^r	$C_{df}^r/C_d(\%)$	$C_{df}^r/{C_d}^c(\%)$
[22]	exp	$2 \cdot 10^6$	0.249	0.519	0.0101	4.06	1.95

From Tab. 4.1 we see that the roof friction contribution to total drag amounts to about 2%, hence total contributes due to viscous effects seems compatible with those predicted further up. Note that values in Tab. 4.1 really relates to a speed test of about 42 km/h, hence values would need to be scaled to typical cruising speeds, but a total viscous contributions higher than 5% is credible anyway as will be showed later.

4.2 Numerical Analysis Results

4.2.1 Flat Plate Approach

Aiming at founding friction-drag values for the full-scale GTS case, we have to extrapolate drag values from Tab. 4.1 because derived from the 1/8 scaled model data. To solve such a problem we remind that dynamic similarity is required and Reynolds numbers have to be the same (we are assuming implicitly the incompressible flow condition). With the symbols used in Tab. 4.1 and considering Reynolds number based on the vehicle width we have:

$$\mathrm{Re}_m = \frac{w_m U_m}{v} = \frac{wU}{v} = \mathrm{Re} \tag{4.1}$$

consequently, the following relation between model and full-scale GTS velocities holds:

$$U_m = 8U \tag{4.2}$$

Tab. 4.2 shows correspondences of Reynolds numbers and speeds between the model and the GTS at full scale:

Table 4.2: Speed correspondences between the GTS model and the GTS at full-scale

Re (millions)	U_m (km/h)	U (km/h)
2	333.6	41.7
3.36	560	70
3.84	640	80
4.32	720	90
4.8	800	100
5.27	880	110

For example, consider now the 100 km/h speed case for the full-scale vehicle; Experimental data at $Re_m = 4.8 \cdot 10^6$ for the model are needed, but from fig. 4.2 from [22], we see that the C_d dependance from Re practically ceases at 10^6, therefore the *total* drag coefficient from Tab. 4.1, i.e. C_d =0.519 holds for the full scale vehicle as well; from this value of C_d and with use of Eq. 2.8 the GTS full-scale aerodynamic load holds to 71.3 KW ($A_r = 10.66\ m^2$ and $\rho_r = 1.2\ kg/m^3$), a value close enough to the 65 KW inferred by Storms et al. [22], as mentioned in Sec. 4.1.

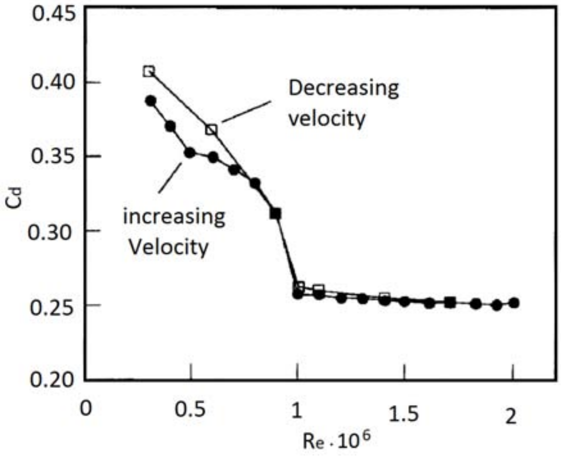

Figure 4.2: Measured total drag

On the contrary, evaluation of the friction-drag at the considered conditions requires to perform the flat plate approach instead.
The value of C_{df}^r from Tab. 4.1 is calculated integrating on the trailer the experimental skin-friction distribution for the GTS model as found by Storms et al. [22], and depicted in fig. 4.3 with red squares (the leading edge of the trailer starts at $x/w_m = 2$), together with its interpolation curve (solid blue) and the theoretical turbulent flat (smooth) plate prediction for the same Reynolds number, that is $Re_m = 2 \cdot 10^6$ (dashed black).
The latter results from the following:

$$c_f = \frac{0.034}{\mathrm{Re}_x^{1/7}} \tag{4.3}$$

where the constant at the numerator of c_f was found equating the experimental value of C_{df}^r at $Re_m = 2 \cdot 10^6$ to the integral of Eq. 4.3 for the same

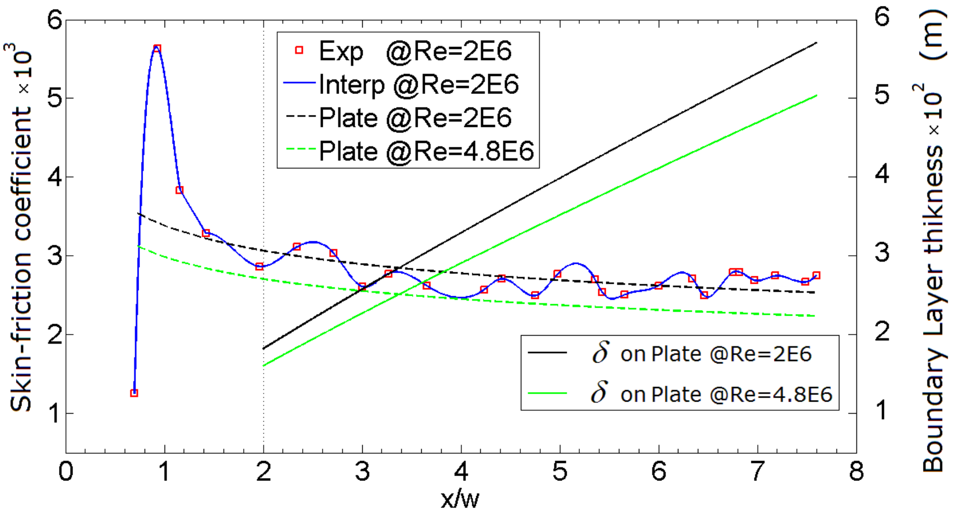

Figure 4.3: Skin-friction and boundary layer thickness distributions for the GTS model at $2 \cdot 10^6$ and $4.8 \cdot 10^6$ Reynolds numbers

Reynolds number:

$$C_{df} = \frac{1}{A_r} \int_{A^r} c_f dA \tag{4.4}$$

Basing on Eq. 4.3 it's now possible to estimate the skin-friction distribution at the needed Reynolds number; see the dashed-green curve in fig. 4.3 and the drag results in Tab. 4.3 for the 100 km/h case.

For this case it is found $C^r_{df} = 8.9 \cdot 10^{-3}$, with a percentage contribution to total drag that is about 12.3% lower than the experimental one.

Table 4.3: Comparison between GTS drag values for the $2 \cdot 10^6$ and $4.8 \cdot 10^6$ Reynolds numbers

Type	**Re**	C_d	C^c_d	C^r_{df}	$C^r_{df}/{C_d}^c(\%)$
exp	$2 \cdot 10^6$	0.249	0.519	0.0101	1.95
flat-plate	$4.8 \cdot 10^6$	0.249	0.519	0.0089	1.72

With the values of the skin-friction coefficient at hand, i.e Eq. 4.3, and assuming for simplicity the power-law suggested by Prandtl, it's possible to calculate the boundary layer thickness on the roof of the GTS model, see [25]:

$$\delta = \frac{\nu}{U_m}\left(\frac{c_f}{0.02}\right)^{-6} = 0.041 \cdot \left(\frac{\nu}{U_m}\right)^{1/7} x^{6/7} \tag{4.5}$$

where ν is the kinematic viscosity of the air at ambient conditions.
Thickness distributions for the model at the $2 \cdot 10^6$ and $4.8 \cdot 10^6$ Reynolds number cases are depicted in fig. 4.3 with black and green solid curves respectively. Finally, equating Reynolds number based on the boundary layer thickness we have:

$$\mathrm{Re}_m = \frac{\delta_m U_m}{\upsilon} = \frac{\delta U}{\upsilon} = \mathrm{Re} \tag{4.6}$$

therefore:

$$\delta = \frac{U_m}{U}\delta_m = 8\delta_m \tag{4.7}$$

With Eq.ns 4.5 and 4.7 at hand we can calculate the boundary layer thicknesses for the full scale vehicle with varying speed; boundary layer heights at the leading edge (L.E.), at the middle (M) and at the trailing edge (T.E.) of the trailer are shown in Tab. 4.4 for this case. Here a little stop is needed, because consideration of the $absolute - flow$ is required, while boundary layer thicknesses relate to the $relative - flow$. When subtracting the truck speed to the relative flow, the thickness δ converts into the distance from the roof where the air is at rest, hence values in Tab. 4.4 relate to the boundary curve separating the viscous region from the inviscid one.
Probably, depending on the vehicle speed, the highest value of the viscous region height is placed before the trailing edge of the trailer, due to the low pressure region at the base that sucks and turn the flow into this area.

Use of Eq. 4.4 and the power expression in Eq. 2.8 allows to calculate Cdf^{τ}s values and both the total aerodynamic and friction contribution loads. Note again that as briefly pointed in Sec. 2.2.1, skin-friction coefficients are made non-dimensional basing on the wetted area, while here we use the truck frontal area for homogeneity with the drag coefficient definition instead. Tab. 4.5 reports the values obtained for the GTS at full scale and

Table 4.4: Height of the viscous region upon the trailer's roof computed from flat-plate theory (GTS at full-scale)

Speed	δ (cm)		
(km/h)	L.E.	M.	T.E.
41.7	14.5	30.8	45.6
70	13.5	28.6	42.4
80	13.2	28	41.6
90	13	27.6	40.9
100	12.8	27.2	40.3
110	12.7	26.8	39.7

ambient conditions along with the relative contributions of viscous and total powers. As can be seen, with increasing speed both contributions become higher while their ratio lowers giving evidence that pressure-drag increase more than friction-drag does, the effect being less evident with increasing speed, i.e. Reynolds number.

Furthermore, because drag coefficients are made non-dimensional using the same dynamic pressure, power ratios equal the drag coefficient ratios, hence due to the invariance of total drag with Reynolds number, the power ratio decrease reflects the lowering of the friction coefficients, as the C^r_{df} column in Tab. 4.5 shows.

Anyway, it is worth noting that these flat-plate predictions assume implicitly that the boundary layer transition locates at the same point of the experimental case; actually, increasing the Reynolds number implies that transition occurs somewhat before, and at the same time, that the boundary layer becomes thinner. For a fixed point on the plate these effects compete, but according to the functional dependance from speed of both the transition point and the thickness (proportional to $1/U$ and $1/U^{1/7}$ respectively), this means that for the range of velocity explored, the advanced transition effect is stronger than the narrowing of the layer. Therefore, except for the $Re_m = 2 \cdot 10^6$ case, boundary layers are expected to be higher than those here predicted, as well as skin-friction values, and then related powers.

Table 4.5: Total and roof-friction wasted powers computed basing on flat-plate theory (GTS at full-scale and ambient conditions)

Speed (km/h)	C_{df}^{r}	P_f^r (KW)	P_{tot} (KW)	P_f^r/P_{tot} (%)
41.7	0.0101	0.1	5.15	1.94
70	0.0094	0.44	24.39	1.8
80	0.0091	0.64	36.42	1.76
90	0.0091	0.91	51.87	1.75
100	0.0089	1.23	71.32	1.72
110	0.0087	1.61	94.18	1.71

Results from this preliminary survey prove again that friction contributes to the aerodynamic loss are quite small; even if these results are restricted to the trailer roof of the vehicle considered, general trends are expected to be the same for the entire viscous contribution, and the upper limit of the 5% of the total loss still remain credible. Now, CFD simulations are required to focus directly into the flow field around the truck, where the prevailing losses are spent to displace the fluid from the vehicle way.

4.2.2 CFD Analysis

4.2.2.1 RANS modeling with 2D/3D approaches

2D Results

Obtained results show that non-dimensional flow velocities and pressure fields allow curves to collapse and to be independent from truck speed U_0. In addition, very little difference arises among the W and NW sections, hence only results for the W-section at the 100 km/h speed case are presented. Comparisons of velocity profiles, see Fig. 4.4, refer to the three axial positions located at the leading edge (LE) and trailing edge (TE) of the trailer roof and its mid-point (MP) with negative values meaning air flowing in the truck direction (the x axis points in the opposite direction of the moving truck in all CFD simulations). Here a point could be seen limiting the trailed flow region upon the trailer roof, where the absolute flow is trailed from the truck, from the one where an opposite airstream seems to be present. This reversed flow is unrealistic and due to the blockage induced by the truck body: velocity profiles were expected to be completely of the trailed type, such those of Fig. 2.3. Nevertheless, results allow some general observations to be made.

For each profile, the Y/H position that corresponds to the $V_x/U_0 = 0$ value can be considered as the height where the trailed region ends; here Y stands for the vertical distance from the street plane while V_x is the absolute velocity component.

As can be observed, the highest value of the trailed region height, reached near the TE, is almost negligible when considering a single truck moving along the lane, being Y/H around 1.1. A different behavior can be observed looking at the last truck of a row of two or three vehicles, being the Y/H value correspondent to the trailed region always equal to or higher than 1.2. In fact, at the LE the Y/H value reaches is about 1.3 for the three truck row, and maintained over this value along all the vehicle. These results indicate that the trailed region growths in height with increasing row length. This fact is best evidenced in Fig. 4.5 where curves depict the loci of the points V_x/U_0

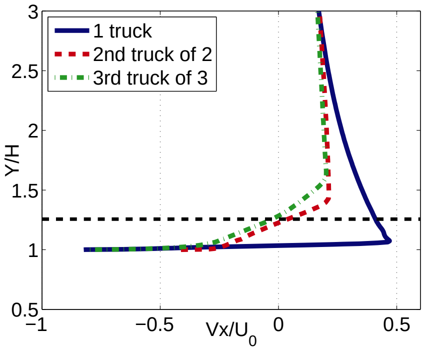

(a) Leading Edge

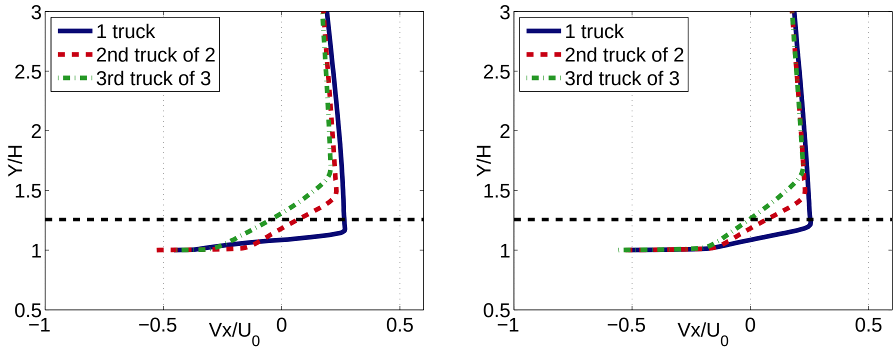

(b) Mid Point

(c) Trailing Edge

Figure 4.4: Non-dimensional velocity profiles for the W-section 100km/h case on the trailer roof

=0 for the three cases considered, now matching the first truck position. Approximating such curves as the boundaries limiting the viscous region, their values give evidence of where the flow could be considered as inviscid. With this approximation, we see that the trailed region growths and expands in the axial direction as well, the wake region rising with the number of trailing trucks. Despite the 2D approximation, results agree with those presented by Baker et al. [65], where the experimental campaign over a train model give evidence of the viscous region growth upon and sideways of the train. At the same time, the wake height decrease just after the last truck is affected by an unrealistic space decay that suggests the avoidance of main three-dimensional effects, as will see later.

In all these figures, the horizontal dashed line represent the 1 m limit distance above the truck (Y/H is about 1.26 here), giving evidence that the trailed flow is always confined into this strip, apart from the 3 trucks case, as Fig. 4.5 shows, in which the trailed region reaches about 1.35 maximum Y/H height.

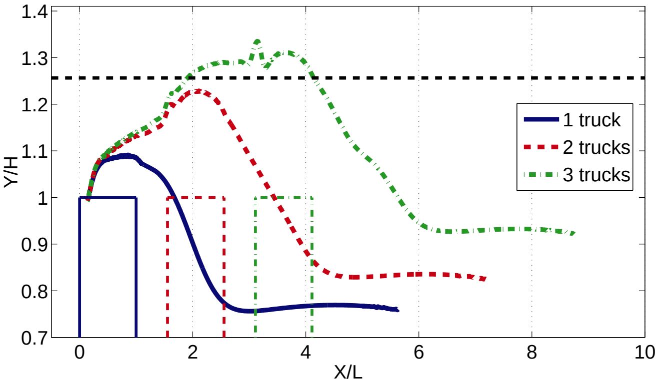

Figure 4.5: Curves representing the Vx=0 loci for the 1 truck, 2 trucks and 3 trucks rows. (rectangular shapes correspond to trucks placement)

Pressure coefficients at $\Delta Y/H = 0.26$ and $\Delta Y/H = 0.64$ distances from the truck surface are depicted in Fig. 4.6. In this figure curves relates to the scheme of Fig. 3.5(b) where the last truck of each row coincides. As can be seen, with varying distance pressure peak amplitudes vary, especially the negative ones, where till 40%-less variations could happen with respect to the $\Delta Y/H = 0.26$ distance case. It's possible to see that the pressure events coincide starting from the base region of each truck ($X/L = 1$) while great differences exist for trailing trucks when compared to the one truck case. In general, trailing trucks enter regions of low pressure generated from the vehicles ahead, the first truck of each row being the pressure *ram* which opens the way allowing trailing trucks to decrease their energy wasting because *surged* from the forwarding vehicles. Comparison of C_p trends for the first truck of each row shows a little increase in the pressure positive peak with augmenting truck number.

Local pressure risings locate at each truck front region where the wake of forwarding vehicles hits the trailing ones, as the local peaks of velocity shows in Fig. 4.4 as well. Note how presented results from Fig. 4.6 reproduce those of Fig. 2.4 where fluid accelerations where calculated starting from the available velocity time-histories; furthermore, experimental results depicted in Fig. 2.7 show the same trend, but the curve is turned over because here are represented the loads that the air applies to the panel, rather than the flow accelerations.

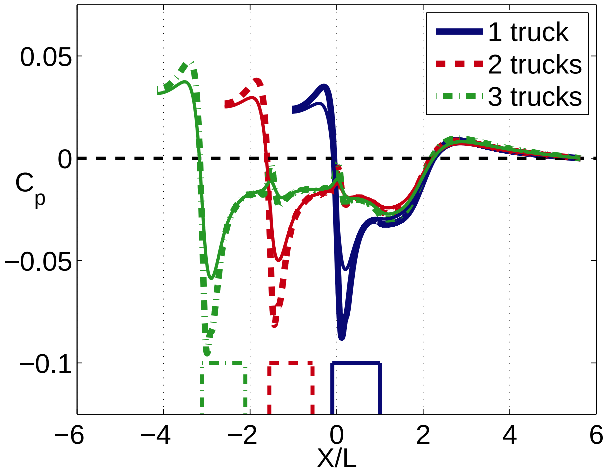

Figure 4.6: Cp trends for the 1 truck, 2 trucks and 3 trucks rows. Thin lines are for the $\Delta Y/H = 0.64$ section, the thick ones for the $\Delta Y/H = 0.26$ section

2D analysis obviously fails in determining correctly the total drag coefficients of the simulated trucks; anyway, with the purpose of detecting the magnitudes of drag contributions, 2D results could be useful to analyze quasi-3D vehicles obtained *extruding* the simulated 2D shapes. For such vehicles we hypothesize that the trailer sides behave in the same way as the roof does, hence the calculated total coefficients are augmented with twice the 2D roof value found. Results for an ideal vehicle without wheels of 2.5 m width based on the NW section are presented first in Tab. 4.6. An ideal vehicle generated from the W-section is of no significance because the presence of the wheels, which extrusion would generate a vehicle with rotating cylinders rather than wheels.

When considering both the W and NW-sections instead, a quasi-3D vehicle could be built stacking both sections with respect of their length contribution in the width direction, with results presented in Tab. 4.7. Note that because the ET is quite different from the GTS model, absolute values of quantities in Tabs. 4.6 and 4.7 differ, while those relating to relative quantities such C_{df}/C_d and P_f^r/P_{tot} are the ones expected to match to some degree those evaluated in our flat-plate approach. For clarity, deviations and differences with flat-plate results are depicted in Tabs. 4.8 and 4.9 for both the two quasi-3D vehicles analyzed. As can be seen, the quasi-3D truck derived from both the simulated truck sections shows the higher matching with flat-plate results, in terms of P_f^r/P_{tot} especially for the 100 km/h case. Furthermore, from the same tables we see that when considering the overall friction contribute to

Table 4.6: Truck drag coefficients and wasted powers based on the NW-section 2D analysis results

Speed (km/h)	C_{dp}	C_{df}	C_{df}^r	C_d	C_{df}/C_d (%)	P_f^r (KW)	P_{tot} (KW)	P_f^r/P_{tot} (%)
90	0.507	0.0318	0.0106	0.539	5.86	0.97	49.27	1.97
100	0.508	0.0314	0.0104	0.539	5.82	1.31	67.74	1.93
110	0.508	0.0302	0.0102	0.538	5.61	1.68	89.30	1.89

Table 4.7: Truck drag coefficients and wasted powers based on both the W and NW sections 2D analysis results

Speed (km/h)	C_{dp}	C_{df}	C^r_{df}	C_d	C_{df}/C_d (%)	P^r_f (KW)	P_{tot} (KW)	P^r_f/P_{tot} (%)
90	0.466	0.0344	0.0087	0.500	6.88	0.79	45.70	1.74
100	0.464	0.0347	0.0086	0.499	6.95	1.08	62.72	1.72
110	0.463	0.0324	0.0078	0.495	6.54	1.29	82.16	1.57

Table 4.8: Deviations of power values relative to flat-plate approaches - truck model based on NW-section

Speed (km/h)	P^r_f (%)	P_{tot} (%)	P^r_f/P_{tot} (%)
90	-6.59	5.01	-12.57
100	-6.50	5.02	-12.21
110	-4.35	5.18	-9.88

Table 4.9: Deviations of power values relative to flat-plate approaches - truck model based on both W and NW sections

Speed (km/h)	P^r_f (%)	P_{tot} (%)	P^r_f/P_{tot} (%)
90	13.18	11.87	0.57
100	12.19	12.06	0
110	19.87	12.76	8.72

drag, is the quasi-3D truck based on the NW-section that seems to agree better on predicted results; in this case, we found percentages varying around 5.8% average against the 5% assumed further up. For the quasi-3D truck based on the NW-section only we found a percentage contribution of the overall friction-drag to total drag of about 6.8% average.

3D Results

Figs. 4.7 show non-dimensional velocity and pressure profiles comparisons between the 2D and 3D one truck case simulations. Comparisons are made for the 100 km/h case with reference to the 2D W shape, with profiles for the 3D model taken from the $Z/W = 0$ section which cut the truck in the middle.

As expected, great influence has limiting the study to a 2D domain, mainly because the air is not allowed to flow around the vehicle. Despite the very high fluid domain realizing a very low blockage value, 2D profiles show very high values of velocity for the reversed flow with respect to the 3D case, as Fig. 4.7(a) shows.

At the same time, comparison for the 2D and 3D Cp pressure trends at $\Delta Y/H = 0.26$ sections of Fig. 4.7(b), proves that the 2D approach affects strongly the pressure field, with pressure values for the 3D case reaching till about 70%-less in relative magnitude. Furthermore, the pressure perturbation generated by the truck in the 3D case is limited in space to about 3 truck lengths against that generated from the 2D model which extends all the domain long. Hence, the bi-dimensional approach exceeds 3D predictions not only in terms of the absolute values of the physical quantities but in the extension of the perturbed regions as well.

When comparing the curves relating to the space point where $V_x/U_0 = 0$, 3D results show that 2D simulations underestimate the trailed region height as depicted in Fig. 4.8(a), where the separation line is taken at the 3D $Z/H = 0$ section . The $V_x/U_0 = 0$ curve appears here increasing in height meaning that the wake expands once the vehicle has passed. To see why look at Fig. 4.8(b) where is depicted a sketch of the flow pattern behind the truck at $x/L = 2$. As can be seen, the two counter-rotating vortices force the flow to point upwards moving higher the boundary of the trailed region, this effect being stronger with moving downwards from the truck region according to the growth in dimensions of the vortices. This flow feature is completely avoided in the 2D simulations therefore the growth in height cannot be catched

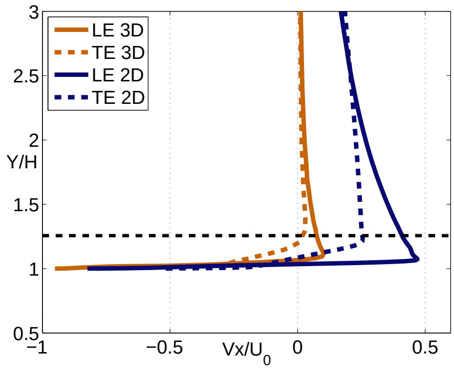

(a) Velocity trends at LE and TE

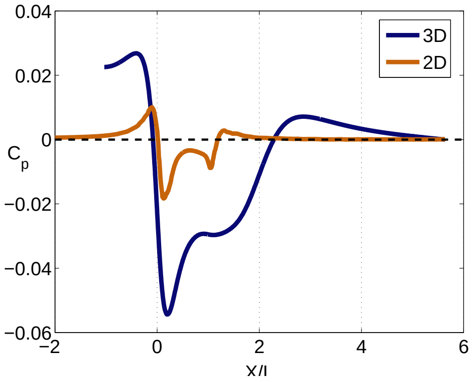

(b) Pressure trends at $\Delta Y/H = 0.26$

Figure 4.7: 2D vs 3D non-dimensional velocity and pressure profiles

correctly, as we have noticed for the results depicted in Fig. 4.5 meaning that a fully 3D approach is mandatory. Variations of velocity and pressure with varying the non-dimensional Z/W-coordinate are depicted in Figs. 4.9 for TE , MP and TE stations for $\Delta Y/H = 0.64$ and $\Delta Y/H = 0.26$ sections above the trailer. As can be seen, transversal gradients decrease with moving to both the side and the base region of the truck for both velocity and pressure quantities. A little increase in the axial velocity component could be appreciated when moving from the MP to the TE points, this effect being related to the nar-

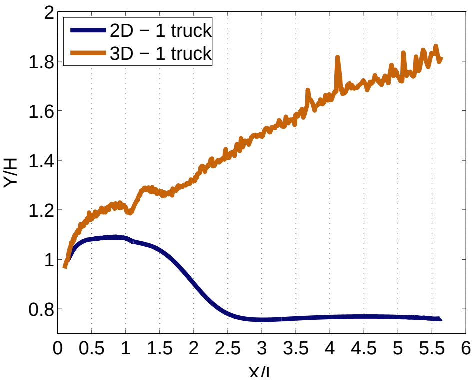

(a) 3D vs 2D trailed flows height comparison

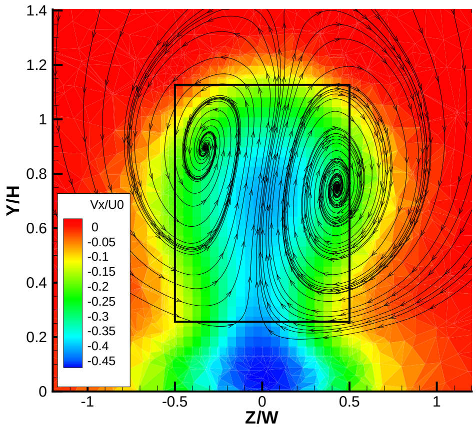

(b) Vortex structure behind the truck

Figure 4.8: 2D vs 3D non-dimensional velocity and pressure profiles

rowing in the axial direction of the streamtubes at the front and rear part of the truck, as Fig. 4.10 shows. Here, background colors refer to the Vx/U_0 magnitudes while streamlines are projected into the plane, giving evidence of the reversed flow as well.

More details of the flow generated by the truck are shown in Fig. 4.11. Here, the reversed flow appears as a characteristic flow pattern that a vehicle generates when moving through still air: the air fronting the

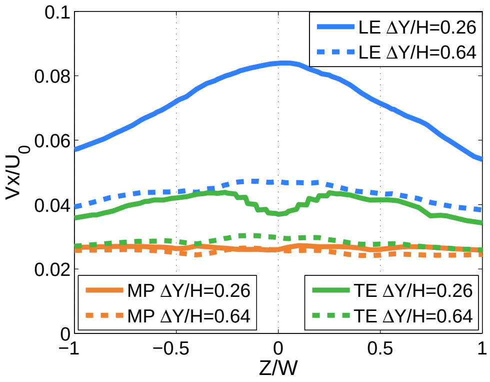

(a) Vx/U_0 velocity trends

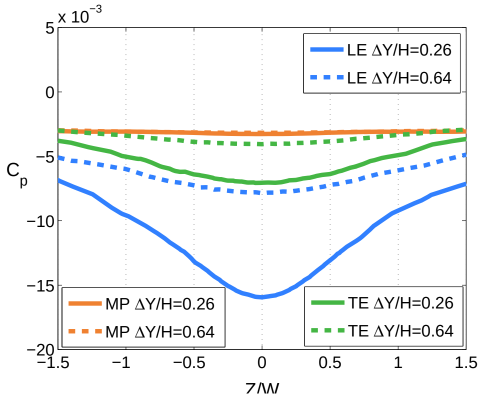

(b) C_p velocity trends

Figure 4.9: $3D$ non-dimensional velocity and pressure dependence from Z/W coordinate

vehicle is forced to flow around the truck body forming a flow moving in the opposite direction of the truck, this effect being essentially of potential nature. Furthermore, when the perturbed airflow reaches the base region of the trailer is forced downward and trailed by the truck itself. A more clear view of the flow structure could be seen in Fig. 4.12 where a 3d sketch of the generated airstream is depicted by virtue of few streamtubes traced around the ET.

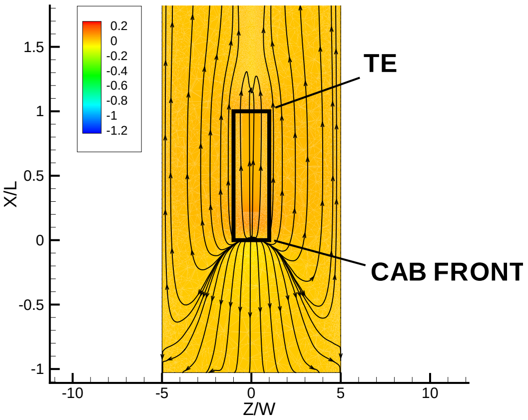

Figure 4.10: $\Delta Y/H = 0.26$ section with projected streamlines. Streamtubes narrow at both the front and base regions of the truck, hence the highest values of V_x/U_0 locate here

Nevertheless, simulated flow values strongly depends on truck blockage, the 3D results being affected from the selected fluid domain dimensions. As Fig. 4.10 shows, compression of the streamlines in the transverse direction increase the reversed flow intensity not only in the sides of the vehicle but even upon it, giving a non-physical contribute to the velocity values of Fig. 4.7(a), where near zero values for Vx/U_0 and only the trailed flow would be expected. Drag values for the 3D model are shown in Tab. 4.10 along with relative deviations from the flat-plate calculations and assumed values for the total drag coefficient. Here, we stress again that vehicles compared are different therefore results are meaningful only in terms of relative quantities. As can be seen, the mismatch in the P_f^r/P_{tot} value is due mainly to the 30% higher value of total drag for the 3D vehicle. That result is not a surprise, the 3D modeling allowing to catch flow features that any 1D or 2D approach cannot reproduce; hence a further proof of the need for a fully 3D modeling is given when very complex flows are of interest. Conversely, total drag sharing between overall-friction and pressure contributes match very well with what expected as a 5.18% value for C_{df}/C_d proves.

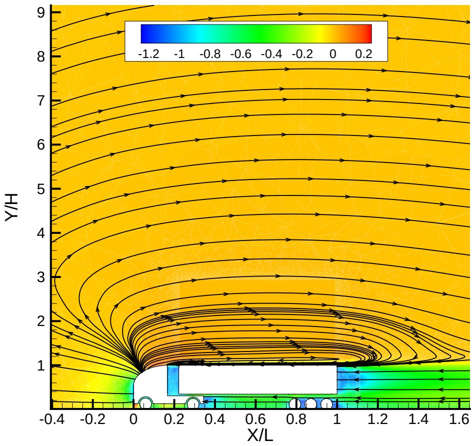

Figure 4.11: Flow pattern and V_x/U_0 magnitude at $Z/W = 0.36$

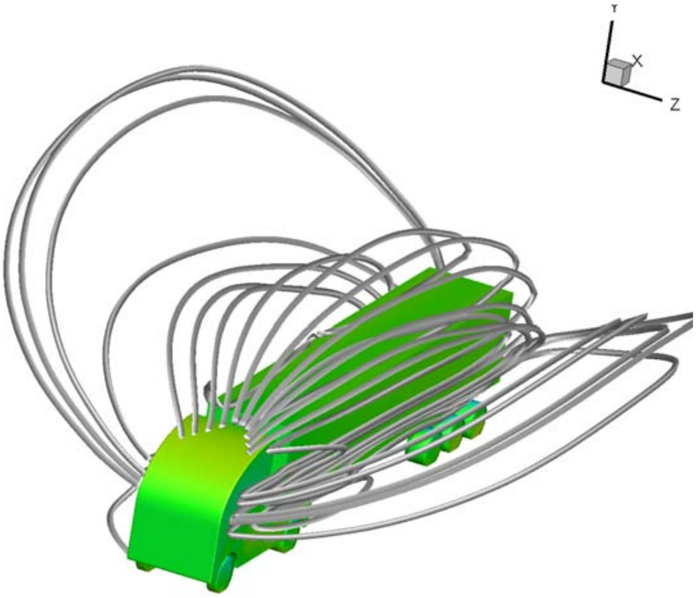

Figure 4.12: The flow structure wrapping the moving truck

Table 4.10: Results for the 3D analysis and comparison with the flat-plate results

Speed (km/h)	C_{dp}	C_{df}	C_{df}^{r}	C_d	C_{df}/C_d (%)	P_f^r (KW)	P_{tot} (KW)	P_f^r/P_{tot} (%)
100	0.629	0.0343	0.0058	0.663	5.17	0.73	83.33	0.88
rel.dev. (%)	-	-	34.8	27.74	-	40.65	-16.8	48.83

4.2.2.2 URANS modeling with 2D/3D approaches with obstacle probes

2D Results

Evaluation of the drag coefficients of the truck with respect to the free panel case are depicted in Fig. 4.13, where C_{d0} refers to the C_d truck coefficient evaluated with no obstacle present (hence that coming from the steady simulations). Fig. 4.13(a) relates to the rectangular panel cases and shows that with varying the axial dimension of the panels (retaining the same height) variations in both amplitude and width of the bell-shape curves towards the front region are induced. With increasing panel width, the air senses the vehicle in advance and the peaks vary in amplitude only, especially that locating at 0 time. In general, drag coefficient deviations get stronger with increasing the panels width, but a little after the cab is passed by.

Fig. 4.13(b) relates to the circular panel cases showing the same trends, panel P_{n6} having the same height of all the rectangular panels, nevertheless showing a positive peak that is around that of P_{n1}, the smallest of the rectangular panel type.
These observations could be explained looking at the energy loss ratio defined as:

$$\frac{E-E_0}{E_{ref}} = \frac{\int\limits_{Domain} (C_d - C_{d0})\, d\tau}{C_{d0}\Delta\tau} \tag{4.8}$$

where the numerator represent the net energy loss addition due to the presence of the panel while E_{ref} represent the energy loss in absence

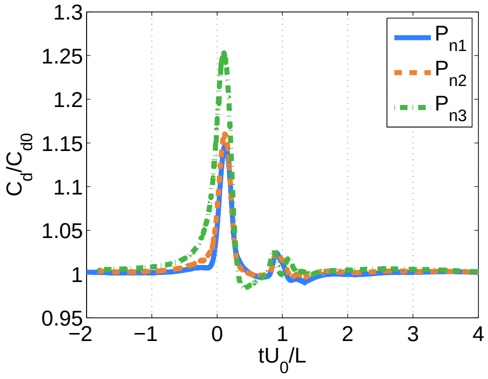

(a) Rectangular panels

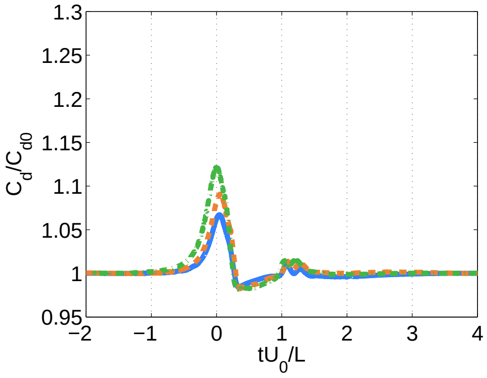

(b) Circular panels

Figure 4.13: Drag coefficients variations due to rectangular and circular shape objects

of any obstacle for a non dimensional time interval $\Delta\tau = 3$, the latter being the chosen reference lapse into which the truck varies its drag. As Tab. 4.11 shows, increasing the width of the rectangular panels and the diameter of the circular obstacle, causes an increase in the truck energy consumption in order to keep the speed constant. Comparison of panel P_{n6} with the rectangular ones proves that despite having the same frontal area, rectangular shapes have the worst blockage effect on the truck, the circular shape being better from an aerodynamica point of view; interpolating obtained results for the rectangular shape for the same L_p/L value of panel P_{n6} shows an energy loss ratio of about 7%, giving more proof of what just pointed out.

Table 4.11: Required energy boost to keep the speed constant

Type	Name	$L_p{}^*/L$	Energy loss ratio (%)
Rectangular	P_{n1}	0.02	+1.42
	P_{n2}	0.04	+1.95
	P_{n3}	0.08	+3.47
Circular	P_{n4}	0.08	+0.37
	P_{n5}	0.1	+1.23
	P_{n6}	0.14	+1.47

* or diameter for circular panels

3D Results

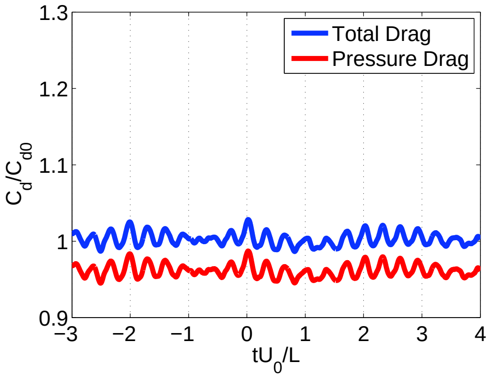

Figure 4.14: 3D total and pressure drag coefficients versus non-dimensional time

Fig. 4.14 shows the total drag coefficient and its pressure contribution time-histories as calculated from the 3D unsteady simulation for the ET moving at 100 km/h. The oscillations in these trends originates from time-dependent flow structures generated by the truck and are recognizable all along the simulated time interval. Variations in total drag because of the transit of the obstacle seems to have the same magnitude of such little variations. Hence, 3D simulations are in contrast to 2D CFD results because now it seems that there is no significant interaction between the ET and the obstacle. Furthermore, from such a simulation we found a little lower contribute of friction to total drag, having C_{df}/C_d a value of 4.12% average against the 5.14% resulted from the steady simulations.

Conversely, Figs. 4.15 shows that the cylinder is affected by the transit of the vehicle. In these figures, *real* curves refer to forces applied to the cylinder as calculated from the unsteady simulation, where the cylinder is represented and allowed to move into the fluid domain; *virtual* trends refer to the same quantities evaluated for a virtual surface generated in the steady CFD solution where no cylinder was simulated. This virtual surface has the same dimensions and kinematic of the cylinder considered, hence computed loads comes only from the unsteady static pressure field generated by the moving truck. $difference$ curves result from the mathematical subtraction of the virtual values from the real ones, assumed to give evidence to the force contribution generated only by the presence of the obstacle near the truck altering the flow. The goodness of such an approach comes from the potential nature of the flow, especially because upstream and nose regions have proved to behave in this way, the true flow supposed to be close enough to the superposition of the virtual and the perturbed flows. In Figs. 4.15 are presented both the horizontal and vertical force contributions (respectively in the x and y direction) acting on the cylinder, non-dimensional coefficients based on the cylinder frontal area and truck speed. As can be seen, the strongest loads are near the 0 time, i.e. near the nose vehicle region where the vertical force shows an inversion of its direction in a very little time.

From Figs. 4.15 we see another interesting feature: the wake region where the cylinder moves within in both real and virtual simulations do not give significant contribution to lift while drag is affected in terms of only the perturbed flow. This means that the wake is mainly a unform pressure region as expected, and the non-zero drag of Fig. 4.15(a) is a purely trailed flow effect.

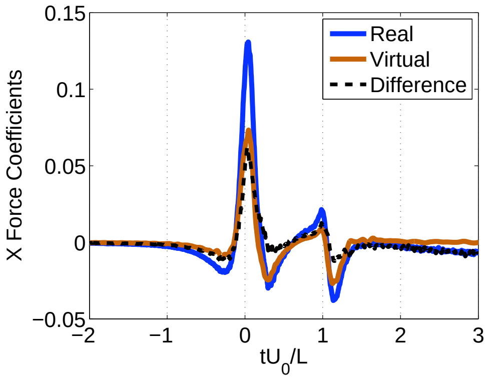

(a) Drag histories

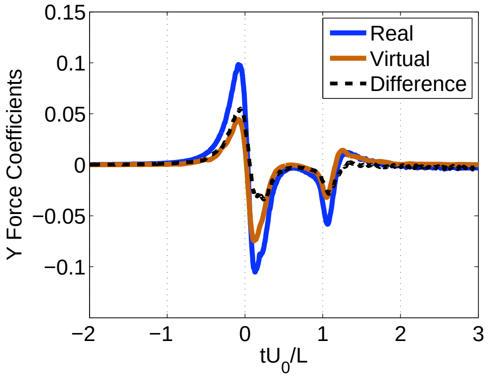

(b) Lift histories

Figure 4.15: Drag and lift time histories for drag and lift coefficients

According to the force coefficients loading the cylinder, Fig. 4.16 shows how the flows considered affect total forces directions with varying time. Composition of both the x and y force coefficients allow to identify angles for both the flows resulting from the 3D unsteady simulation and that related to the perturbed flow generated by the cylinder. As can be seen differences are located mainly in the third quarter of the transit interval, but in general directions agree.

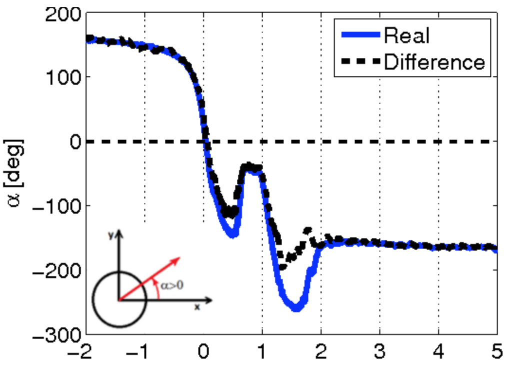

Figure 4.16: Angle variation with time for total forces acting on the cylinder

Trends for the resulting total forces and coefficients are presented in Fig. 4.17 for all the flows considered. As can be seen, the first peak locates at 0 time and is roughly twice the second one, which places at the end of the transit interval. In other words, these results prove that the main loads induced by the truck on the cylinder locate in the nose and base regions of the truck. Furthermore, comparing coefficients in Fig. 4.17 shows that real values are 1.5 and 2 times higher than the virtual and difference values respectively.

It is now possible to identify approximately the velocity values that a uniform flow would has in order to realize the same loads as those generated by the perturbed flow. From Shlichting [66], we see that the C_d value for a smooth cylinder presents a plateau for Reynolds numbers ranging from about 10^4 to $2 \cdot 10^6$, this value being about 1. For the case considered here, this Reynolds number interval corresponds to a flow velocity interval ranging from about 0.003 to 1.04 of V_x/U_0, where CFD results show that velocities upon the truck fall, see Fig. 4.11. Using this value for the drag coefficient and solving its definition with respect to the velocity term, the force coefficient history of Fig. 4.17 for the perturbed flow allows to plot the non-dimensional *equivalent flow velocity* time history of Fig. 4.18. The obtained velocity curve reflects peaks location of the load history, furthermore it acts with directions that coincides with those depicted in

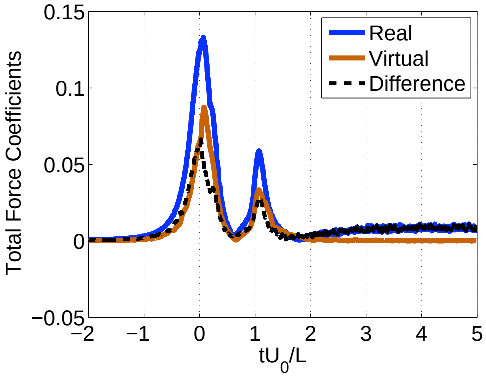

Figure 4.17: Absolute values of total forces acting on the cylinder

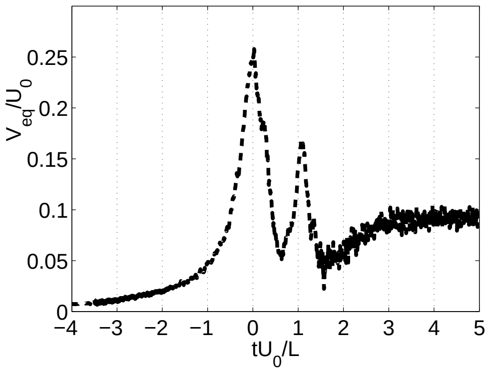

Figure 4.18: Non-dimensional equivalent flow velocity

Fig. 4.16, proving that the flow rounds clockwise the cylinder during the transit interval, the higher values of velocity being in the opposite direction of the truck motion. A sketch of the flow as seen by the cylinder is presented in Fig. 4.19 for a non-dimensional time of about 0.14, for the $Z = 0$ field section. As can be seen, streamlines seems to not be so altered by the obstacle presence, the latter allowing to extend the accelerated flow region from the cab surface to the space between the cylinder and the roof.

Note now that the equivalent velocity is based upon both x an y load contributions, hence v_{eq} accounts for both the velocity components in the $x - y$

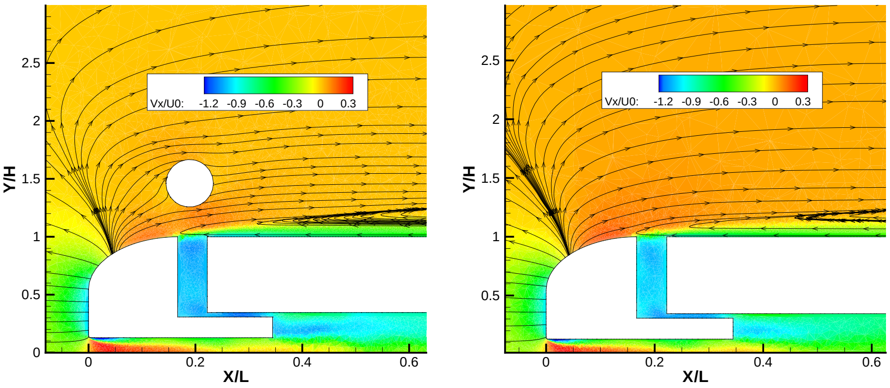

(a) Unsteady flow at about tU_0/L=0.14 (b) Steady flow

Figure 4.19: 3D streamlines comparison at $Z = 0$ sections

plane; when considering velocity profiles the vertical component of velocity upon the trailer was not considered before, only in the nose region we found that such components contribute strongly to the overall velocity, as Figs. 4.19 show.

The equivalent velocity concept bases its validity in that the actual flow on the obstacle is truly uniform even if highly time dependent, as proved when observing the instantaneous total pressure field upon the obstacle, see Fig. 4.20; here the cylinder is represented unwrapped with angles as those of Fig. 4.16. As can be seen the pressure distribution practically do not depends from the transversal coordinate, and the same happens for the $difference$ load contribution from which the equivalent velocity is derived. Note also that Fig. 4.16 depicts only the pressure field at U_0t/L=0.15, but the same uniformity holds all along the vehicle transit interval.

Furthermore, such a uniformity holds in a core of the flow located just upon the truck, as for example Fig. 4.12 schematically shows. When higher positions or larger cylinders were considered, a less unform flow would be expected because of the spherical-like shape of the induced flow.

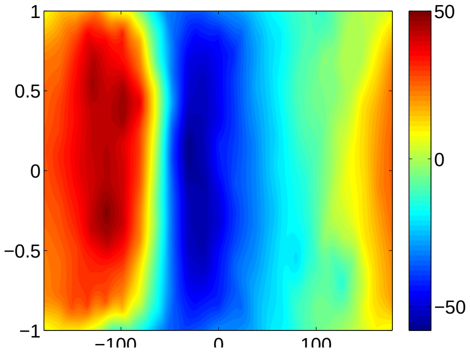

Figure 4.20: The pressure field on the simulated obstacle at U_0t/L=0.15; pressure units in Pa

4.3 Comments on the Obtained Results

Our results have proven that investigating the energy contents carried by the airflows induced by a moving vehicle is truly a challenge and this section is devoted to commenting obtained results from the point of view of the energy harvesting process.

The aerodynamic loss that a truck requires to move is due mainly to its streamlining because it behaves as a bluff-body. In fact, from Tab. 4.12, we see that when considering different approaches, and for a truck moving at 100 km/h, the order of magnitude of the frictional contribution to total drag is little and the value of 7% is never exceeded; a percentage around 5% is considered more credible.

According to percentages in Tab. 4.12, we see that in the case of the 3D RANS case performed the pressure-drag contribution holds to about 79 kW; hence, when the truck is moving such power serves mainly to displace the air out of the way; the air is pushed in the front part of the vehicle while it is surged by the truck base region and a flow structure resembling that generated by a source-sink couple appears, see for example Fig. 4.12 for a sketch of the resulting flow pattern. Starting from this observation, one could expect that exists a moving flow field whose energetic potential lyes in both the generated flow and in the fact that it is moving with the truck, i.e. what we are termed here $absolute-flow$. From this point of view we found a confirmation of the general results presented in Chap. 2, where analysis of the experimental tests proved the existence of an inviscid region where the flow could be approximated as a potential-flow. Here, such region was located in the front part of the moving vehicle, but when placed high enough from the

Table 4.12: Results obtained for the 100 km/h speed case

Approach	C_{dp}	C_{df}	C_{df}^r	C_d	C_{df}/C_d	P_f^r (%)	P_{tot} (KW)	P_f^r/P_{tot} (%)
1D	-	-	0.0089	0.519	-	1.72	71.32	1.72
quasi-3D (NW)	0.508	0.0314	0.0104	0.539	5.82	1.31	67.74	1.93
quasi-3D (W+NW)	0.464	0.0347	0.0086	0.499	6.95	1.08	62.72	1.72
3D	0.629	0.0343	0.0058	0.663	5.17	0.73	83.33	0.88

truck the inviscid region is expected all along the vehicle. Therefore, when considering an hypothetical harvesting process, this is the region where one has to focus because no direct interaction arise due to presence of immersed surfaces into the high velocity gradient subregion. According to the 2D approximation, see Fig. 4.5, we have proven that when one vehicle is considered the viscous subregion seems to be confined well inside a strip of about 1 m height upon the truck, following vehicles contributing in put higher such a boundary. But results from the 2D unsteady simulations showed that the truck is affected by the presence of the obstacle, see Tab. 4.11 for a resume about the energy boost required by the truck to keep the velocity constant with varying the obstacle shape. This fact is due to the strong reversed flow that extends a lot upon the limiting curves of Fig. 4.5.

According to 3D results, see Fig. 4.7, we have proven that when a full modeling is allowed, the flow field loses in strength and the 1 m limit upon the vehicle remains a credible limit upon which the inviscid region exists, for one vehicle at least. In this case, the reversed flow still appears but is so little that on one side proves the limits of the 2D approach and on the other side calls for a fully 3D unsteady simulation.

From Fig. 4.14 we see that for one truck the presence of the obstacle do not interfere significantly with the vehicle motion, hence a possibility arises about the feasibility of putting an harvesting device upon the truck, at least 1 m height above it. In fact, results for the single truck case prove that any interaction, if any, has the same order of magnitude of the variations in total drag experienced by the vehicle. Note also, that when a not permeable device is immersed into the fluid domain, one probably faces with the worst case scenario in terms of interaction with the advancing vehicle; it is expected that when some device, i.e. a turbine, is placed upon the vehicle, the interaction lowers because it allows some air to flow through the rotor rather than be completely deviated by an obstacle such that used here. This is obviously an issue that requires further study. Therefore, according to the single truck results, it seems to be possible satisfying the harvesting process paradigm, i.e. the harvesting process is feasible without forcing the vehicle to waste more energy than that required by its motion when no device is placed nearby; hence, from now on we have some confidence in speaking about a real resource.

When investigating the loads acting on the obstacle we see that forces of a certain strength exist, even if they are generated by two different mechanisms. When the loads acting on the obstacle are studied by means of a virtual probe moving nearby the ET, a very strong resemblance and time matching is found with the loads experienced by the actual cylinder, see Figs. 4.15. Therefore a contribution to the total loads is due to the flow perturbation that the obstacle induces near the moving truck. According to the inviscid character of the flow in the region explored, such a contribution could be evidenced by subtraction of the virtual loads from the total ones. Hence we argue that the total load is due to both the moving pressure field and the moving velocity field. The former arises because of the pressure field generated by the truck while the latter is entirely associated with the presence of the obstacle itself. This is the reason why a limit exists in considering only the potential effects due to the moving vehicle: the flow that impinges on an external body arises only when the body is physically immersed in the moving field. These are found to be the two mechanisms acting on the cylinder and hence the two forms available for exploiting energy from the moving flow field without affecting the truck motion.

When vehicles induced-winds are of interest a very practical tool such as the $equivalent - velocity$ concept is thought to be useful. Once defined, the velocity pulse of Fig. 4.18 allows to see that when a truck moves a ramp is generated consisting in three main part: the first, where starting from rest the air feels a smooth increase in velocity; the second, where two high velocity peaks are found and the third consisting in the wake region decaying with a very slow time rate, see Fig. 2.5. Furthermore, apart the time scales involved, with making v_{eq} dimensional, we found peaks of about 7 m/s and a wake-effect velocity of about 2.5 m/s respectively, hence the dynamic content of the field is quite poor, at least when compared to typical speed at which turbines work.

The feasibility of positioning a wind turbine device is explored in the next chapter.

Chapter 5

Exploiting the Wind Energy Content: the Start-up Problem

In the introductory section of the present work we have briefly showed that many of the patents and ideas relating the harvesting process applied to vehicle-induced flows were based on drag-type vertical axis rotors. There was suggested that use of such rotors was realized probably because of both the highly variable flow direction and the need for allowing rotors to start without use of any servo-motor. In the present chapter we analyze both such intuitions and propose an approximated approach to evaluate the start-up capabilities of a drag-type vertical axis wind rotor when subjected to the flow induced by one truck. After that, an extension to the case of a truck row will be analyzed for evaluating the harvestable energy potential and put light onto the real feasibility of such a technology.

5.1 Drag-Type Wind Rotors

As already focused in Sec. 4.2.2.2, our integral approach let us to introduce an equivalent uniform flow allowing to characterize the induced-flow upon an heavy vehicle when moving in a level and windless highway for typical cruising speeds. In particular, we have seen that this flow changes its direction during the transit of the vehicle, as the *difference* curve of Fig. 4.16 shows; from this figure we have seen that the induced flow rotates clockwise pointing initially in the same direction in which the truck moves and completing a full round around the obstacle during the truck passage.
Therefore, when thinking about some wind generator to be placed near the moving vehicle to exploit such a flow, the VAWT (Vertical Axis Wind Turbine) rotor is the natural choice because it is well known that it operates regardless of wind direction. This evidence confirms that use of a VAWT is the right choice when aiming at harvesting the energy content in vehicle induced flows.

Usually, when dealing with VAWTs, one may think about both lift or drag-types rotors, which mainly reduce to Savonius and Darrieus turbines, see Fig. 5.1 for an example of such a devices. As well known, drag-type rotors are capable of producing a useful torque mainly because of the resistance opposed to the free flow by the moving blades. As shown in Fig. 5.2(a) for the Savonius rotor, the working principle relies in the lower drag force experienced by the advancing blade with respect to the returning one, gen-

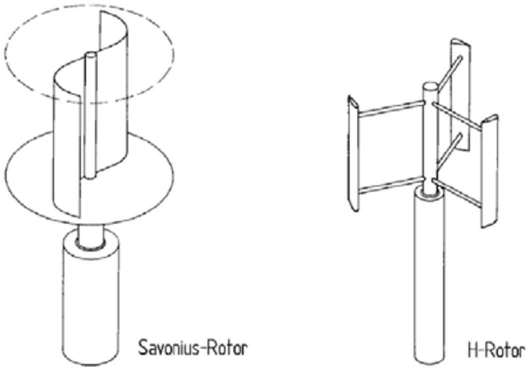

Figure 5.1: Drag and lift type rotors

erating the positive net torque to be harvested.
In lift-type rotors the net useful torque comes from the aerodynamic lift generated by the rotating airfoils; each blade operates with a time varying angle of attack generating aerodynamic forces continuously varying in both magnitude and direction, as Fig. 5.2(b) shows.

The difference in working principles between these rotors give the reason why their performances and optimal regimes are so different. To show this look at Fig. 5.3 where is a sketch representing the power characteristics of several wind rotors in terms of their *power coefficient* C_{PR} and the *Tip speed ratio*, λ or TSR, defined as:

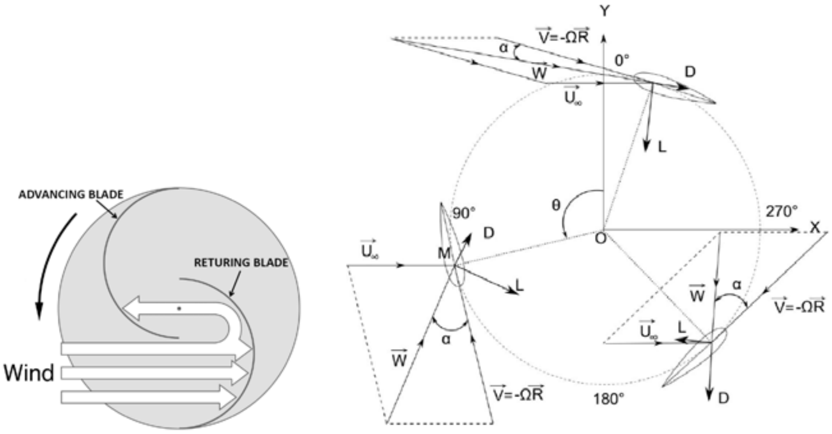

(a) Savonius rotor (b) Darrieus rotor

Figure 5.2: Working principles of drag and lift type wind rotors

$$C_{PR} = \frac{P_R}{0.5\rho V_0^3 A_R} \tag{5.1}$$

$$\lambda = \frac{\omega R}{V_0} \tag{5.2}$$

$$C_{QR} = \frac{C_{PR}}{\lambda} = \frac{M_{mR}}{{}^1\!/\!_2\rho V_0^2 A_R R} \tag{5.3}$$

where P_R is the net delivered power, V_0 the wind speed, R, A_R and ω are the rotor radius, swept area and angular velocity respectively and M_{mR} the aerodynamic torque; Eq. 5.3 refers to the *torque coefficient* whose expression in terms of the power coefficient will be useful in the following. Basing on the same wind speed for the sake of simplicity, from Fig. 5.3 we see that

Darrieus rotors operate at higher angular velocities than Savonius rotors, and the maximum power delivered from the latter is less of half that of the Darrieus rotor. This difference in regimes, or tip speed ratios, comes directly from the fact that blades operating in a drag mode cannot exceed the wind speed; conversely, only lift types rotors can exceed the TSR limit of 1. This is why in Fig. 5.3 one can see that Savonius rotors have an upper limit in TSR slightly beyond unity: in fact, it is known that such rotors can produce a little amount of lift according to their poor airfoil-like behaviour. The superior efficiency of lift type machines comes mainly from the fact that the useful force, the lift, is due by the pressure gradient established across the profile surfaces, rather than the deflection in the momentum imparted to the flow by the blades of a drag driven device.

Nevertheless, from technical literature it is known that the start-up behaviour of lift-type Darrieus turbines is very sensitive to rotor position, see for example the works of Bianchini et al. [67] and R. Dominy and Dominy [68], furthermore they present a low torque when starting from rest; to prove that claim, we differentiate now Eq. 5.3 with respect to λ, and considering

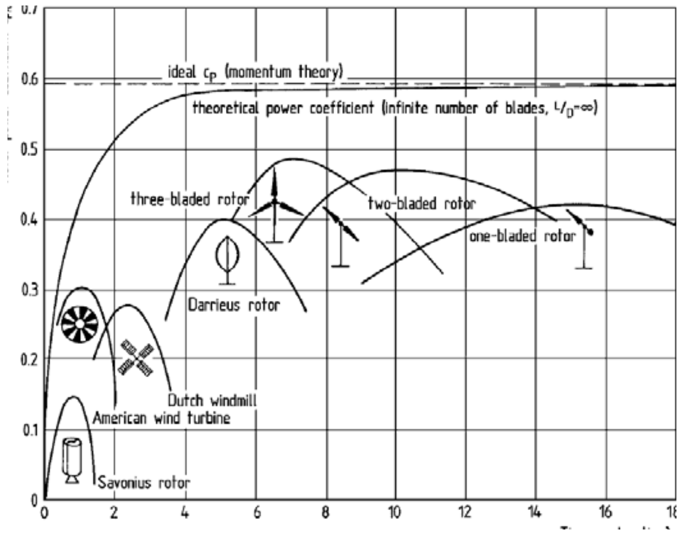

Figure 5.3: Wind turbines power coefficients, from [27]

value at zero TSR we found:

$$\left.\frac{dC_{PR}}{d\lambda}\right|_0 = C_{QR}(0) \tag{5.4}$$

This means that when a wind rotor is at rest, its starting torque value coincides with the slope of the power curve there. Consider now Fig. 5.4(a) and Fig. 5.4(b) where typical Savonius and Darrieus turbines power curves are depicted: as can be seen and according to Eq. 5.4 Darrieus rotors have always less starting capabilities than Savonius rotors because of their flat characteristic curve at the lower values of TSR.

Therefore, especially when low wind speeds are of concern drag-type rotors

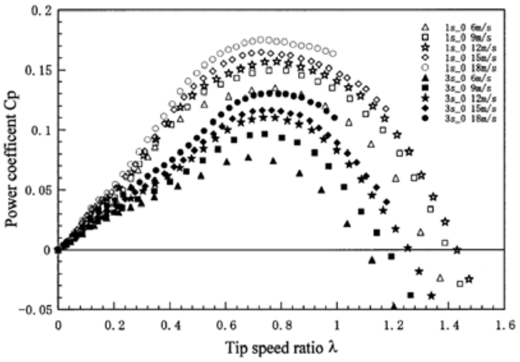

(a) 1-stage (1s) and 3-stage (3s) Savonius characteristic curves, from [69]

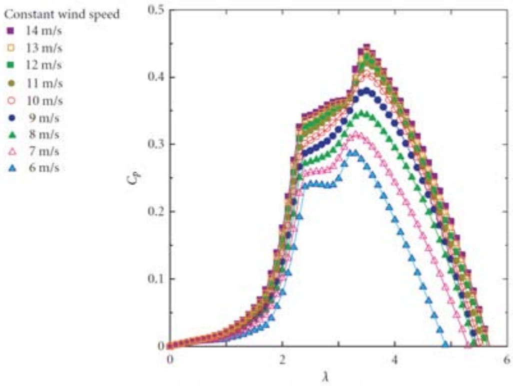

(b) 4 blades Darrieus turbine characteristic curves, from [70]

Figure 5.4: *Cp* curves for Savonius and Darrieus wind rotors

are in general preferable than lift-type rotors according to their higher starting torque. Moreover, if the resource consists in a very impulsive wind-load, as those generated by a moving vehicle, a high-starting capability rotor is preferred and Savonius turbines are to be considered superior than Darrieus machines for the special application considered here.

The explanations given above supports the main idea of using Savonius rotors for harvesting vehicles induced-winds, as shew by most of the patents presented in Sec. 1.

5.2 Start-up Dynamics of a Savonius Rotor

Generally, once the choice of the adequate wind-rotor type is made, one has to face with the testing of such a turbine with the wind-load at disposal. When numerical simulations are of concern, models aiming at reproducing the dynamics of the turbine require knowledge of its power curves with varying wind speed, see for example Bianchini et al. [67]; the turbine power curves depend from the wind speed as shown in Figs. 5.4, despite the non-dimensional representation of power in terms of C_p. Hence, with a variable wind speed, the operating point of the turbine moves among the different power curves according to the inertial characteristics of the machine, see Yutaka et al. [70]. Obviously this fact makes the dynamic study of the turbine quite complicated and no simple solution is allowable for predicting correctly the dynamic behaviour of the rotor, see for example Alessandro et al. [71].

However, every kind of wind rotor despite its type or shape has the peculiarity that at the lower values of TSR, power curves collapse; this means that for studying the start-up dynamics of a wind turbine it is possible to approximate its behaviour in proximity of the rest condition with one curve only, i.e., there is no need to known the complete dependence of C_{PR} from Reynolds number, provided one power curve at a fixed wind speed at least. The advantage of using such an approximation consists in the simplification of the mathematical integration of the second cardinal equation of dynamics, where knowledge of one C_{PR} curve allows to predict the starting capability of the machine correctly. Obviously after the start-up phase such an approach leads to approximated results in studying the overall turbine dynamics, nevertheless it makes possible to discover several characteristic features of the rotor when subjected to a specific wind time-hystory. This is the approach will follow from now on for the case of a Savonius rotor.

Usually, aiming at characterize the start-up capabilities of a wind rotor the no-load condition test is performed and the rotor made free to accelerate when subjected to the considered wind load without connecting the generator, [67] and [28]. For this case, the Newton second law rewrites:

$$I_R \dot{\omega} = M_{mR}(t) - M_{rR}(t) \tag{5.5}$$

where $M_{mR}(t)$ is again the aerodynamic torque generated from the rotor, I its moment of inertia and $M_{rR}(t)$ the resistance opposed to rotation by the bearings or other parasitic effects. This equation holds instant by instant with I determining the dynamic response of the machine to the wind. Assuming to approximate the aerodynamic torque with its averaged values coming from only one known power curve, allows to simplify a lot the problem of Eq. 5.5, provided the turbine moment of inertia and the wind speed time-history; note in fact that all the available turbine characteristics such those in Figs. 5.4, refer always to the averaged values per rotation of the machine at the considered regime.
With these assumptions we can express $M_{mR}(t)$ in Eq. 5.5 as a function of TSR only, and then in terms of ω and V_0 by virtue of Eq. 5.2:

$$M_{mR}(\omega) = \frac{1}{2}\rho V_0^2 A_R R \cdot \frac{C_{PR}(\lambda)}{\lambda} \tag{5.6}$$

$$C_{PR}(\lambda) = a\lambda^3 + b\lambda^2 + c\lambda \tag{5.7}$$

Therefore, interpolating for example C_p with a polynomial expression like that of Eq. 5.7 and solving for the angular velocity, Eq. 5.5 rewrites as follows:

$$\begin{cases} \frac{d\omega}{dt} = \frac{\rho R^2 H_R}{I_R}\left[aR^2\omega(t)^2 + bRV_0(t)\omega(t) + cV_0(t)^2\right] \\ \omega(t_0) = 0 \end{cases} \tag{5.8}$$

Eq. 5.8 is a first order ordinary differential equation in ω with initial condition of rest at time t_0=0 for the known wind speed $V_0(t)$. This is exactly the form that our problem takes within the assumed hypothesis.
With such a mathematical tool at hand we can try to solve numerically for $\omega(t)$ by the position $V_0(t) = v_{eq}(t)$. This problem is solved in $Matlab^{®}$ by use of the *ode*45 solver based on an explicit Runge-Kutta (4,5) formula. It is a one-step solver because in solving for $\omega(t_n)$, it needs only the solution at the preceding time point, $\omega(t_{n-1})$.

5.2.1 Code Validation

We test our simplified approach with reference to the work of I. Ushiyama and Jinkichi [28] who tested different Savonius rotors at constant wind speeds with varying up to 7 design parameters in order to provide the optimum design configuration. In particular we refer to the conventional two-bladed Savonius rotor of aspect ratio 3 whose characteristic curves are depicted here in Figs. 5.5. According to our approach from now on we consider the turbine as characterized only by the 6 m/s power curve.

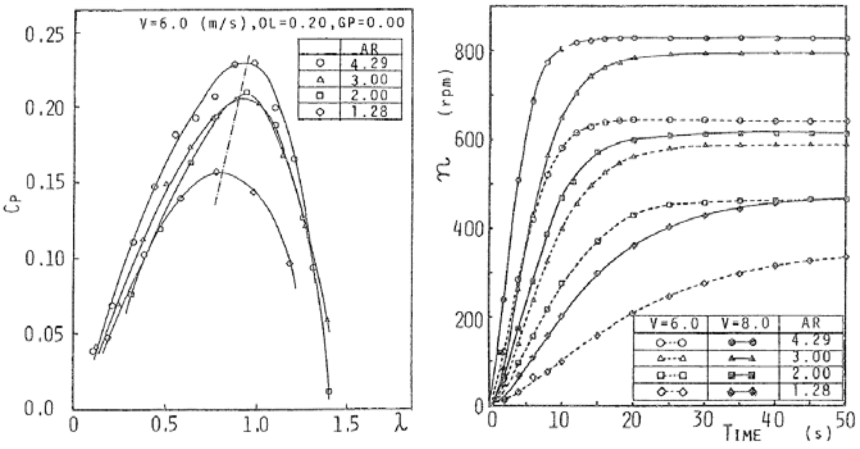

(a) C_p trends

(b) Start-up curves at constant wind speed

Figure 5.5: Curves for the 2-bladed Savonius rotors, from [28]

Testing the start-up behaviour of the turbine with solving the problem in Eq. 5.8 and assuming no parasitic loss for simplicity (i.e. $M_{mR}(t) = 0$) gives the results of Fig. 5.6. Here we can see that accordingly to experimental

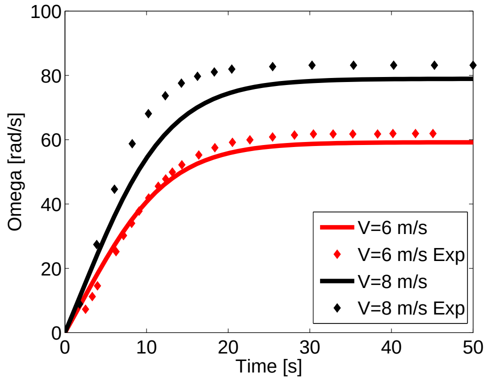

Figure 5.6: Numerical results compared to tests from [28]

results the start-up behaviour of the turbine is well predicted for the case of a constant wind speed of 6 m/s; this is not a surprise because the C_p reference curve is taken exactely for that wind speed. When considering the 8 m/s case, Fig. 5.6 shows some degree of discrepancy between the experimental results and the numerical values, but a reasonable agreement exists, especially at the lower values of angular velocity where our approximation strictly holds. Note also that for both the calculated curves maximum speeds are lower than the experimental ones because no bearing or other parasitic resistances were considered; here the turbine reaches a dynamic equilibrium corresponding to the C_p=0 condition on the right branch of the C_p curve of Fig. 5.5(a).

5.2.2 Turbine Response to the Equivalent Velocity Pulse: 1 Truck Case

Once the code has been tested for the simple case of constant wind speed, we start to solve the dynamic problem of Eq. 5.8 with considering the time varying velocity pulse generated by a moving truck. Before attempting any solution of the rotor dynamics we extend the equivalent velocity pulse of Fig. 4.18 in both the near and far wake regions. According to the experimental results of Baker et al. [17] analyzed in Sec. 2.1.1, we model the near-wake region extending our CFD simulated wake for 10 time units and the far-wake region introducing a decay exponent of -0.6, see Fig. 2.5, considering an overall time interval of about 60 time units. Therefore, making dimensional the equivalent velocity depicted in Fig. 4.18 for the case of a cruising speed of 100 km/h, we make the substitution $V_0(t) = v_{eq}(t)$ in Eq. 5.8 and solve for $\omega(t)$ assuming again $M_{mR}(t)$=0 because of the parasitic little influence, as discussed above. Results from such a calculation are plotted in Figs. 5.7.

Fig. 5.7(a) shows the non-dimensional time history comparison between the velocity signal v_{eq} and the rotor angular velocity (note that the time origin is set when v_{eq} starts to increase); from this figure we can see that the rotor is able to self-start when subjected to the calculated velocity pulse.

As can be seen, the rotor senses velocity peaks as the impulsive acceleration in the turbine angular velocity shows at the very beginning; just before the

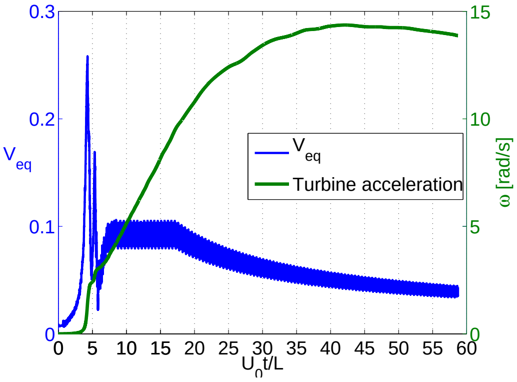

(a) Turbine start-up dynamics

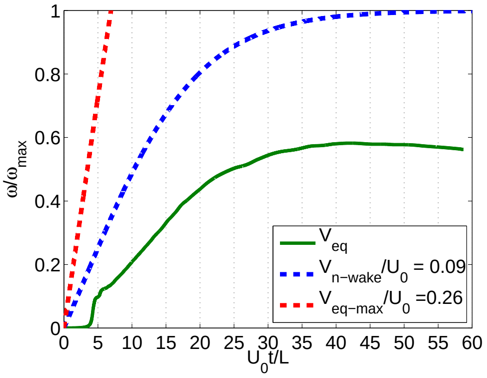

(b) Turbine start-up comparison between variable and constant wind speed

Figure 5.7: The turbine dynamics when subjected to v_{eq}

first peak, i.e. for about U_0t/L <3 the curve is very flat, but when the nose of the truck passes underneath the turbine, i.e. when the first velocity peak appears, the turbine accelerates significantly slowing its rate once the peaks have passed. After that, a constant acceleration rate is visible until about U_0t/L =17 where the wake starts to decay. Then, the rotor reaches a maximum at around U_0t/L =40 and starts to decelerate with a very slow rate. To analyze more such a behaviour look now at Fig. 5.7(b), where we depict the rotor angular velocity along with the analogous constant-wind curves for

a wind speed equal to that of the near-wake region (blue curve) and that of the maximum peak velocity (red curve) respectively. Note that angular velocities are made all non-dimensional based on the maximum regime of the near-wake start-up curve. At the beginning of the time interval analyzed, we notice that effectively the turbine is propelled by the peaks because of the similarity between the turbine angular velocity curve and the constant-wind curve for the maximum peak velocity at about $U_0 t/L$ =4. Furthermore, comparing the rotor curve with the near-wake start-up curve shows that the turbine is unable to reach the maximum allowable regime, or in other words, that the near-wake region is too short for allowing the turbine reaching the maximum allowable rotational speed.
Such a result depends from the inertia of the rotor as we can see from Fig. 5.8, where the effects of changing the moment of inertia of the turbine is depicted for the two cases of increasing and decreasing 0.5 times the reference value I_0 used for the above simulations along with the reference case of Fig. 5.7(a). Results show that increasing the inertia of the turbine is paid with a very little loss in the peaks contributions and an appreciable time delay to reach the final regime. When decreasing of the same quantity the turbine moment of inertia, advantages could be seen for the gain due to the peaks that drives the rotor towards higher rotational velocities with the start-up curve resembling more the corresponding constant-wind curve. At the same time, such a reduction in the rotor inertia makes the turbine more prone to reductions in flow velocity as the strong deceleration at $U_0 t/L$ =25 shows. Anyway, as known, the rotor inertia changes only the time required by the machine to reach the final regime according to the considered wind load.

To see how the peaks in the equivalent velocity affects the turbine start-up behavior look at Figs. 5.9 where the same curves of Figs. 5.7 are depicted for an equivalent velocity curve without peaks.

Note that here values are made non-dimensional basing on the maximum rotor speed reached by the turbine in the case with peaks. For this test, the original velocity pulse is modified replacing the velocity peak region with a smooth curve but retaining the same wake region. As can be seen, the rotor reaches the maximum allowable regime corresponding to the minimum velocity value of the far-wake region, showing that what really makes the tur-

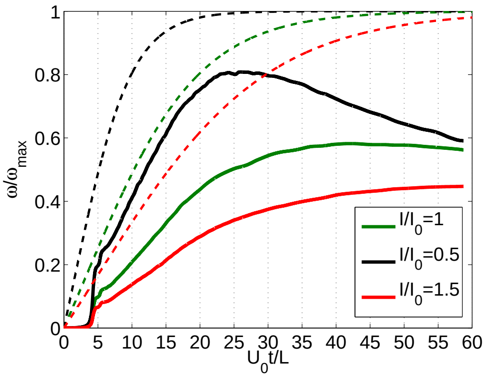

Figure 5.8: Turbine start-up comparisons with varying the moment of inertia

bine rotate is the wake. In fact, comparison between the obtained rotational curves for the two cases depicted in Fig. 5.9(c) shows that peak contribution makes the turbine rotating faster but is the wake that really propels the rotor. This result comes from the fact that the wake trailed region expands behind the truck, as Fig. 4.8(a) shows.

For completeness, Fig. 5.10 shows how the rotor angular velocity measured just after the second induced velocity peak is affected by the changing in the turbine moment of inertia (the angular velocity is made non-dimensional with respect to the maximum regime of the constant wind start-up curve for the near-wake region). As can be seen the rotational velocity follows an hyperbolic-like dependence from I/I_0, with values around the maximum regime of the wake for very low values of I.

In the same figure (green curve) we plot the time delay $\Delta(U_0t/L)$ from the the second peak (i.e. from the truck base region) at which the rotor starts to decelerate, this is the locus of time-points where the maximums of the start-up curves locate (see for example the black curve in Fig. 5.8). As expected, with increasing the rotor inertia the delay (expressed here in time units) increases, the trend being linear. Note that the plateau on the right is due to the imposed limit in the analyzed time interval that forces the maximum rotational speed to be located here starting from about I/I_0 =1.4. On the other side, when considering very low values of inertia we can see that the turbine is so slender that starts to decelerate more and more near the second velocity peak.

If now we assume to define the turbine as started when it has reached the plateau, the delays of Fig. 5.10 represent the time required by the turbine to reach the assumed reference regime as well. Therefore we can see from results such those depicted in Fig. 5.8 that start-up times are not so different from those of the corresponding start-up constant-wind curves.

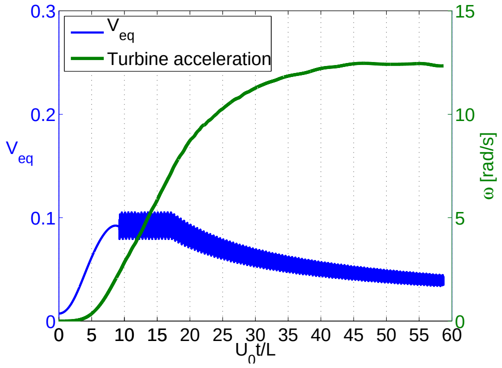

(a) Turbine start-up dynamics

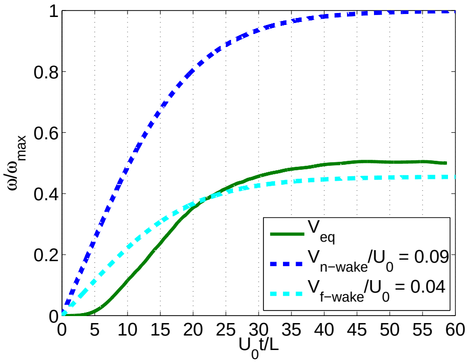

(b) Turbine start-up comparison between variable and constant wind speed

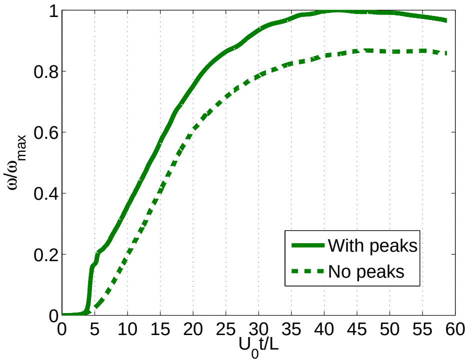

(c) Turbine behaviour for evaluating the peaks effect

Figure 5.9: The turbine dynamics

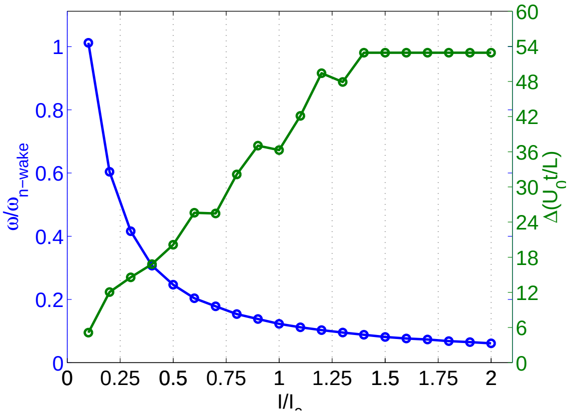

Figure 5.10: Start-up analysis with varying the rotor inertia

5.2.3 Turbine Response to the Equivalent Velocity Pulse: Multi-Truck Case

Characterizing the turbine response in the multiple truck passage case requires knowledge about both the obstacle-truck row interaction and the equivalent velocity pulse as we have done for the single truck case of Sec. 4.2.2.2. A deeper investigation is required to see whether the gain in drag reduction operated by the leading trucks could compensate for the possible drag increase for trailing vehicles caused by the presence of a turbine. Therefore, only for the purpose of testing what would happen in the multiple passage case, we ignore here the interaction problem and consider first the case of three trucks in a row. Therefore, a 3D RANS simulation for three ET vehicles 10 m spaced as studied in Sec. 4.2.2.1 for the 2D case is performed basing exactly on all the assumed conditions and settings of the 3D one truck case of Sec. 4.2.2.2. Results for this special case are used to evaluate the equivalent velocity pulse basing on the virtual loads and the results from Sec. 4.2.2.2 to determine indirectly both real and difference load values, see Figs. 5.11.

As can be seen, our simplified approach is able to catch very well the induced flow as comparison with the equivalent velocity pulse for the single truck case shows in Figs. 5.11(b), proving that effectively loads could be scaled among them as suggested. As expected, the first truck of the row behaves as it was alone, apart for the peak in the base region; in this case the trucks are so close that peaks in the region between them merge and a wider region of higher velocity forms. Note also that Figs. 5.11 show the reduction in magnitudes that loads and then V_{eq} suffer as a consequence of the trailing motion.

According to our method for determining the equivalent velocity signal for the case of 3 ET trucks in a row, no wake is captured forcing us to model such a region artificially by adjoining the wake shape of the 1 truck case model, see Fig. 5.12(a). With the dynamics of the turbine solved, Figs. 5.12 shows that the turbine takes advantage from the peaks generated by the trailing trucks, but Fig. 5.12(b) shows that the start-up performances are still poor as the comparison with the near-wake start-up curve shows. Anyway,

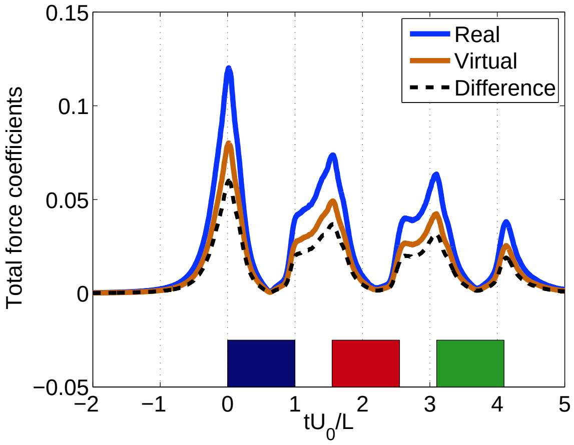

(a) Total force coefficients

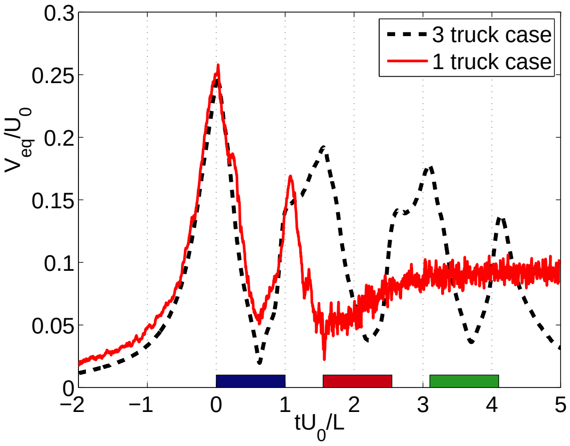

(b) The derived equivalent velocity pulse

Figure 5.11: Loads and equivalent velocity pulse as derived for the 3 truck case study

the rotor is able to reach an higher rotational regime than that obtained in the case of the single truck, see Fig. 5.12(c) where again values are expressed with reference to the maximum value of the 1 truck case curve.

All the results above show that the turbine is able to catch up the energy content of the velocity peaks induced by trailing trucks. Therefore, we explore now the case of an infinite truck row where the equivalent velocity pulse is constructed by the repetition of the third velocity peak of Fig. 5.12(b), or in other words, we make the hypothesis that after the third truck the velocity signal stabilizes and no modifications of the velocity pulse occurs; results for this case are shown in Figs. 5.13.

As can be seen the turbine accelerates reaching a maximum regime at about U_0t/L=60, meaning that the rotor requires about 39 ET trucks 10 m spaced to reach a steady-state regime; such a regime, see Fig. 5.13(b), is that the turbine would reach for the case of a constant wind-speed of about 0.12 times the truck speed, i.e. about 3.3 m/s. For this case the air-flow generated by the trucks is a little stronger than that produced by the single truck motion. Furthermore, we stress again that the turbine maximum regime is unaffected by the rotor moment of inertia, but affects only the time required by the turbine to reach such rotational velocity.

When different values of truck spacing are considered one can expect different rotor responses, and Figs. 5.13 show that even at this low distances the rotor is able to decrease its rotational regime (i.e. it decelerates) just after each single peak suggesting that the more is the distance between trucks the higher would be the turbine start-up time. In other words, with increasing the vehicles spacing the leading and trailing trucks peaks still merge but a wider low velocity region in the middle of the two is expected making the turbine decelerate there. Ideally, the best case scenario would be the case in which peaks between trucks merge making the rising in velocity monotonic until the maximum, our assumption of 10 m distance being not so far from that, see for example Fig. 5.11(b).

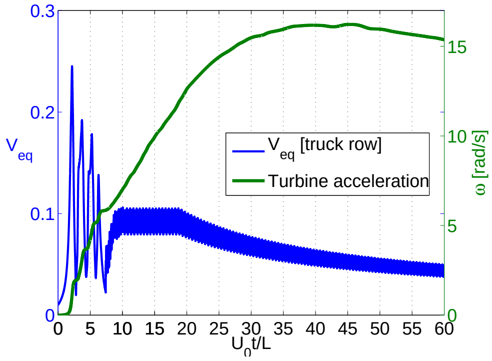

(a) Turbine start-up dynamics for the truck row

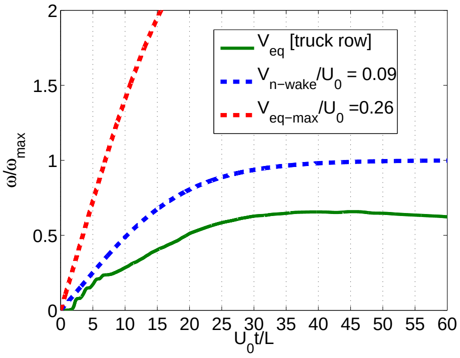

(b) Turbine start-up comparison between variable and constant wind speed

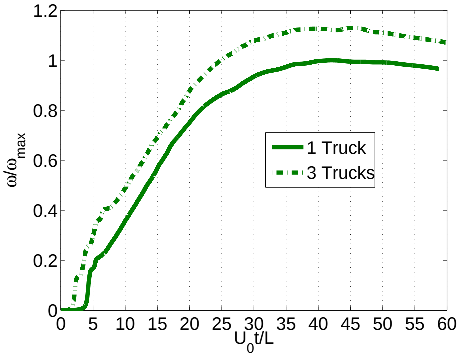

(c) Turbine start-up comparison between 1 and 3 ET trucks in a row

Figure 5.12: The turbine dynamics for the case of a truck row with vehicles spaced 10 m apart

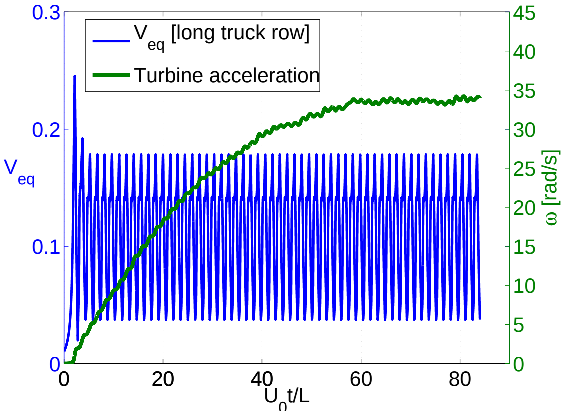

(a) Turbine start-up response for the long truck row

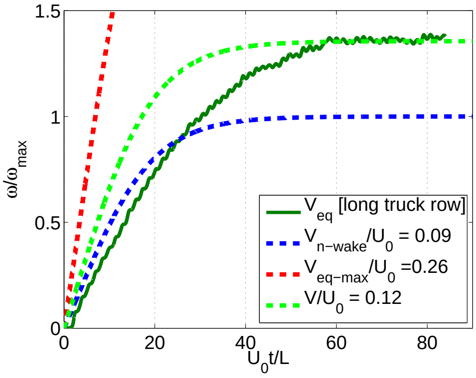

(b) Turbine start-up comparison between variable and constant wind speed

Figure 5.13: Turbine start-up behaviour when subjected to a long truck row

5.2.4 Estimating the Energy Output

All results analyzed in the previous section relating the turbine start-up behaviour when subjected to truck rows are derived neglecting completely the problem of the turbine-trucks interaction. Still basing on such an hypothesis we make now a rough energy balance to evaluate the energy potential that the assumed technology would be able to harvest according to obtained outcomes.

First of all we remember that for the infinite truck row case of Sec. 5.2.3 the turbine behaves as it was propelled by a constant wind velocity of about 3.3 m/s that consists in a very poor energy content flow for a turbine despite the assumed high traffic conditions; Savonius rotors often have their cut-in speed at 3 m/s and rated speed higher than this. Anyway, aiming at evaluating the available energy content we model the turbine dynamics applying the electric load at the shaft and hypothesizing that the turbine could operate at its maximum efficiency for the assumed wind speed. With this purpose in mind we define the characteristic curve for the generator as a parabola passing for the maximum of the assumed C_p rotor curve with the following:

$$C_{Pgen} = \frac{C_{PR\max}}{(\lambda_{\max})^2}\lambda^2 \tag{5.9}$$

where C_{PRmax} and λ_{max} are the maximum power coefficient and tip speed ratio of the power curve in Fig. 5.5(a) for the 6 m wind case. With this model, the generator entries Eq. 5.8 contributing to the b coefficient with $-C_{PRmax}/\lambda_{max}$. Solving this problem with our code give the results shown in Figs.5.14. With the assumed wind velocity we found that the turbine attains the regime corresponding to a TSR value of about 0.9 that matches the experimental one from Fig. 5.5(a), as expected. In this conditions the turbine reaches the steady regime in about 25 time units exploiting 20% of the incoming wind energy power (i.e. C_p=0.2). According to the frontal area of the rotor considered (A_R =0.128 m^2) and by use of Eq. 5.1 we obtain that the rotor generates power for about 0.56 W or 0.56 Wh of energy. Hypothesizing a constant traffic flow rate all year long at the end we find about 4.9 kWh that is about 0.18 % of the yearly energy consumption of the Italian

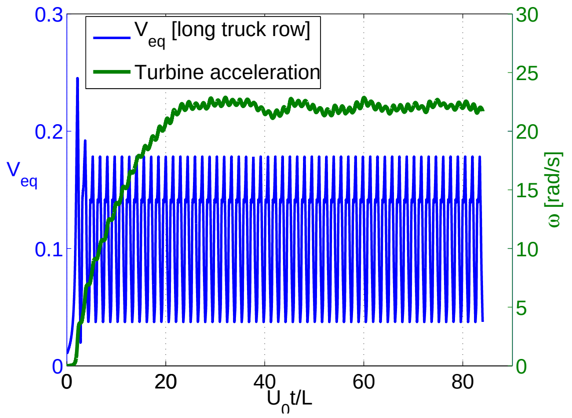

(a) Turbine start-up response for the long truck row

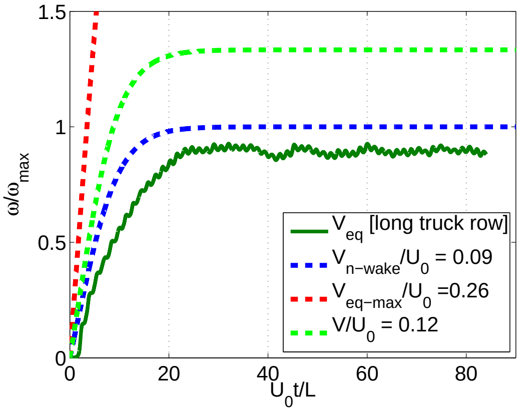

(b) Turbine start-up comparison between variable and constant wind speed

Figure 5.14: Turbine start-up behaviour when subjected to a long truck row

middle-class family (2700 kWh). Note also that this traffic corresponds to the passage of one vehicle roughly each second corresponding to about 86400 VMGT that is about 3.9 times the traffic of heavy vehicles for the Italian A1 highway in the section connecting Brescia with Padova (as cited in the introductory section of the present work).

Hence, results for the high traffic condition above show that the available energy content is huge but the efficiency at which such an energy could be eventually harvested with the studied technology is really poor.

Chapter 6

Conclusions and Perspectives

The increasing energy demand together with the problem of pollutant emissions due to fossil based combustion processes calls for new energy scenarios where alternative and renewable energy sources will have to contribute increasingly. Along with such technologies that operate at a macro-scale level, new efforts are spent in the direction of micro-scale harvesting technologies as well, especially for powering electronic portable and auxiliary devices. Generally, an energy harvesting process aims at scavenging secondary energy flows, generated by standard industrial and/or every-day life primary processes, that otherwise would be lost. Among all, that of harvesting energy from the air-flows induced by the road traffic has grown in interest particularly in the last 3-4 years. Actually, at the huge increase in the number of circulating road vehicles corresponds the enormous energy waste due to the aerodynamic loss that vehicles have to overcome for moving. Therefore, a question arises wether such an energy content could be really harvested, or in other words, if such induced air-flows could be considered a feasible alternative energy source. This issue is the one we aimed to explore in the present work, with special emphasis put into truckage and the possibility of exploiting such air-flows using VAWT generators.

At the very beginning, by means of a brief historical analysis we have showed that starting from about 1993 till today, several authors had registered patents on the subject with special attention devoted to the use of verti-

cal axis wind turbines for harvesting road vehicles induced flows, Sec. 1. Because of the lack in technical literature about such a problem, the study focused first in a general understanding of the phenomena involved basing on cross-related studies and researches, Sec. 2. In doing so we had gain insights into the mechanisms on how a truck interacts with its surroundings and a more accurate numerical campaign of increasing complexity has been planned for studying the involved phenomena, Sec. 3.
Activities were performed approaching the problem with 1D, 2D and 3D modeling methods based on the flat-plate approach and CFD numerical simulations using the ANSYS *Fluent*® commercial code. CFD simulations were planned for evaluating both the general flow features around the moving vehicle but also its interactions with an external object placed nearby by use of steady and unsteady RANS approaches respectively. In all these simulations attention was paid on the absolute flow rather than on the relative flow, the latter being of interest in the field of standard aerodynamics. The time-dependent simulations where mandatory for evaluating the interaction between the moving truck and an external object mimicking the wind generator that here was not simulated. Such an issue was of extremely importance because of the need for the harvesting process to work only with the wasted aerodynamic energy content, i.e. without affecting more the moving vehicles and in turn increasing their fuel consumption.

In particular, to detect both the available energy contents and the structure of the assumed resource, a flat plate approach based on the available experimental results was articulated and the limited contribution to drag coming from the frictional effects evidenced as a consequence of the bluff-body behaviour of a truck, Sec. 4.2.1.

CFD simulations were performed exploring the induced flow field generated by a truck moving at high speed along a level and windless highway. The special purpose of the numerical campaign was to put light on the flow features upon the trailer roof and with this purposes in mind, a specific new truck shape was designed to represent the typical European truck and used for both 2D and 3D modeling approaches, Sec. 3.2.2.
According to the preliminary bibliographic survey and starting from the general study of the induced velocity and pressure profiles, 2D steady RANS

simulations were performed. In doing so, results for the flow fields were analyzed and compared for one, two and three trucks in a row considering vehicles with and without wheels with varying trucks speed. For all cases, a neat region was identified upon the trucks where trailed flows were confined, but upon them a non-realistic reversed flow as a consequence of the 2D modeling appeared as well. Despite the very low blockage value induced by the truck shape, air flowing with relatively high speed in the opposite direction of the vehicles come from the impossibility for the air to flow sideways of the vehicles. Anyway, the main result was there that trailed flows generated by shear stresses on the roof reach about 1.3 times the truck height thickness for the three trucks case study, showing an unrealistic height decay trend just behind the last truck of the row. Results for pressure fields and velocity profiles were found to be in good agreement with those found in literature, especially in terms of general trends, Sec. 4.2.2.1;

3D steady RANS simulations confirmed that 2D approaches were able to catch some general trend, even if magnitudes for both velocity and pressure fields were deeply overestimated. Modeling of the full domain relieved 2D non-physical effects and a little reversed flow still appeared as a consequence of the blockage induced by the truck; pressure trends for the 3D case showed values up to 70%-less the correspondent 2D values at the reference distance of 1 m above the truck. Furthermore, a realistic wake behaviour was obtained showing that the increase in height of the trailed region there was due mainly by the counter-rotating vortices that force the trailed region to grow when moving downwards from the trailer base. Such a result gave the explanation for the unrealistic height lowering of the trailed region obtained with the 2D approach, evidencing that vehicles induced flows are dominated by strong three-dimensional effects, Sec. 4.2.2.1.

URANS simulations were made to analyze dynamic interactions of the truck with an obstacle with its lower edge placed 1 m height upon the roof. In doing so, no energy absorption was modeled and no turbine rotor was designed but the obstacle used as a probe to explore the flow field upon the truck. Simulations were performed by use of the remeshing technique available in the ANSYS *Fluent*® environment and the method was first validated using results coming from the analyzed literature, results showing a good agreement, Sec. 3.2.2.2. In the 2D modeling approach, both rectangular and circular panels were tested, showing that the presence of the panel increase the truck energy consumption in order to take the speed constant. Aerodynamic performances of the panels with varying dimensions proved that the circular shape affects the drag of the truck to a lesser extent, comparisons made in terms of increments in energy consumption of the truck, Sec. 4.2.2.2.

Simulation of the truck-panel interaction for the 3D case was restricted to the circular cylinder shape, with the truck drag coefficient resulting unaffected by the passage of the obstacle upon the roof, giving some chances for the application of some energy device near the vehicle. In the limits of the modeling approach, 3D URANS simulations showed that drag variations are of the same order of magnitude of the detected time-varying oscillations at least. Forces acting on the cylinder were analyzed and both vertical and horizontal non-dimensional coefficients compared with varying time, revealing that the strongest interaction happens when the truck nose pass underneath the cylinder. Composition of force contributes allowed to study total forces and directions at any given time.

Force coefficients were compared with those coming from the RANS simulation where a fictitious cylinder was moved and loaded only by the pressure field generated by the truck. Hence, the real flow was approximately considered as inviscid, and the loads due to the flow generated by the presence of the cylinder evaluated by mathematical subtraction of the virtual values from those coming from the 3D unsteady results. In doing so, total loads were found to be 1.5 and 2 times higher than virtual and derived values respectively.

With the assumption above, the load coming from the flow induced by the presence of the cylinder was used to evaluate the equivalent flow velocity, a function representing the velocity value that a uniform flow requires to generate on the cylinder the same load. Values of about 0.25 time the truck speed where calculated for the nose region, where according to force trends the strongest interaction with the cylinder occurred. Therefore both flow velocity and pressure pulses were characterized using the 3D obstacle as a probe, and load mechanisms explained, Sec. 4.2.2.2.

Finally a simplified approach was used to study the start-up behaviour of a VAWT rotor when subjected to the calculated induced-wind. Drag-driven rotors were demonstrated to be superior than lift-type rotors for this application and our attention was put only on the Savonius turbine. Numerical integration of the Newton second Law for rotation was performed with the approximation of considering a real Savonius rotor as characterized by only one of its power curves. According to such a simplification, the calculation for evaluating the rotor angular velocity with varying time was performed for a moving truck using the equivalent velocity signal, Sec. 5.
Results proved that the rotor was able to start-up, the speed reached in the no-load condition at regime being compatible with experimental values. The main outcome was there that the turbine worked as it was propelled mainly from the wake, the velocity peaks contributing mainly in allowing the turbine to reach about 10% higher rotational speed than that obtained in the case of no peaks present. Note here that such a result comes from the growth in height of the trailed flow in the wake region, that we remaind the 2D approach was unable to catch.
Therefore the wind rotor behaved as it was propelled by a constant wind velocity equal to that of the wake generated by the truck, that is lower than the cut-in wind-speed typical for this type of rotors.

Results for the obstacle-vehicle interaction in the case of a truck row was not planned in the present work, and evaluation of the turbine start-up behaviour made only with the purpose of estimating the available energy content. With this aim a final 3D RANS simulation was performed for a row of 3 trucks 10 m spaced aiming at calculating virtual values for the load acting again on the fictitious cylinder as before. Therefore, according to results coming from the single truck case, the flow impinging on the cylinder was calculated and the equivalent flow velocity pulse derived such that a very good agreement with the results for the one truck case was observed for the leading truck.
Solving the turbine dynamics with such a pulse showed that the turbine improved its performances which means that trailing trucks contribute with their velocity peaks to the acceleration of the rotor.
After that, a row of infinite trucks 10 m spaced was generated and the turbine

dynamics solved again for this velocity signal. Results for this case have shown that the rotor was able to reach the steady-state regime equivalent to that of a constant wind speed higher than that of the wake but a little more. i.e. about 0.12 times the truck speed.
Starting from this result the turbine dynamics was analyzed modeling the electric generator such that at the calculated wind velocity the turbine got the maximum efficiency. As expected the turbine reached the steady state regime at equilibrium in a little time (about 20 time units, i.e. about 13 truck 10 m spaced against the 60 time units of the no-load case) but with a delivered power of just 0.56 W corresponding to an yearly energy delivery of about 4.9 kWh.

All the obtained results indicate that in the scenario considered here, i.e. that of a truck moving in a level and straight road, harvesting energy by means of a wind turbine placed upon the vehicles is not a feasible process. Flows are very slow and the idea of gaining energy from the velocity peaks induced by trailing trucks give a little help, especially when this case is compared to that of placing the turbine exposed to the atmospheric wind, where it could be that the harvested energy is higher depending on the site. Note also that the calculated power requires a very intense traffic flow for the turbine to deliver such an energy content, even if the very limiting distance of 1 m above the truck was considered.
Nevertheless, in the author opinion is that such a limit relays mainly in the source rather in the technology, meaning that other cases of moving vehicles could be of interest for this application. The road traffic could be of interest when air-flows are channeled into a tunnel, or the case of high speed trains, especially because they are inherently long and could operate at very higher velocities than those typical for a truck. For high speed trains, very high values of velocity for the wake are known to be generated meaning that consideration of such vehicles could really make the investigated technology feasible; anyway, the study of the interaction between the energy device and the moving vehicle need to be performed first. Note again that in the present work the truck-turbine interaction was not simulated directly and data about such a problem is still required, hence CFD analysis and/or in-field tests for the different cases and configurations would be helpful for the purpose.

Bibliography

[1] T.A. Wither. Apparatus for generating power, December 21 1993. URL `http://www.google.com/patents/US5272378`. US Patent 5,272,378.

[2] H. Gutterman. Wind-generated power system, June 25 2002. URL `http://www.google.com/patents/US6409467`. US Patent 6,409,467.

[3] A.W. Bilgen. Wind power generating system, October 26 2004. URL `http://www.google.com/patents/US6809432`. US Patent 6,809,432.

[4] N.R. Di. Electric power generator driven by the draft of passing vehicles, March 30 2005. URL `http://www.google.com/patents/EP1519011A1?cl=it`. EP Patent App. EP20,030,021,606.

[5] T.F. Wiegel and K.C. Stevens. Traffic-driven wind generator, August 29 2006. URL `http://www.google.com/patents/US7098553`. US Patent 7,098,553.

[6] A.A. Van Meveren and G.D. Van Meveren. System for generating electrical energy from vehicle movement on a road, March 8 2011. URL `http://www.google.com/patents/US7902690`. US Patent 7,902,690.

[7] G. Mauro and U. Alkaragholy. Road with inlayed wind harnessing technology, December 11 2012. URL `http://www.google.com/patents/US8328499`. US Patent 8,328,499.

[8] A. Ignatiev and Y. Song. Dual-mode roadway turbines for energy generation from artificial pulsed vehicle wind and continuous ambient wind, April 23 2013. URL `http://www.google.com/patents/US8427000`. US Patent 8,427,000.

[9] Archinect-Blogs, 2007. URL `http://archinect.com/blog/article/21451130/here-goes-please-comment`. (Accessed 19 Dic 2013).

[10] 2007. URL `http://www.ecogeek.org/wind-power/524`. (Accessed 19 Dic 2013).

[11] A. Schwartz, 2010. URL `http://inhabitat.com/turbine-light-powers-highway-lights-with-wind/`. (Accessed 19 Dic 2013).

[12] 2011. URL `http://www.energyharvestingjournal.com/articles/harnessing-wind-energy-from-traffic-00003093.asp?sessionid=1`. (Accessed 19 Dic 2013).

[13] Arianna Callegari. The green tunnel, 2011. URL `http://betterymagazine.com/ideas/natural-wind`. (Accessed 19 Dic 2013).

[14] G. Sanna. URL `http://www.designbuzz.com/city-speed-turbine-harnesses-wind-power-produced-by-the-speed-of-vehicles`. (Accessed 19 Dic 2013).

[15] Pino Bruno, 2010. URL `http://www.pinobruno.it/2010/08/eolico-in-francia-energia-prodotta-dal-passaggio-dei-camion-sulláutostrada/`. (Accessed 19 Dic 2013).

[16] URL `http://lab.enel.com/it/finalist/atea`. (Accessed 19 Dic 2013).

[17] C. J. Baker, S. Dalley, T. Johnson, M. A. Brown, A. P. Gaylard, A. Quinn, and N. Wright. Measurements of the Slipstream and Wake of a Model Lorry. In *3rd MIRA International Conference on Vehicle Aerodynamics*, October 2000. ISBN 095 24156 2 3.

[18] P.M. Cali and E.E. Covert. Experimental measurements of the loads induced on an overhead highway sign structure by vehicle-induced gusts. *Journal of Wind Engineering and Industrial Aerodynamics*, 84:87–100, April 2000.

[19] A.D. Quinn, C.J. Backer, and N.G. Wright. Wind and vehicle induced forces on flat plates-part 2: vehicle induced forceexperimental measurements of the loads induced on an overhead highway sign structure by vehicle-induced gusts. *Journal of Wind Engineering and Industrial Aerodynamics*, 89:831–847, April 2001.

[20] S.P. Veluri, C.J. Roy, A. Ahmed, R. Rifki, J.C. Worley, and B. Recktenwald. Joint computational/experimental aerodynamic study of a simplified tractor/trailer geometry. August 2009.

[21] C.J. Roy, J. Payne, and M. McWherter-Payne. Rans simulations of a simplified tractor/trailer geometry. September 2006.

[22] B.L. Storms, J.C. Ross, J.T. Heineck, S.M. Walker, D. M. Driver, and G.G. Zilliac. An experimental study of the ground transportation system (gts) model in the nasa ames 7- by 10-ft wind tunnel. 2001.

[23] S. Krajnović and L. Davidson. Large-eddy simulation of the flow around a ground vehicle body. 2001.

[24] J. Östh. A les study of a simplified tractor-trailer model. Master's thesis, Chalmers University Of Technology, 2010.

[25] F.M. White. *Fluid Mechanics.* Fourth edition. ISBN 978-0-07-128645-9.

[26] M Ougburn, L. Ramroth, and A.B. lovins. Transformational trucks: determining the energy efficiency limits of a class-8 tractor-trailer. July 2008.

[27] E. Hau. *Wind Turbines: Fundamentals, Technologies, Application, Economics.* Springer, 2006. ISBN 9783540242406. URL `http://books.google.it/books?id=Z4bh0bd65IAC`.

[28] H. Nagai I. Ushiyama and S. Jinkichi. Experimentally determining the optimum design configuration for savonius rotors. *Bulletin of JSME*, 29 (258):4130–4138, 1986.

[29] S. Maddox, K.D. Squires, K.E. Wurtzler, and J.R. Forsythe. Detached-eddy simulation of the ground transportation system. Article in "The

Aerodynamics of Heavy Vehicles: Trucks, Buses, and Trains." Lecture Notes in Applied and Computational Mechanics Vol. 19. Editors: McCallen, Rose, Browand, Fred, Ross, James. Page 11, 2004.

[30] AISCAT. gennaio-marzo e aprile-giugno 2013. Technical Report 1-2, Associazione Italiana Società Concessionarie Autostrade e Trafori, 2013. notiziario trimestrale.

[31] G.T. Bellarmine and J. Urquhart. Wind energy for the 1990s and beyond. *da mettere*, 1996.

[32] L.R. Wilson. Windturbine driven by trafic, May 3 2001. URL `http://www.google.com/patents/WO2001031196A1?cl=en`. WO Patent App. PCT/GB2000/004,118.

[33] T. Spinelli. Methods and apparatus for generating power from vehicles, April 27 2006. URL `http://www.google.com/patents/US20060087201`. US Patent App. 10/972,547.

[34] H.E. Dempster. Barrier-mounted wind-power generation system, November 15 2007. URL `http://www.google.com/patents/US20070264116`. US Patent App. 11/746,625.

[35] R. Schmidler. Verfahren und einrichtung zum nutzbarmachen regenerativer energie, September 11 2008. URL `http://www.google.com/patents/DE102007011582A1?cl=de`. DE Patent App. DE200,710,011,582.

[36] V. Gushakowski. Device for producing a current comprises a roller with blades rotating about a shaft which is fixed to a floor or ceiling, January 4 2007. URL `http://www.google.com/patents/DE102005029922A1?cl=en`. DE Patent App. DE200,510,029,922.

[37] T. King and D.W. Ratcliffe. Improvements in or relating to energy generation, February 5 2009. URL `http://www.google.com/patents/WO2009015907A2?cl=en`. WO Patent App. PCT/EP2008/006,408.

[38] L. Chen, F.L. Ponta, and L.I. Lago. Perspectives on innovative concepts in wind-power generation. *Energy for Sustainable Development*, 2011.

[39] URL `http://www.designrepublic.it/viewdoc.asp?co_id=2133`. (Accessed 19 Dic 2013).

[40] Khalid M. Saqr and Md. Nor Musa. A perspective of the malaysian highway energy consumption and future power supply. *Energy Policy*, 39 (6):3873 – 3877, 2011. ISSN 0301-4215. doi: http://dx.doi.org/10.1016/j.enpol.2011.03.034. URL `http://www.sciencedirect.com/science/article/pii/S030142151100214X`.

[41] CITA PRODUCTION, . URL `http://www.cita-production.com/`. (Accessed 19 Dic 2013).

[42] CITA PRODUCTION, . URL `http://www.evi-production.fr/eol.php`. (Accessed 19 Dic 2013).

[43] Fey Systems. URL `http://www.feisystemsitaly.it/gallery_it.html`. (Accessed 19 Dic 2013).

[44] Riccardo Luna. Autostrade come centrali: l'energia dal vento sollevato dai camion. URL `http://www.repubblica.it/ambiente/2013/05/13/news/autostrade_come_centrali_l_energia_dal_vento_sollevato_dai_camion-58671674/?ref=HRERO-1`. (Accessed 19 Dic 2013).

[45] B.M. Creamer, K.H. Frank, and R.E. Kligner. Fatigue loading of cantilever sign structures from truck wind gusts. *Journal of Wind Engineering and Industrial Aerodynamics*, 1979.

[46] M.N. Albert, L. Manuel, K.H. Frank, and S.L. Wood. Field testing of cantilevered traffic signal structures under truck-induced gust loads. March 2007.

[47] A. Sanz-Andrès, J. Santiago-Prowald, C. Baker, and A. Quinn. Vehicle-induced loads on traffic sign panels. March 2003.

[48] A. Sanz-Andrès, C. Gragera, J. Meseguer, and F. Zayas. Experimental investigation on the force induced by a high speed vehicle passing by a traffic sign. July 2009.

[49] R.H. Croll, W.T. Gutierrez, B. Hassan, J.E. Suazo, and A.J. Riggins. Experimental investigation of the ground transportation systems (gts) project for heavy vehicle drag reduction. *SAE Paper No. 960907,SP 1145*, 1996.

[50] B.L. Storms, D.R. Satran, J.T. Heineck, and S.M. Walker. A summary of the experimental results for a generic tractor-trailer in the ames research center 7- by 10-foot and 12- foot wind tunnels. 2006.

[51] K. Salari, J.M. Ortega, and P.J. Castellucci. Computational prediction of aerodynamic forces for a simplified integrated tractor-trailer geometry. June 2004.

[52] K. Salari R.C. McCallen, J. Ortega, L. DeChant, B. Hassan, C. Roy, W.D. Pointer, F. Browand, M. Hammache, T.Y. Hsu, A. Leonard, M. Rubel, P. Chatalain, R. Englar, J. Ross, D. Satran, J.T. Heineck, S. Walker, D. Yaste, and B. Storms. Doe's effort to reduce truck aerodynamic drag-joint experiments and computations lead to smart design. June 2004.

[53] M. Hammache and F. Browand. On the aerodynamics of tractor-trailers. Article in "The Aerodynamics of Heavy Vehicles: Trucks, Buses, and Trains." Lecture Notes in Applied and Computational Mechanics Vol. 19. Editors: McCallen, Rose, Browand, Fred, Ross, James. Page 11, 2004.

[54] W.D. Pointer. Commercial cfd code validation for external aerodynamics simulations of realistic heavy-vehicle configurations. Article in "DOE Project on Heavy Vehicle Aerodynamic drag FY 2005 Annual Report" Editors: R.C. McCallen, K. Salari and J. Ortega and P. Castellucci and C. Eastwood and and J. Paschkewitz and L. DeChant and B. Hassan and F. Browand and C. Radovich and T. Merzel and D. Plocher and J. Ross and B. Storms and J.T. Heineck and S. Walker and C. Roy, 2005.

[55] D.G. Hyams, K. Sreenivas, R. Pankajakshan, D.S. Nichols, W.R. Briley, and D.L. Whitfield. Computational simulation of model and full scale class 8 trucks with drag reduction devices. September 2010.

[56] K. Salari, R. McCallen, J. Ortega, C. Eastwood, J. Paschkewitz, and P. Castellucci. Commercial cfd code validation for external aerodynamics simulations of realistic heavy-vehicle configurations. Article in "DOE Project on Heavy Vehicle Aerodynamic drag FY 2005 Annual Report" Editors: R.C. McCallen, K. Salari and J. Ortega and P. Castellucci and C. Eastwood and and J. Paschkewitz and L. DeChant and B. Hassan and F. Browand and C. Radovich and T. Merzel and D. Plocher and J. Ross and B. Storms and J.T. Heineck and S. Walker and C. Roy, 2005.

[57] S. Krajnović and L. Davidson. A test case for large-eddy simulation in vehicle aerodynamics. 2002.

[58] S. Krajnović and L. Davidson. Exploring the flow around a simplified bus with large eddy simulation and topological tools. 2002.

[59] S. Krajnović and L. Davidson. Development of large-eddy simulation for vehicle aerodynamics. 2002.

[60] K.R. Cooper. Commercial vehicle aerodynamic drag reduction: Historical perspective as a guide. Article in "The Aerodynamics of Heavy Vehicles: Trucks, Buses, and Trains." Lecture Notes in Applied and Computational Mechanics Vol. 19. Editors: McCallen, Rose, Browand, Fred, Ross, James. Page 11, 2004.

[61] J.C. Hilliard and G.S. Springer. *Fuel economy in road vehicles powered by spark ignition engines.* May 1984. ISBN 0306414384.

[62] Fluent Inc. *Fluent 14.0 User guide.*, 2011.

[63] R.M. Wood and S.X.S. Bauer. Simple and low-cost aerodynamic drag reduction devices for tractor-trailer trucks. 2003.

[64] C. Diebler and M. Smith. Simple and low-cost aerodynamic drag reduction devices for tractor-trailer trucks. 2002.

[65] C. J. Baker, S. J. Dalley, T Johnson, A Quinn, and N. G. Wright. The slipstream and wake of a high-speed train. *Proceedings of the Institution of Mechanical Engineers, Part F: Journal of Rail and Rapid Transit*, 215 (2):83–99, 2001. doi: 10.1243/0954409011531422.

[66] H. Shlichting. *Boundary-Layer Theory.* Seventh edition, 1979. ISBN 0-07-055334-3.

[67] A. Bianchini, L.Ferrari, and S.Magnani. Start-up behavior of a three-bladed h-darrieus vawt: experimental and numerical analysis. June 6-10 2011. paper No GT2011-45882.

[68] A. Bickerdyke R. Dominy, P. Lunt and J. Dominy. Self-starting capability of a darrieus turbine. *Proceedings of the I MECH E part A : journal of power and energy., 221 (1).*, pages pp. 111–120., 2007.

[69] Y. HARA T. HAYASHI, Y. LI and K. SUZUKI. Wind tunnel tests on a three-stage out-phase savonius rotor. *JSME International Journal*, 2005.

[70] H. Yutaka, H. Koichi, and H. Hayashi. Moment of inertia dependence of vertical axiswind turbines in pulsating winds. *International Journal of Rotating Machinery*, 2012. Volume 2012, Article ID 910940, 12 pages,Hindawi Publishing Corporation.

[71] V. D Alessandro, S. Montelpare, R. Ricci, and A. Secchiaroli. Unsteady aerodynamics of a savonius wind rotor: a new computational approach for the simulation of energy performance. *Energy*, 35(8):3349 – 3363, 2010. ISSN 0360-5442.